行政院原子能委員會

委託研究計畫研究報告

環境氣氛對 SOFC 接合件高溫耐久機械性質之影響

Environmental Effect on High-Temperature Mechanical Durability of SOFC Joints

計畫編號：**1042001INER018**

受委託機關（構）：國立中央大學

計畫主持人：林志光 教授

聯絡電話：**03-4267340**

E-mail address：t330014@cc.ncu.edu.tw

核研所聯絡人員：吳思翰、劉建國

報告日期：**104** 年 **12** 月

目錄

頁碼

中文摘要

本研究目的在探討還原環境對於玻璃陶瓷接合劑和金屬連接板接合件的潛變性質與破壞模式之影響，所使用的玻璃陶瓷為核能研究所開發一款代號為 GC-9 的材質，金屬連接板則是使用代號為 Crofer 22 H 的商用肥粒鐵系不銹鋼。在 800 ℃ 的 H_2-7 vol% H_2O 還原環境下，對於接合件施予剪力及張力固定負載來進行潛變實驗，同時評估還原環境時效處理對接合件潛變性質的影響，並比較在還原環境與氧化環境下潛變性質的差異。

結果顯示，接合件試片於 800 ℃ H_2-7 vol% H_2O 氣氛下的剪力與張力潛變壽命會隨著負載減少而增加。剪力試片具 1000 小時壽命的潛變強度約為剪力接合件強度的 18%，而張力試片具 1000 小時壽命的潛變強度則約為張力接合件強度的 0.67%。兩個可能影響接合件抗潛變性質的原因為：(1) 潛變實驗過程中的即時熱處理，增加 GC-9 玻璃陶瓷基材中的結晶量，並提升接合件的抗潛變能力；(2) 隨著潛變時間增加，還原環境中的水會降低 GC-9 玻璃陶瓷基材中非結晶相的黏滯性，軟化接合件的結構。因此剪力與張力接合件試片的破裂位置，隨著潛變時間的增加，由破裂於 GC-9 玻璃陶瓷基材中，轉變為 GC-9 與氧化鉻(Cr_2O_3)的介面，最後變回破裂於 GC-9 中。

經 1000 小時還原環境時效處理後，剪力試片具 1000 小時壽命的潛變強度約為未經時效處理剪力接合件強度的 32%，而張力試片具 1000 小時壽命的潛變強度則約為未經時效處理張力接合件強度的 38%。經時效處理後，接合件的抗潛變能力降低的主要原因為，在 GC-9 玻璃陶瓷基材中的玻璃相與結晶相之間形成微孔洞所導致。對於未時效處理之剪力與張力試片，在還原環境下接合件的抗潛變能力，明顯低於氧化環境下接合件的抗潛變能力，主要原因為還原環境中的水氣降低接合件的結構強度所致。

Abstract

The objective of this study is to investigate the effect of reducing environment on the creep properties of a joint between a glass-ceramic sealant and an interconnect steel with no and 1000-h thermal aging in a reducing environment (H_2-7 vol% H_2O). The joint between glass-ceramic and metallic interconnect is subjected to an applied tensile or shear constant load in reducing environment at 800 ℃ during the creep test. The materials used are a GC-9 glass-ceramic sealant developed at the Institute of Nuclear Energy Research (INER) and a commercial Crofer 22 H ferritic stainless steel. Comparison of the creep properties in oxidizing and reducing environments is also made for the non-aged joint.

The creep rupture time of Crofer 22 H/GC-9/Crofer 22 H joint is increased with a decrease in the applied constant shear and tensile loading at 800 ℃ regardless of thermal aging condition. The shear and tensile creep strength of non-aged joint at 1000 h in the given reducing atmosphere is about 18% and 0.67% of the average shear and tensile joint strength, respectively. For both non-aged tensile and shear specimens with a short creep rupture time less than 10 h, fracture mainly occurs within the GC-9 glass-ceramic. For a creep rupture time of 10-100 h, fracture site changes to the interface between the Cr_2O_3 layer and the GC-9 glass-ceramic. For a creep rupture time over 100 h, the GC-9 glass-ceramic layer is the major fracture site, again.

After 1000-h thermal aging in the given reducing environment, the shear and tensile creep strength at 1000 h in H_2-7 vol% H_2O of the aged joint is about 32% and 38%, respectively, of that without a thermal aging. Degradation of creep strength in the joint after a thermal aging is probably

due to formation of micro-voids between crystalline and glassy phases during the cooling process. The creep resistance of the non-aged joint is significantly degraded when the testing environment is changed from oxidizing environment to reducing environment. As water in the given humidified hydrogen might relax joint structure, the creep resistance of joint in reducing environment becomes weaker than that in air regardless of loading mode.

1. INTRODUCTION

1.1 Solid Oxide Fuel Cell

Solid oxide fuel cell (SOFC) is the most efficient device for electric power generation, compared with other fuel cells. It converts chemical energy directly into electricity without an intermediate step of conversion to heat such that the efficiency is higher than that of conventional power generation systems. Compared with other fuel cells, the most important features of SOFC include (1) that components are made of solids, (2) that the utilization of solid oxides as the electrolyte which can prevent leakage or evaporation, and (3) that electrochemical reactions occur without noble catalysts and solid oxides possess highly ionic conductivity at a high operation temperature of 600 ℃-1000 ℃. Typical configuration designs for SOFCs developed are tubular and planar cells. Planar SOFC attracts more attention because of its lower fabricating cost, lower operating temperature, and higher current density [1-3].

Schematic of the operating principle in an SOFC using hydrogen as fuel is shown in Fig. 1 [4]. Fuel and oxidant flow though the anode and cathode, respectively, to produce electrochemical reactions at elevated temperature. The electrochemical reactions involved include,

Anode: $H_2 + O^{2-} \rightarrow H_2O + 2e^-$ (1)

Cathode: $\frac{1}{2}O_2 + 2e^- \rightarrow O^{2-}$ (2)

Overall: $H_2 + \frac{1}{2}O_2 \rightarrow H_2O$ (3)

The power capacity of a single SOFC is limited. To obtain a higher power density for electrical application, it is necessary to connect a number of unit cells in series through interconnects. Figure 2 shows the structural scheme of a planar SOFC stack [4]. A unit cell is composed of a positive electrode-electrolyte-negative electrode (PEN) plate, interconnects, a nickel mesh, and sealants. The interconnects separate fuel and oxidant gasses and connect individual cells in series. They must be stable in both oxidizing and reducing environments, and be compatible with other SOFC components for long-term operation at high temperatures. A nickel mesh is inserted, between an interconnect and PEN plate, to work as an electrical connector and a fuel gas manifold. In a planar SOFC stack, the high temperature hermetic sealant

plays an important role in keeping fuel and oxidant from mixing and leakage during operation. Undesired chemical interaction and mismatch of coefficient of thermal expansion (CTE) between sealant and interconnect may damage SOFC stacks and degrade the electrochemical performance [5-7]. Therefore, development of sealant for SOFC applications is one of the challenges to meet the reliability target.

1.2 Glass Sealant

Sealing designs developed for SOFC include rigid seals and compressive seals [3,8,9]. For the compressive type of sealing such as mica-based sealants, the major advantage is that these seals are not rigidly fixed to other SOFC components. However, maintenance of gas-tight compressive sealing requires application of an external constant load during operation. On the other hand, rigid seals, such as glass and glass-ceramic sealants, form a joint with neighboring components without external load. Therefore, the important requirement for a rigid seal is that the seal's thermal expansion should closely match that of neighboring components. After melting and cooling down to room temperature, glass and glass-ceramic seals are brittle and susceptible to cracking because of tensile stresses generated during non-equilibrium thermal events with thermal mismatches.

Recently, a new joining approach known as bonded compliant seal (BCS) has been developed for planar SOFC stacks [10]. A thin, deformable metal foil is used to bond the neighboring metallic and ceramic components. The flexible metal is able to relieve the effects of differential thermal expansion between the metallic support structure and the ceramic cell by ‘‘trapping’’ much of stress as elastic or plastic strain within the foil. The cell stresses in this type of seal are predicted to be much lower than other designs. After thermal cycle testing, BCS shows original hermeticity and bond strength with a significant mismatch of CTE between the two materials [10]. Since an exact match of CTE between adjacent components is not required, it provides a much wider range of alloy compositions to be used in the planar SOFC interconnect. However, more work is needed to understand the effects of the BCS design variables on the stresses and strains that arise in the components, particularly foil stiffness and geometry [11].

Because of generally lower price and easy fabrication, glass sealants are commonly used in planar SOFC stacks. Glass transition temperature (T_g) of glass and glass-ceramic sealants is an important factor to select a suitable

sealant for SOFC. At operating stage, the temperature of SOFC stacks is higher than T_g such that glass and glass-ceramic sealants become viscous [3,11]. This key mechanism offers good wetting behavior to form a well adherent bond during joining process, but it should not soften too much to flow during operation for a gas-tight seal. Therefore, T_g of the glass system used as a sealant in SOFCs must be lower than the operating temperature. To overcome the weakness of glass, glass-ceramics were developed for SOFC applications by means of changing the microstructure of glass. Glass-ceramics are a composite which consists of amorphous and crystalline phases. During sintering process and operation, the amorphous glassy phase transforms into crystalline phases. Strength of the resultant sealant becomes stronger than that of the initial state so that glass-ceramics have better mechanical properties and higher viscosity than glasses to withstand thermal stresses. Because of the mismatch of CTE between these two phases, thermal stress may develop and generate cracks, microvoids, or fracture. However, the viscosity and flowability of the amorphous phase could relax the thermal stress caused by thermal mismatch at operation. Both sealant composition and thermal events could affect crystallization of a glass so that controlling the crystallization is important to have suitable viscosity and wetting behavior and to have sufficient integrity during operation for an SOFC sealant.

Phosphate, borosilicate, boro-aluminosilicate, silicate glasses and glass-ceramics have been developed and evaluated for use in planar SOFC [3,8,12]. BaO-CaO-Al_2O_3-SiO_2 (BCAS) glass systems have been developed and investigated [5,13-19], with a focus on a commercial BCAS glass, designated as G-18 (35 mol% BaO, 35 mol% SiO_2, 15 mol% CaO, 10 mol% B_2O_3, and 5 mol% Al_2O_3). In the cases of barium-containing glass-ceramics for SOFC, CTE is increased by crystallization and formation of barium silicate ($BaSiO_3$) [3]. Because of a lower activation energy of barium [3], crystallization of a barium-containing glass is faster than that of one containing other alkaline-earth metal elements. The influences of each constituent in a glass-ceramic sealant have been investigated [3]. Barium is commonly used as a modifier in silicate glasses. Boron oxide and zirconia can reduce T_g and CTE ,respectively [3].

A new glass-ceramic sealant (designated as GC-9) containing BaO, B_2O_3, Al_2O_3, and SiO_2 for intermediate-temperature planar SOFC (IT-pSOFC) at 700 ℃-750 ℃ has been developed at the Institute of Nuclear Energy Res earch (INER). The properties of CTE, viscosity, crystallization, and chemical interaction between this sealant and other planar SOFC components

(electrolyte, electrode, interconnect, and frame) have been investigated [20-22]. Mechanical properties of GC-9 at various temperatures were investigated by Chang [23]. In the study of Chang [23], in order to generate different degrees of crystallization, GC-9 samples were sintered at 850 ℃ and then aged at 750 ℃ for 4 h and 100 h, designated as non-aged and aged, sintered GC-9, respectively. Results of Chang [23] revealed that the extent of crystallization was increased with an increasing aging time, while the types of crystalline phase were not changed. Because of a crack healing effect, there was a significant improvement of flexural strength as compared to the room-temperature strength at a high temperature below T_g [23]. Mechanical strength of the aged GC-9 was increased; however, a less amount of amorphous phase could diminish the ability for relaxing thermal stresses at high temperature. However, the strength and stiffness of both aged and non-aged GC-9 glass-ceramics were decreased at temperature above T_g.

1.3 Joint of Glass-Ceramic Sealant and Metallic Interconnect

Both ceramic and metallic materials have been used as interconnect for SOFCs. Ceramic interconnects are made of semiconducting oxides with good stability in air and are generally compatible with other ceramic components [24]. The electrical conductivity of ceramic interconnects increases with temperature, which is suitable for the high-temperature SOFC. In lower temperature, the lower electrical conductivity of ceramic interconnects is a challenge in IT-pSOFC system. Metallic interconnects are excellent electrical conductors, while the poor oxidation resistance of metal forms oxide scales so that the electrical conductivity would degrade [24]. However, metallic interconnects are favored for IT-pSOFC over the expensive ceramic ones due to their low cost and easy fabrication [24].

In IT-pSOFC systems, glass-ceramic sealants are commonly used to join interconnects and cells. Figure 3 [8] shows the locations where seals are used in a planar SOFC stack with metallic internal gas manifolds and metallic interconnects. Common seals include: (a) cell to metal frame; (b) metal frame to metal interconnect; (c) frame/interconnect pair to electrically insulating spacer; (d) stack to base manifold plate [8]. Seals (b) and (d) can be referred to as a joint of glass-ceramic sealant and metallic interconnect.

In a planar SOFC stack, the joint of glass-ceramic sealant and metallic interconnect is exposed to oxidizing and reducing environments during operation. The difference in environment affects interactions between the

joining components. Interactions of glass sealant with metallic interconnect may influence the chemical stability of a joint due to internal diffusion of anions and cations. Therefore, the joining behavior of various sealants with ferritic chromia-forming alloys under simulated SOFC environments have been studied [5,14-16,18,25-39]. Some studies were carried out using a single exposure atmosphere, either air (or moist air) representing the cathode-side environment, or a reducing atmosphere simulating the anode-side environment. Recently, some investigations [5,14,28,30,36] were conducted under dual-atmosphere conditions that closely simulate the exposure condition of joint during SOFC operation to determine the interaction between seal and interconnect. Unfortunately, interactions such as undesirable chromate formation [14,16,18,25-29,32,35,37,39] and electrical short-circuiting [5,14,28,30,36] are difficult to avoid if ferritic chromia-forming alloys are applied as the interconnect. Chromate is a large scale in an oxidizing environment and absent in a reducing environment [14,18,29,39]. However, internal oxidation in the metal substrate is found near the three-phase boundary of hydrogen/glass–ceramic sealant/steel [5,28,29,32].

During cyclic operation of SOFC, generation of thermal stresses leads the seals to be subjected to tensile and shear stresses [40-43]. Interactions of glass or glass-ceramic sealant with metallic interconnect in planar SOFCs also influence the mechanical properties of the joint of these materials. Once the thermal stress exceeds the corresponding strength of the joint, seals may fail leading to degradation of cell performance. For assessment of the structural reliability of an SOFC stack, it is necessary to investigate the mechanical properties of the joint of glass-ceramic sealant and metallic interconnect in both oxidizing and reducing environments.

The mechanical properties of a joint do not belong to that of a single material due to the multi-layer structure and therefore they are interfacial properties between dissimilar materials. The joint strength between glass-ceramic sealant and metallic interconnect in SOFC has been characterized using various testing techniques. In the study of Weil et al. [16], a modified rupture testing technique was developed by placing a sealed disk specimen in a test fixture and pressurizing the backside of the sample until rupture of seal in air at room temperature. The results revealed that alumina-forming ferritic steel substrates offered greater bond strength with G-18 glass sealant [16]. The barium chromate layer that developed on the chromia-forming steels exhibited a poorer thermal expansion match and

tended to grow to a greater thickness than the celsian zone observed on the alumina-formers [16]. Malzbender et al. [2] characterized the shear strength of the joint between a glass-ceramic sealant (BCAS) and a metallic interconnect (Crofer 22 APU) in air at the operation temperature of 800℃ by a symmetric shear test. At the operation temperature, as-joined specimens exhibited viscous shear deformation while the viscous shear deformation became more difficult for additionally crystallized specimens [2]. The tensile joint strength between a glass-ceramic (SiO_2-Al_2O_3-CaO-Na_2O, SACN) and a metallic interconnect (Crofer 22 APU) in oxidizing and reducing environments was characterized at room temperature by Smeacetto et al. [32]. It was observed that fracture always occurred within the glass-ceramic and never at the interface of the joint [32]. The results of Chou et al. [18] showed that the tensile strength of joint between a (SrO, CaO)-Y_2O_3-B_2O_3-SiO_2 glass (YSO75) and a metallic interconnect (Crofer 22 APU) at room temperature drastically reduced after aging in air (850℃/500h) due to formation of $SrCrO_4$ at the outer sealing edges exposed to air. Besides, joint strength slightly increased after aging in wet reducing environment (850 ℃/250h) [18].

Stephens et al. [19] investigated the interfacial strength between G18 glass-ceramic and Crofer 22 APU substrate in air at temperatures ranging from 25 ℃ to 800 ℃ under both tensile and shear loading. Two failure modes were observed in the tensile test, glass bulk failure mode referring to failure occurring through the glass layer, and interfacial failure mode referring to failure occurring at the glass-metal interface [19]. Celikn [37] investigated the tensile joint strength between a glass-ceramic sealant and Crofer 22 APU substrate in air at room temperature under different bonding conditions. Temperature and pressure during the sintering process are found to be the most important parameters to produce a hermetic seal [37]. According to their results, the optimum sintering temperature and pressure are 870 ℃ and 0.5 kg cm^{-2}, respectively [37]. Timurkutluka et al. [38] evaluated the tensile joint strength between glass-ceramic sealant containing yttria stabilized zirconia (YSZ) and Crofer 22 APU substrate in air at room temperature after thermal cycling. Glass–ceramic powders are mixed with various amounts of YSZ to improve the thermal cycling stability by enhancing the devitrification resistance [38]. It was found that the mechanical performance of the samples without any YSZ showed the poorest thermal cycling stability due to the crystallization especially after 10 thermal cycles [38]. The fracture strength of the samples with 5% YSZ content showed almost a stable trend in spite of the

thermal cycles [38]. Therefore, the optimum YSZ content was found to be 5 wt% when thermal cycling behavior is considered [38].

In the studies of Chen [44] and Liu [45], the joint strength of GC-9 glass-ceramic sealant and Crofer 22 H interconnect steel was investigated under both tensile and shear loading in the oxidizing and reducing environments, respectively, at room temperature and 800 ℃. Some specimens of Chen [44] and Liu [45] were heat treated in in the oxidizing and reducing environments, respectively, at 800 ℃ for 1000 h. Both the tensile and shear joint strengths at room temperature are greater than those at 800 ℃ [44,45]. The fracture sites for non-aged specimens are the same in both oxidizing and reducing environments at room temperature and 800 ℃, because the exposure time in the given oxidizing or reducing atmosphere during mechanical testing is not long enough to affect the mechanical properties of a joint. The fracture sites for the non-aged tensile joint specimens are within the GC-9 layer at room temperature and 800 ℃; those for the non-aged shear joint specimens are at the metal/chromia and glass/chromate interfaces at room temperature and 800 ℃, respectively [44,45]. After thermal aging in the oxidizing and reducing environments, joint strength of the 1000 h-aged shear specimen at 800 ℃ is reduced, compared to the non-aged one. The fracture sites for the 1000 h-aged shear joint, when tested at 800 ℃ in oxidizing and reducing environments, are within the GC-9 layer. Because of CTE mismatch between ceramic and glass phases, micro-voids were formed in the glass-ceramic substrate with a greater extent of crystallization. Yeh [46] investigated the effect of Crofer 22 H coated with a thin lanthanum strontium manganite (LSM) layer on the shear and tensile joint strength at 800 ℃ in an oxidizing environment. There is a significant decrease in shear and tensile joint strength for samples with LSM coating because of generation of microvoids and micocracks in the chromate layer during sintering process [46]. The results of Chen [44], Liu [45], and Yeh [46] indicate that both tensile and shear joint strengths are lower than the flexural strength of GC-9 as they are associated with initiation and propagation of cracks at various interfaces.

1.4 Creep of Joint of Glass-Ceramic Sealant and Metallic Interconnect

Creep is normally regarded as deformation at a constant stress/load as a function of time and temperature [47]. Creep deformation can not be neglected for metals and crystalline ceramics at a high temperature in the range of 30 to 60% of the melting temperature (T_m) [48]. Figure 4 [48] shows

strain versus time during creep under constant load. There is an initial instantaneous response of elastic and perhaps plastic strain, then followed by a gradual accumulation of creep strain, as shown in Fig. 4 [48]. In the primary stage, the strain rate is relatively high. However, strain rate decreases and becomes constant when the primary stage is ended. The second stage is called steady-state creep. At the end of the secondary stage, strain rate increases in an unstable manner as rupture failure approaches [48]. Creep cavities may form inside the material and cause rupture in the tertiary stage. Figure 5 [48] shows stress versus time to rupture (t_r) during creep under constant load. A stress versus t_r plot is analogue to S-N curve for fatigue, except that the life is a rupture time rather than a number of cycles [48].

The high-temperature operation of pSOFC could generate significant thermal stresses due to mismatch of coefficient of thermal expansion (CTE) between components and temperature gradients in the SOFC system [40-43] so that components in pSOFC must be able to withstand the thermal cycling operation. They need to have long-term durability due to a difficulty to be repaired in a pSOFC stack. The thermal stresses may or may not cause an immediate failure of pSOFC structure, but they could generate creep damages in the components under a long-term high-temperature operation environment. Creep damages in the joint of a glass-ceramic sealant with metallic interconnect may eventually generate excessive deformation and/or cracking, leading to gas leakage and degradation of cell performance. Therefore, it is very important to investigate the creep properties of such a joint for assessing the structural integrity and durability of a pSOFC stack.

High-temperature creep properties have been studied individually for anodes [7], electrodes [49], glass-ceramic sealants [17,19,50-53], and metallic interconnects [54-58] for pSOFC applications. In a planar SOFC stack, there are oxidizing and reducing environments so that it is necessary to investigate the environmental effect on creep properties. Some of the precious studies are conducted in an oxidizing environment [7,17,19,50-58] and others are performed in a reducing environment [49,58].

Nanoindentation was applied to measure the elastic modulus, hardness, and creep properties of a G18 sealant glass from room temperature to 400 ℃ [17]. The results showed that elastic modulus slightly increased with temperature below 300 ℃. There was a significant jump of about 100% in elastic modulus from 300 ℃ to 400 ℃ in all of the variously crystallized specimens due to self-healing of cracks [17]. The samples with a longer aging time didn’t show a significant increase in creep deformation before it reached

the secondary stage. It indicated that specimens having a higher degree of crystallinity were more resistant to creep at high temperature [17]. At secondary state, there was no clear dependence of creep strain rate on aging time at a given testing temperature because the tests were performed below T_g (620 ℃ for G18). Under this condition, there was no phase change or viscoelasticity provided by glassy phase [17]. However, an increase in steady-state strain rate with temperature was found for each aging condition [17]. A research further studied the nanoindentation creep behavior of G18 at 25 ℃, 550 ℃, 650 ℃, and 750 ℃ using samples of different extents of crystallization [51]. One set of samples were sintered at 850 ℃ for 1 h, and aged at 750 ℃ for 4 h. Another set of samples were aged further for 100 h at 800 ℃. The results showed that the 4 h-aged sample had a greater elastic modulus than did the 100 h-aged one at room temperature [51]. Further aged samples contained micro-voids in glassy phases which surrounded the crystalline phase. These micro-voids which might cause cracking during cooling resulted in a lower elastic modulus for a 100 h-aged sample. Above 500 ℃, the 100 h-aged sample had a greater elastic modulus, compared to the 4 h-aged one, due to a self-healing effect of cracks [51]. The results also showed that creep deformation increased with temperature, especially above T_g. The 4 h-aged G18 which had less crystalline phases displayed more creep deformation than did the 100 h-aged one. The crystalline phases with a higher T_g were most likely to impede flow of the glassy phases [51].

Compressive tests with C-ring specimens have been carried out to assess the creep behavior of glass ceramic sealant for tubular SOFC [53]. C-rings, which develop upon loading from outer to inner surface a transition from tensile to compressive stresses, can easily be machined from the tubular specimens [53,59]. The results [53] reveal that creep effects are significant around or above T_g as verified for glass ceramic sealant. After thermal aging at 800 ℃ for 500 h in air, aged sealant displays less creep strain rate than the non-aged one at temperature above 850 ℃ [53]. It indicates that an increasing fraction of crystalline phase inside the sealant increases the creep resistance [53]. Boccaccini et al. [58] investigated creep behavior of porous metal (22% Cr-based stainless steel alloy) in both oxidizing and reducing environments. The creep experiments performed in an oxidizing environment show higher creep strain rates than in a reducing environment [58]. The weight gain of metal in an oxidizing environment is larger than that in a reducing environment [58]. It indicates that effect of oxide scale formation can affect the creep strain rate [58].

In the study of Lin [60], creep properties of the joint between GC-9 glass-ceramic sealant and Crofer 22 H interconnect steel were investigated under both tensile and shear loading in air at 800 ℃. It is observed that the creep rupture time is shorter than 10 h when the applied stress is about 1.6 MPa and above in both shear and tensile loading modes [60]. If the applied stress is less than 1.1 MPa, the creep rupture time is over 1000 h for both loading modes [60]. The shear creep strength at 1000 h is about 23% of the average shear joint strength at 800 ℃ [60]. The tensile creep strength at 1000 h is only about 9% of the average tensile joint strength at 800 ℃. For both shear and tensile joint specimens, creep cracking first takes place at the spinel/$BaCrO_4$ interface, followed by penetration through the $BaCrO_4$ layer and propagation along the interface between the chromate layer and glass-ceramic substrate [60]. Final fast fracture occasionally takes place within the glass-ceramic layer [60].

1.5 Purposes

The high operation temperature enables pSOFC to obtain a superior efficiency of energy conversion; however accompanying concerns, such as degradation of materials which results from undesirable reactions between components, affect the performance of pSOFC. The thermal stresses caused by considerable CTE mismatch between components and thermal gradients affect the structural durability of pSOFC. Excessive thermal stresses may lead to fracture of components endangering the mechanical integrity of a pSOFC stack. In a pSOFC stack, it is difficult to replace sealants bonded to adjacent components, such as interconnects and PENs when they fail or fracture. Therefore, a systematic investigation of mechanical properties of joints between the glass-ceramic sealant and metallic interconnect at room temperature and operation temperature is essential for development of a reliable pSOFC stack.

For those steels and glass-ceramics developed for SOFC applications, effects of environment on their joint characteristics, such as electrical performance, chemical properties, and long-term stabilities, have been widely investigated [5,14-16,18,25-39,44-46,60]. In those studies [18,19,32,37,38,44,46,60], the joint strength and creep behavior in oxidizing environment have been investigated. However, there are only a limited number of studies focused on the effect of reducing environment on the mechanical properties of the joint between interconnect and sealant [18,45].

Therefore, information about the effect of reducing environment on the long-term high-temperature creep behavior of such a joint is still lack. For these reasons, the objective of this study is to investigate the effect of reducing environment on the creep properties of a joint between a glass-ceramic sealant and an interconnect steel. Two loading modes, tensile and shear forces, are applied to characterize the creep properties of the joint at 800 ℃ in wet hydrogen. In addition, some samples are also tested after aging at 800 ℃ in wet hydrogen to simulate the SOFC working environment. Fractographic and microstructural analyses are conducted with scanning electron microscopy (SEM) and correlated with the creep testing results. It is hoped that results of the current study and previous work [44-46,60] can provide some useful information for assessing the long-term structural reliability of planar SOFC stacks.

2. MATERIALS AND EXPERIMENTAL PROCEDURES

2.1 Materials and Specimen Preparation

In order to simulate the conditions of a joint subjected to thermal stresses at SOFC operation temperature, two types of sandwich-like specimens (metal/sealant/metal) are designed in this study for determining the creep properties of the joint and investigating the interfacial reactions. In the present work, metallic parts of the joint specimens are made of a commercial ferritic stainless steel, Crofer 22 H (ThyssenKrupp VDM GmbH, Werdohl, Germany), which is a heat-resistant alloy developed for application in SOFCs. Chemical compositions and mechanical properties of the Crofer 22 H alloy are listed in Tables 1 and 2 [61], respectively. For Crofer 22 H, the yield strength, ultimate tensile strength, and Young's modulus are decreased, while the elongation is increased with an increase in temperature, as shown in Table 2 [61]. The GC-9 glass sealant used was developed at INER for intermediate-temperature planar SOFC. The major chemical composition of the GC-9 glass sealant includes 34 mol% BaO, 34 mol% SiO_2, 9.5 mol% B_2O_3, 12 mol% CaO, 5 mol% La_2O_3, 4.5 mol% Al_2O_3, and 1 mol% ZrO_2 [62]. It was made by mixing the constituent oxide powders followed by melting at 1550 ℃ for 10 h. After melting, it was poured into a mold preheated to 680 ℃ to produce GC-9 glass ingots. The GC-9 glass ingots were then annealed at 680 ℃ for 8 h and cooled down to room temperature. GC-9 glass powders were made by crushing the as-cast glass ingots and sieving with 325 mesh sieves. The average size of the glass powder is 45 μm. Slurries were made by adding into the GC-9 powders the desired amounts of solvent (alcohol), binder (ethyl celluloid), and plasticizer (polyethylene glycol). Table 3 [46] lists the average biaxial flexural strength of the sintered GC-9 glass at various temperatures.

Figure 6 shows the scheme of two types of joint specimens for tensile test (Fig. 6(a)) and shear test (Fig. 6(b)), respectively. The as-received metal plates were cut into slices in the dimensions of 95 mm x 25 mm x 2.5 mm. A pin hole was drilled in each steel slice for applying pin loading. It is effective to minimize bending and twisting effects during a creep test by means of pin loading. For shear specimens, an edge of each steel slice was milled from the original thickness of 2.5 mm to 1 mm with an area of about 8 mm x 25 mm. After machining, a GC-9 glass slurry was spread on the joining region of each steel slice to make a half-specimen. The apparent joining areas are 25 mm x 2.5 mm and 25 mm x 6 mm for tensile and shear specimens, respectively. The

glass slurry was made of a mixture of glass powder dispersed in ethanol. The half-specimen was then put in a furnace at 70 ℃ to dry the slurry. A joint specimen was assembled by placing one half-specimen onto another half-specimen to form a Crofer 22 H/GC-9/Crofer 22 H sandwich specimen through appropriate heat treatments. In the assembling process, the joint specimens were firstly held at 500 ℃ for 1 h and heated to 900 ℃ followed by a hold time of 4 h. The heating rate at each heating step in the given assembling process is 5 ℃/min. For investigating the effect of environmental atmosphere on the joining quality, some samples were aged in a reducing atmosphere of wet hydrogen (H_2-7 vol% H_2O) at 800 ℃ for 1000 h. The aging treatment was carried out in a furnace attached with a quartz tube filled with desired gas. Photograph of this environmental furnace is shown in Fig. 7. The reducing atmosphere is generated using helium as a carrier gas to pass through water at 90 ℃ and then mix with pure hydrogen. During the heating step, the helium is used to purge the quartz tube continuously. After reaching 800 ℃, the wet hydrogen gas (H_2-7 vol% H_2O) starts to flow into the quartz tube for aging treatment. To avoid water condensation, gas lines are wrapped with a heating tape to maintain at a certain, warm temperature.

2.2 Creep Test

In order to understand the effect of reducing environment on the mechanical properties, a stainless steel tube (AISI 310), which was designed in house and made by a local machine shop, was attached to the specimen for mechanical test in wet hydrogen environment [45]. In the tube, the specimen is linked with the top and bottom extension rods by pins. In order to minimize bending and twisting during test, pin loading was applied in the tests. O-rings are placed at the ends of the tube for gas-tight purpose, as shown in Fig. 8. During the test, hydrogen with 7 vol% H_2O gas flows in and out of the attached tube to keep the entire tube filled with wet hydrogen gas. All of the creep tests at 800 ℃ are conducted in the given wet hydrogen environment using such an attachment for the specimen. A compact furnace was used to heat the central portion of the specimen and attachment, as shown in Fig. 8. Short-term creep tests were performed on a commercial closed-loop servo-hydraulic test machine (MTS 810) attached with a furnace by means of load control. Long-term creep tests (> 100 h) were conducted using a direct-load creep test machine. Photographs of the experimental setup for short-term and long-term creep tests are given in Fig. 9 and Fig. 10,

respectively.

In the creep test, various weights were used as the loading source. The values of the applied constant loads were selected to generate the magnitude of creep rupture time distributed in the orders of 1, 10, 100, and 1000 h. For the high-temperature creep tests, the specimens were heated to 800 ℃ with a rate of 5 ℃/min and held for 15 min to reach thermal equilibrium before applying force. During the heating step, the attached stainless tube was flushed with helium gas. When temperature reached 800 ℃, the tube was then filled with wet hydrogen.

2.2.1 Friction test

As O-rings are placed at the ends of the tube, friction between the O-ring and the extension rod may affect the load on the specimen. In order to count the effect of friction, it is necessary to measure the frictional force between the O-ring and the extension rod during mechanical test. In this way, the net force applied on a specimen is equal to the applied load minus the frictional force. The friction tests were conducted on a commercial closed-loop servo-hydraulic test machine (MTS 810) by means of displacement control with a loading rate of 0.001 mm/s to determine the frictional force.

2.3 Microstructural Analysis

After creep testing, fracture surface of each specimen was examined with an optical microscope to determine the true joining area. In order to investigate the characteristics of interfaces in the joint, some samples were cut along the longitudinal direction to observe the cross sections. The cross sections were finely polished to optical finish. SEM was also used to examine the interfacial morphology between the glass-ceramic sealant and metallic interconnect. The energy dispersive spectrometer (EDS) module was used for composition analysis in order to understand the elemental distribution in the glass-ceramic sealant and metallic interconnect. The creep fracture modes of the joint under tensile stress and shear stress were then characterized.

3. RESULTS AND DISCUSSION

Formation of adhesive oxide layers is the main mechanism of interfacial joining between the glass-ceramic and metallic interconnect. The bonding strength of the joint originates from the mutual van der Waals force of the formed oxide layers. The high-temperature joining mechanism of the GC-9 glass-ceramic and Crofer 22 APU alloy involves formation of two oxide layers with a Cr_2O_3 layer on the surface of Crofer 22 APU and a $BaCrO_4$ layer on the surface of GC-9 [21]. A spinel ($(Cr,Mn)_3O_4$) layer is formed between these two oxide layers. Similar oxide layers are expected to be formed between the given GC-9 and Crofer 22 H in the present study. Figure 11 shows the location of each oxide layer between Crofer 22 H and GC-9 glass-ceramic.

As sealants used in SOFC are exposed to both oxidizing and reducing environments during operation, it is important to understand the environmental effect on the creep properties at elevated temperature, especially for planar SOFCs which are expected to last for tens of thousands of hours with repeated thermal cycles. In the following discussion, some of the results in a reducing environment have been reported in the thesis of Liu [45]. In the study of Liu [45], effect of thermal aging in a reducing environment on the joint strength was investigated under shear and tensile loading at room temperature and 800 ℃. The shear joint strength has an average value of 6.8 MPa and 4.2 MPa at room temperature and 800 ℃, respectively, while the average tensile joint strength is of 31.3 MPa at room temperature and of 11.9 MPa at 800 ℃ [45]. A reducing aging-treatment at 800 ℃ for 1000 h enhances the joint strength of shear loading at room temperature by 24% and degrades it at 800 ℃ by 19%. A reducing aging-treatment at 800 ℃ for 1000 h increases the joint strength of tensile loading at room temperature by 47% and deteriorates it at 800 ℃ by 51% [45]. Figures 12 and 13 show the fracture pattern of shear and tensile specimens, respectively, when tested at 800 ℃ after 0 h, 100 h, and 1000 h of thermal aging [45]. The micrographs shown in Figs. 12 and 13 will be compared with the fracture patterns of the creep ruptured specimens of this study in the following discussion. In this study, some of the joined specimens were aged in wet hydrogen at 800 ℃ for 1000 h to assess the effect of aging treatment on the long-term durability of the joint. After aging treatment, the aged specimens were tested under constant loading at 800 ℃ in a reducing environment.

3.1 Non-aged Joint of Glass-Ceramic Sealant and Metallic Interconnect

3.1.1 Creep rupture behavior

Creep rupture characteristics of the non-aged joint of GC-9 glass-ceramic sealant and Crofer 22 H interconnect subjected to constant shear and tensile loads at 800 ℃ are shown in Fig. 14 by plotting the applied stress versus creep rupture time. As shown in Fig. 14, the relationship between the applied stress and creep rupture time can be well described by a simple power law for each loading mode. The fitted equation and correlation coefficient (r) for each loading mode in Fig. 14 are expressed as follows,

shear loading: $\tau t_r^{0.096} = 1.50, \quad r^2 = 0.93$ (4)

tensile loading: $\sigma t_r^{0.50} = 2.52, \quad r^2 = 0.97$ (5)

where τ and σ, respectively, are the applied shear and tensile stresses in unit of MPa and t_r is time to rupture in unit of h. The creep rupture time for the joint specimen subjected to a constant shear or tensile load at 800 ℃ can be estimated through these power-law relations thanks to the high correlation coefficient values. As shown in Fig. 14, the creep rupture time increases with a decrease in applied stress for both loading modes. With an applied constant stress of about 1.2 MPa and 0.8 MPa, respectively, for shear and tensile loading modes, the creep rupture time is less than 10 h according to Eqs. (4) and (5). On the other hand, for a creep rupture time longer than 1000 h, the applied constant stress should be smaller than 0.77 MPa and 0.08 MPa for shear and tensile loading modes. The shear creep strength of non-aged joint at 1000 h in H_2-7 vol% H_2O is about 18% of the average shear strength (4.2 MPa) [45], and the tensile creep strength at 1000 h is only about 0.67% of the average tensile strength (11.9 MPa) [45].

3.1.2 Failure analysis

Figure 15 shows the failure patterns in the shear specimens tested at 800 ℃. As shown in Fig. 15(a), for a creep rupture time of 0-1 h, cracks initiated at the glass-ceramic layer at the periphery of the joining area, propagated at

the interface between the Cr_2O_3 chromia layer and $BaCrO_4$ chromate layer, and then propagated inward through the interface between the chromia layer and the GC-9 glass-ceramic, followed by final, fast fracture at the inner glass-ceramic layer. Evidences of microstructural observation for selected regions in the fracture surfaces of Fig. 15(a) are provided as follows. Optical and SEM micrographs of four outlined regions of the fracture surface in the upper micrograph of Fig. 15(a) are shown in Fig. 16. Relevant EDS results of Fig. 16(b), 16(c), and 16(d) are shown in Fig. 17. Figure 16(b) and 16(e) show a microstructure of the GC-9 glass-ceramic. Needle-shape crystalline phases (α-$Ba(Al_2Si_2O_8)$) are observed in Fig. 16(b) and 16(e), indicating the fracture surface is covered with a glass-ceramic layer. As Ca, Ba, Al, Si, and O, which are the main composites of GC-9, are detected in Fig. 17(a), the microstructure presented in Fig. 16(b) indeed is the GC-9 glass-ceramic. Chromate ($BaCrO_4$) is identified in Fig. 16(c). By means of EDS analysis, Cr, Ba, and O elements are detected in Fig. 17(b), indicating that this region is a $BaCrO_4$ chromate layer. Ca, Ba, Al, Si, O, and Cr elements (Fig. 17(c)) are detected for the microstructure present in Fig. 16(d), so it is the GC-9 glass-ceramic with peeled Cr_2O_3 chromia. Figure 18 shows the optical and SEM micrographs of the four outlined counterpart regions on the fracture surface in the lower micrograph of Fig. 15(a). The counterparts of Regions 1, 2, 3, and 4 in Fig. 16(a) are shown in Region 1, 2, 3, and 4 in Fig. 18(a), respectively. Figure 18(b) and 18(e) show microstructures of the GC-9 glass-ceramic, while Figure 18(c) and 18(d) show microstructures of the Cr_2O_3 chromia layer.

Cross-sectional views of the interfacial microstructure between GC-9 and Crofer 22 H are shown in the SEM micrographs of Fig. 19 with back-scattered electron (BSE) mode [45]. As shown in Fig. 19(a), the upper zone is the Crofer 22 H, while the lower region is the glass-ceramic sealant. The left side of Fig. 19(a) is the edge of the joint, which is close to the exposing environment, and the right side of that is the center of the joint. As the joint specimen was sintered in air, a $BaCrO_4$ chromate layer is found at the edge of the joint, as shown in Fig. 19(b). However, the $BaCrO_4$ chromate layer is barely found in the SEM micrograph of the central region of the joint, as shown in Fig. 19(a). The $BaCrO_4$ chromate layer is presumably too thin to be observed due to a less amount of oxygen available in the inner central region. As shown in Fig. 19(c), a Cr_2O_3 chromia layer between the $BaCrO_4$ chromate and Crofer 22 H is found. A Cr_2O_3 layer was indeed formed on the Crofer 22 H side during the joining process between GC-9 and Crofer 22 H.

Therefore, the cracking path near the central portion of fracture surface (Region 3) present in Fig. 16(a) is along the interface between Cr_2O_3 and GC-9.

For a creep rupture time of 1-10 h, cracking first took place peripherally at the interface between the Cr_2O_3 layer and $BaCrO_4$ layer and then in the glass-ceramic substrate, and then proceeded at the interface between the Cr_2O_3 layer and the GC-9 glass-ceramic, as shown in Fig. 15(b). Optical and SEM micrographs of three outlined regions of the fracture surface in the upper micrograph of Fig. 15(b) are shown in Fig. 20. Figure 20(b) shows a microstructure of the $BaCrO_4$ chromate layer, and the glass-ceramic layer with needle-shape crystalline phases (α-$Ba(Al_2Si_2O_8)$) is observed in Fig. 20(c). The GC-9 glass-ceramic with peeled Cr_2O_3 chromia is shown in Fig. 20(d). Figure 21 shows the optical and SEM micrographs of the three outlined counterpart regions on the fracture surface in the lower micrograph of Fig. 15(b). The counterparts of Regions 1, 2, and 3 in Fig. 20(a) are shown in Regions 1, 2, and 3 in Fig. 21(a), respectively. Figure 21(b) and 21(d) show a microstructure of the Cr_2O_3 layer, while Figure 21(c) shows the GC-9 glass-ceramic with needle-shape crystalline phases (α-$Ba(Al_2Si_2O_8)$).

As shown in Fig. 15(c), for a creep rupture time of 10-100 h, the fracture pattern is almost the same as that in Fig. 15(b). Figures 22 and 23 show the optical and SEM micrographs of three outlined regions of the fracture surface in the upper and lower micrographs, respectively, of Fig. 15(c). The microstructure present in Fig. 22(b) is the $BaCrO_4$ chromate layer which is similar to that in Fig. 20(b). Figures 22(c) and 22(d) are the GC-9 glass-ceramic substrate. The Regions 1, 2, and 3 in Fig. 23(a) are the counterparts of Regions 1, 2, and 3 in Fig. 22(a). The fractography feature is the Cr_2O_3 layer in Figs. 23(b) and 23(c), while that is the GC-9 glass-ceramic in Fig. 23(c). As shown in Fig. 15(c) for a longer creep rupture time, the white area of GC-9 glass-ceramic is smaller than that in Fig. 15(b).

As shown in Fig. 15(d) for a creep rupture time of 100-1000 h, the central part of the fracture surface is the GC-9 glass-ceramic, and the periphery of the fracture surface is the Cr_2O_3 layer. Figures 24 and 25 show the optical and SEM micrographs of two outlined regions of the fracture surface in the upper and lower micrographs, respectively, of Fig. 15(d). The SEM micrographs of the Region 1 in both Figs. 24 and 25 are the Cr_2O_3 layer, while those of Region 2 in both Figs. 24 and 25 are the GC-9 glass-ceramic. Figure 15(e) shows the fracture surfaces with a creep rupture time over 1000 h. Fracture occurred within the glass-ceramic and at the interface between the

Cr_2O_3 layer and the GC-9 glass-ceramic for the specimen present in Fig. 15(e). The fracture pattern of Figure 15(e) is almost the same as that of Figure 15(d). Optical and SEM micrographs of two outlined regions of the fracture surface in the upper micrograph of Fig. 15(e) are shown in Fig. 26. Figures 26(b) and 26(c) show the glass-ceramic layer with needle-shape crystalline phases (α-$Ba(Al_2Si_2O_8)$). Figure 27 shows the optical and SEM micrographs of the two outlined counterpart regions on the fracture surface in the lower micrograph of Fig. 15(e). The counterparts of Regions 1 and 2 in Fig. 26(a) are shown in Regions 1 and 2 in Fig. 27(a), respectively. Figures 27(b) shows the GC-9 glass-ceramic with needle-shape crystalline phases (α-$Ba(Al_2Si_2O_8)$), while Figure 27(c) shows a microstructure of the Cr_2O_3 layer.

The failure patterns of tensile specimens tested at 800 ℃ are shown in Fig. 28. Figure 28(a) shows that fracture for a rupture time of 0-1 h occurred within the glass-ceramic layer and at the interface between the Cr_2O_3 layer and the GC-9 glass-ceramic. Figure 29 shows the optical and SEM micrographs of two outlined regions in the upper micrograph of Fig. 28(a). Two distinct zones, white and green, in the outlined regions of Fig. 29(a) represent the GC-9 glass-ceramic substrate. The microstructure of needle-shape crystalline phase is present in Fig. 29(b) and 29(c). Optical and SEM micrographs of the two outlined counterpart regions in the lower micrograph of Fig. 28(a) are shown in Fig. 30. Figure 30(b) and 30(c) show the microstructures of GC-9 glass-ceramic substrate and the Cr_2O_3 layer, respectively.

The rupture time of 1-10 h shows a similar fractography morphology to that of 0-1 h. Optical and SEM micrographs of outlined regions of the fracture surface in the micrographs of Fig. 28(b) are shown in Figs. 31 and 32. Similar to Fig. 29(b) and 29(c), the GC-9 glass-ceramic is present in Figs. 31(b) and 31(c), while the Cr_2O_3 layer and the GC-9 glass-ceramic which are present in Fig. 30(b) and 30(c) are also present in Fig. 32(c) and 32(b), respectively. Fracture for the rupture time of 10-100 h occurred at the interface between the Cr_2O_3 layer and the GC-9 glass-ceramic, as shown in Fig. 28(c). The GC-9 glass-ceramic and the Cr_2O_3 layer are shown in Figs. 33(b) and 34(b), respectively.

The fracture for the rupture time over 100 h occurred within the GC-9 glass-ceramic layer, as shown in Fig. 28(d) and 28(e). In Fig. 28(d) and 28(e), the fracture surfaces have a green color. Figure 28(d) shows the fracture surfaces of a rupture time of 100-1000 h, while the rupture time for Figure

28(e) is over 1000 h. Optical and SEM micrographs of outlined regions of the fracture surface in the upper and lower micrographs of Fig. 28(d) are shown in Figs. 35 and 36, respectively. Figures 35(b) and 36(b) show the GC-9 glass-ceramic microstructure with needle-shape crystalline phases (α-Ba($Al_2Si_2O_8$)). Figures 37(b) and 38(b) show optical and SEM micrographs of outlined regions of the fracture surface in the micrographs of Fig. 28(e) and no needle-shape crystalline phases are found in the glassy regions. Figure 39 shows a cross-sectional view of the microstructure in the specimen of Fig. 28(e). As shown in Fig. 39, the upper zone is the glass-ceramic sealant, while the lower zone is the Crofer 22 H. In the region of the glass-ceramic sealant, there exist the needle-shape crystalline phases (α-Ba($Al_2Si_2O_8$)), indicating the fracture occurring in the GC-9 glass-ceramic substrate.

3.2 1000 h-aged Joint of Glass-Ceramic Sealant and Metallic

3.2.1 Creep rupture behavior

After 1000-h thermal aging, creep rupture characteristics of the joint of GC-9 glass-ceramic sealant and Crofer 22 H interconnect subjected to constant shear and tensile loads at 800 ℃ are shown in Fig. 40 by plotting the applied stress versus creep rupture time. As shown in Fig. 40, the relationship between the applied stress and creep rupture time is well described by a simple power law for each loading mode. The fitted equation and correlation coefficient (r) for each loading mode in Fig. 40 are given in the following,

shear loading: $\tau t_r^{0.21} = 1.07, \quad r^2 = 0.81$ (6)

tensile loading: $\sigma t_r^{0.45} = 0.58, \quad r^2 = 0.89$ (7)

As shown in Fig. 40, the creep rupture time increases with a decrease in applied stress for both loading modes. With an applied constant stress greater than about 0.65 MPa and 0.21 MPa, respectively, for shear and tensile loading modes, the creep rupture time is less than 10 h according to Eqs. (6) and (7). For a creep rupture time to be longer than 1000 h, the applied constant stress should be smaller than 0.25 MPa and 0.03 MPa for shear and tensile loading

modes, respectively. For the GC-9/Crofer 22 H joint thermally aged at 800 ℃ in H_2-7 vol% H_2O for 1000 h, the shear creep strength at 1000 h is about 7.3% of the average shear strength (3.4 MPa) [45], while the tensile creep strength at 1000 h is only about 0.6% of the average tensile strength (5.1 MPa) [45].

3.2.2 Failure analysis

For creep rupture time of 0-1 h, 1-10 h, and 10-100 h, fracture of the 1000 h-aged shear specimens occurred within the GC-9 glass-ceramic layer, as shown in Fig. 41, which is similar to that of Fig. 15(d) and 15(e). Figure 42 shows the fracture pattern of 1000 h-aged tensile specimens with various creep rupture times indicating cracking within the GC-9 glass-ceramic substrate, which is comparable to that of Fig. 28(d) and 28(e). Apparently, after a thermal aging of 1000 h in wet hydrogen, glass-ceramic layer becomes the weakest path for cracking resistance regardless of loading mode and loading time.

3.3 Effects of Thermal Aging in Reducing Environment

As the service life of planar SOFCs is expected for 40,000 h or more, it is important to know the effect of reducing environment on the structural integrity of the joint. During the creep test, non-aged shear and tensile specimens are exposed to H_2-7 vol% H_2O at 800 ℃ and go through an in-situ thermal aging under loading. Fracture pattern of non-aged shear specimen with a creep rupture time of 0-1 h in Fig. 15(a) is the same as that of shear strength testing specimen without a thermal aging treatment (Fig. 12(a) [45]). As shown in Fig. 15(b) and 15(c), the fracture sites of non-aged shear specimen with a creep rupture time of 1-10 h and 10-100 h are similar as mentioned above. The fracture site of non-aged shear specimen with a creep rupture time of 10-100 h in Fig. 15(c) is the same as that of Fig. 12(b) [45] for shear strength testing specimen with a 100-h thermal aging treatment. Fracture of non-aged shear specimen with creep rupture time over 100 h (Fig. 15(d) and 15(e)) occurred within the GC-9 layer, which is similar to that of shear strength testing specimen with a 1000-h thermal aging treatment (Fig. 12(c) [45]).

As shown in Fig. 13(a) and 13(b) [45], the fracture sites for tensile strength testing specimen with no and a 100-h thermal aging treatment are within the glass-ceramic layer and at the interface between Cr_2O_3 and GC-9

glass-ceramic, respectively. Fracture pattern of non-aged tensile specimen with a creep rupture time of 0-1 h and 1-10 h, as shown in Fig. 28 (a) and 28(b), is a mixture of that in Fig. 13(a) and 13(b). The fracture site for a creep rupture time of 10-100 h (Fig. 28(c)) is comparable to that of tensile strength testing specimen with a 100-h thermal aging treatment (Fig. 13(b) [45]). Fracture of non-aged tensile specimen with a creep rupture time over 100 h (Figs. 16(d) and 16(e)) occurred within the GC-9 layer, which is similar to that of tensile strength testing specimen with a 1000-h thermal aging treatment (Fig. 13(c) [45]). Again, for the non-aged shear and tensile creep specimens, they undergo through an in-situ thermal aging during creep test.

For both non-aged tensile and shear specimens with a short creep rupture time less than 10 h, fracture mainly occurs within the GC-9 layer. For those with a creep rupture time of 10-100 h, fracture path changes to the interface between Cr_2O_3 and GC-9. With a creep rupture time over 100 h, fracture takes place within the GC-9 layer, again. It reveals that in-situ thermal aging during creep test enhances the cracking resistance of the GC-9 glass-ceramic at a short creep rupture time but deteriorates it at a long creep rupture time. In the results of the joint strength test [45], fracture of the joint with a long-term thermal aging treatment in the H_2-7 vol% H_2O also takes place within the GC-9 glass-ceramic layer regardless of loading mode.

In the study of Liu [45], after 100-h and 1000-h thermal aging in H_2-7 vol% H_2O, internal oxidation is found at the triple-phase boundary of metal/glass-ceramic sealant/wet hydrogen atmosphere, as shown in Figs. 43 and 44 [45]. Figures 45 and 46 show the cross-sectional SEM micrographs (BSE mode) of the interface of Crofer 22H/GC-9 in the non-aged tensile creep specimen of rupture time of 100-1000 h (Fig. 28(d)) and over 1000 h (Fig. 28(e)), respectively. Internal oxidation is also found at the triple-phase boundary in Figs. 45(b) and 46(b). Similar observations of internal oxidation at the triple-phase boundary are also reported in the study of Menzler et al. [29]. The internal oxidation may be attributed to an interaction of hydrogen/water vapor with the double oxide layer to form hydroxides or other volatile species [29]. Additionally, not only the aluminum and silicon in the interconnect but also the elements in the glass-ceramic may undergo the internal oxidation [28,29]. It is known that the SOFC operating conditions such as atmosphere, temperature, and time affect the interfacial stability. In general, air atmosphere promotes chromate phase formation and humidified hydrogen atmosphere promotes iron- and chromium-containing phase formation at the interface [28].

Comparison of the creep rupture life time between the non-aged and 1000 h-aged joint specimens in the given humidified hydrogen atmosphere is shown in Fig. 47. Apparently a thermal aging treatment of 1000 h in H_2-7 vol% H_2O significantly degrades the creep resistance of the GC-9/Crofer 22 H joint in both loading modes. This is attributed to a change in the cracking path of the joint specimens after a long-term thermal aging. Given a creep rupture time of 1000 h, the corresponding shear and tensile creep strength is 0.77 MPa and 0.08 MPa, respectively, for non-aged joint specimens and drops to 0.25 MPa and 0.03 MPa, respectively, for 1000 h-aged joint specimens. The shear creep strength at a rupture time of 1000 h of the thermally aged joint is only about 32% of that of the non-aged joint, and that is 38% for tensile loading mode. Table 4 lists the cracking path of creep fracture for non-aged joint specimens under shear and tensile loading, while the cracking path of 1000 h-aged joint specimens is listed in Table 5. As described above, four types of fracture site are observed in the crept specimens. Fracture occurring in the GC-9 substrate is designated as "A" in Tables 4 and 5. Fracture occurring at the interface between $BaCrO_4$ layer and Cr_2O_3 layer is designated as "B." Fracture occurring at the interface between glass-ceramic sealant layer and Cr_2O_3 layer is designated as "C." Fracture occurring in Cr_2O_3 layer is designated as "D." If fracture involves two sites, these two fracture sites are marked together. Some explanations for the observed behavior are given as follows.

Firstly, a thermal aging makes the amorphous glassy phase transform into crystalline phases and changes the flaw size and morphology of the GC-9 glass-ceramic. Therefore, the fracture site for the non-aged joint changes from the GC-9 glass-ceramic to the interface of Cr_2O_3/GC-9 with increasing creep rupture time up to 100 h. As shown in Fig. 48 [45], the content of main crystalline phase, alpha-Ba($Al_2Si_2O_8$), is estimated by calculating the average area proportion of the darker gray needles in fifteen SEM micrographs for each aged condition. As a result, the content of the crystalline alpha-Ba($Al_2Si_2O_8$) phase is approximately 23%, 32%, and 32%, in the non-aged, 100 h-aged, and 1000 h-aged GC-9, respectively [45]. Even through the content of the main crystalline phase in the 100 h-aged and 1000 h-aged GC-9 is the same, the main fracture site for the non-aged joint with creep rupture time over 100 h is within the GC-9 glass-ceramic layer, again. This is attributed to the second reason described below.

Secondly, water in glass has a great influence on a variety of properties for glass. For instance, water increases the rate of structural relaxation and

crystallization of glass [63-65]. In addition, water reduces the viscosity of the glass [63-65]. Therefore, for a longer time of in-situ thermal aging during creep test, water could diffuse into the GC-9 glass-ceramic to relax the structure. Therefore, for non-aged joint with a creep rupture time over 100 h, the GC-9 glass-ceramic layer becomes the weakest path for creep cracking. As shown in the Figs. 37(b) and 38(b), no needle-shape crystalline phases are found in the glassy regions, indicating crack goes through the amorphous phase of GC-9 due to a lower viscosity of the glass. Similarly, creep fracture of the 1000 h-aged joint specimens all takes place within the glass-ceramic layer regardless of loading mode and creep rupture time.

Thirdly, the study of Liu et al. [66] indicates that micro-voids are formed in the aged samples during a cooling process due to CTE mismatch between the crystalline and glassy phases. As shown in Fig. 48 [45], micro-voids (porosity) are estimated by calculating the average area proportion of black regions in fifteen SEM micrographs for each aged condition. The porosity ratio for the non-aged, 100 h-aged, and 1000 h-aged GC-9 is thus determined as 15%, 22%, and 22%, respectively [45]. The micro-voids provide a weak path for creep cracking such that fracture occurs mainly within the glass-ceramic layer for all of the 1000 h-aged joint specimens. This might explain why the 1000 h-aged joint shows an inferior creep resistance to that of the non-aged one, as shown in Fig. 47.

3.4 Effects of Environment on Creep Rupture Behavior

Comparison of the creep stress-life relationship for the non-aged GC-9/Crofer 22 H joint tested in air and H_2-7 vol% H_2O is shown in Fig. 49. Note that the data of air are taken from Ref. [60]. The fitted equation and correlation coefficient (r) for each loading mode tested in air in Fig. 49 are expressed as follows [60],

shear loading: $\tau t_r^{0.066} = 1.68, \quad r^2 = 0.90$ (8)

tensile loading: $\sigma t_r^{0.074} = 1.85, \quad r^2 = 0.97$ (9)

As shown in Fig. 49, in both loading modes, the creep resistance of the

non-aged joint is significantly degraded when the testing environment is changed from oxidizing atmosphere to reducing atmosphere. Given a creep rupture time of 1000 h, the corresponding shear and tensile creep strength is both 1.1 MPa in air [60] and drops to 0.77 MPa and 0.08 MPa, respectively, in H_2-7 vol% H_2O. For non-aged joint with a creep rupture time of 1000 h, the shear creep strength in H_2-7 vol% H_2O is about 70% of that in air, while the tensile creep strength in H_2-7 vol% H_2O is only about 7.27% of that in air. Because water in the given humidified hydrogen atmosphere reduces the viscosity of the glass, the structure of joint in H_2-7 vol% H_2O is weaker than that in air. As the joint area of a tensile specimen is smaller than that of a shear specimen, water could diffuse into the joint of a tensile specimen more easily. This might explain why the creep resistance of tensile specimen drops to a greater extent in H_2-7 vol% H_2O, compared to shear specimen.

Typical failure patterns for the non-aged shear and tensile crept specimens tested in air are shown in Figs. 50 and 51, respectively [60]. For both shear and tensile loading modes, cracking of the non-aged crept joint specimens in air initiated and grew at the spinel/chromate interface along the periphery of the joining area [60]. The crack then penetrated through the chromate layer and propagated along the interface between the chromate layer and glass-ceramic substrate [60]. Final fast fracture occasionally took place within the glass-ceramic layer [60]. The color of the peripheral joining area is yellowish, as shown in Figs. 50 and 51 due to existence of a chromate layer. With an increase in the amount of chromate left on the glass-ceramic substrate, color of the central fracture surface becomes a deep one such as red and brown [60]. As shown in Figs. 15 and 28, fracture surface of non-aged crept specimens in H_2-7 vol% H_2O shows green and white colors. EDS analysis results indicate the green fracture site exists the Cr_2O_3 chromia on the GC-9 glass-ceramic layer, as shown in Figs. 16(d). Cr_2O_3 is used in a wide range of green pigments, coating materials for thermal protection, catalysts, glass production, and lithium-ion batteries [67] However, the thickness of the Cr_2O_3 is around 0.2 mm, as shown in Fig. 19(c). Although the GC-9 glass-ceramic has a white color, the peeled Cr_2O_3 on the GC-9 shows a clear green color. The counterpart of the GC-9 is metal side with a slight green color, as the base metal has a gray color.

4. CONCLUSIONS

(1) For the creep test of non-aged joint specimens at 800 ℃ in H_2-7 vol% H_2O, the creep rupture time is shorter than 10 h when the applied stress is about 1.2 MPa and above in shear loading mode. If the applied shear stress is smaller than 0.77 MPa, the creep rupture time is over 1000 h. The shear creep strength of non-aged joint at 1000 h in the given wet hydrogen is about 18% of the average shear joint strength (4.2 MPa).

(2) For non-aged joint specimens tested under constant tensile loading at 800 ℃ in H_2-7 vol% H_2O, the creep rupture time is less than 10 h when the applied stress is greater than 0.8 MPa. For a creep rupture time longer than 1000 h, the applied tensile load should be smaller than 0.08 MPa. The tensile creep strength of non-aged joint at 1000 h in the given reducing atmosphere is about 0.67% of the average tensile joint strength (11.9 MPa).

(3) For both non-aged tensile and shear specimens with a short creep rupture time less than 10 h, fracture mainly occurs within the GC-9 glass-ceramic. For a creep rupture time of 10-100 h, fracture site changes to the interface between the Cr_2O_3 layer and the GC-9 glass-ceramic. For a creep rupture time over 100 h, the GC-9 glass-ceramic layer is the major fracture site, again.

(4) A thermal aging makes the amorphous glassy phase transform into crystalline phases and changes the flaw size and morphology of the GC-9 glass-ceramic. Therefore, the fracture site for non-aged joint changes from the GC-9 layer to the interface of Cr_2O_3/GC-9 with an increase of creep rupture time up to 100 h. For a longer in-situ thermal aging during creep test, water could diffuse into the GC-9 layer to relax glass-ceramic structure. Therefore, the GC-9 glass-ceramic layer becomes the weakest path for creep cracking in the non-aged joint with a creep rupture time over 100 h.

(5) For shear creep test of the 1000 h-aged joint specimens at 800 ℃ in H_2-7 vol% H_2O, the creep rupture time is less than 10 h for applied shear

stress of 0.65 MPa and above. If the applied shear stress is less than 0.25 MPa, the creep rupture time is over 1000 h. For the aged specimen, the shear creep strength at 1000 h is about 7.3% of the average shear strength (3.4 MPa).

(6) For tensile creep test of the 1000 h-aged joint specimens at 800 ℃ in H_2-7 vol% H_2O, the creep rupture time is shorter than 10 h for an applied tensile stress greater than 0.21 MPa. The applied tensile should be less than 0.03 MPa for creep rupture time longer than 1000 h. The tensile creep strength at 1000 h for the aged specimen is only about 0.6% of the average tensile strength (5.1 MPa).

(7) All of the creep fracture in the 1000 h-aged shear and tensile specimens takes place within the glass-ceramic layer regardless of loading mode and rupture time.

(8) For a creep rupture time of 1000 h in H_2-7 vol% H_2O, the shear and tensile creep strength of the thermally aged joint is about 32% and 38%, respectively, of those without a thermal aging. Micro-voids are formed in the aged samples during the cooling process due to CTE difference between the ceramic and glassy phases. The porosity ratio in the GC-9 layer of joint is higher after a 1000-h thermal aging in H_2-7 vol% H_2O. Therefore, thermally aged joint has a lower creep strength.

(9) The creep resistance of the non-aged joint is significantly degraded when the testing environment is changed from an oxidizing atmosphere to a reducing one. As water in the given humidified hydrogen could relax the joint structure, the shear creep strength at 1000 h in H_2-7 vol% H_2O is about 70% of that in air and the tensile creep strength at 1000 h in H_2-7 vol% H_2O is only about 7.27% of that in air.

REFERENCES

1. K. Kendall, N. Q. Minh, and S. C. Singhal, "Cell and Stack Designs," Chapter 8 in *High Temperature Solid Oxide Fuel Cells: Fundamentals, Design and Applications*, edited by S. C. Singhal and K. Kendall, Elsevier, Kidlington, UK, 2003.

2. J. Malzbender, J. Mönch, R. W. Steinbrech, T. Koppitz, S. M. Gross, and J. Remmel, "Symmetric Shear Test of Glass-Ceramic Sealants at SOFC Operation Temperature," *Journal of Materials Science*, Vol. 42, pp. 6297-6301, 2007.

3. J. W. Fergus, "Sealants for Solid Oxide Fuel Cells," *Journal of Power Sources*, Vol. 147, pp. 46-57, 2005.

4. W. Z. Zhu and S. C. Deevi, "A Review on the Status of Anode Materials for Solid Oxide Fuel Cells," *Materials Science and Engineering*, Vol. A362, pp. 228-239, 2003.

5. P. Batfalsky, V. A. C. Haanappel, J. Malzbender, N. H. Menzler, V. Shemet, I. C. Vinke, and R. W. Steinbrech, "Chemical Interaction Between Glass-Ceramic Sealants and Interconnect Steels in SOFC Stacks," *Journal of Power Sources*, Vol. 155, pp. 128-137, 2006.

6. Y. Zhao and J. Malzbender, "Elevated Temperature Effects on the Mechanical Properties of Solid Oxide Fuel Cell Sealing Materials," *Journal of Power Sources*, Vol. 239, pp. 500-504, 2013.

7. A. Nakajo, J. Kuebler, A. Faes, U. F. Vogt, H. J. Schindler, L.-K. Chiang, S. Modena, J. V. Herle, and T. Hocker, "Compilation of Mechanical Properties for the Structural Analysis of Solid Oxide Fuel Cell Stacks. Constitutive Materials of Anode-Supported Cells," *Ceramics International*, Vol. 38, pp. 3907-3927, 2012.

8. P. A. Lessing, "A Review of Sealing Technologies Applicable to Solid Oxide Electrolysis Cells," *Journal of Materials Science*, Vol. 42, pp. 3465-3476, 2007.

9. I. W. Donald, "Preparation, Properties and Chemistry of Glass- and Glass-Ceramic-to-Metal Seals and Coatings," *Journal of Materials Science*, Vol. 28, pp. 2841-2886, 1993.

10. K. S. Weil, J. S. Hardy, and B. J. Koeppel, "New Sealing Concept for Planar Solid Oxide Fuel Cells," *Journal of Materials Engineering and Performance*, Vol 15, pp. 427-432, 2006.

11. K. S. Weil and B. J. Koeppel, "Thermal Stress Analysis of the Planar

SOFC Bonded Compliant Seal Design," *International Journal of Hydrogen Energy*, Vol. 33, pp. 3976-3990, 2008.

12. K. S. Weil, "The State-of-the-Art in Sealing Technology for Solid Oxide Fuel Cells," *JOM*, Vol. 58, pp. 37-44, 2006.
13. S. R. Choi and N. P. Bansal, "Mechanical Properties of SOFC Seal Glass Composites," *Ceramic Engineering and Science Proceedings*, Vol. 26, pp. 275-283, 2005.
14. V. A. Haanappel, V. Shemet, I. C. Vinke, and W. J. Quadakkers, "A Novel Method to Evaluate the Suitability of Glass Sealant-Alloy Combinations under SOFC Stack Conditions," *Journal of Power Sources*, Vol. 141, pp. 102-107, 2005.
15. S. Ghosh, A. D. Sharma, P. Kundu, and R. N. Basuz, "Glass-Ceramic Sealants for Planar IT-SOFC: A Bilayered Approach for Joining Electrolyte and Metallic Interconnect," *Journal of the Electrochemical Society*, Vol. 155, pp. 473-478, 2008.
16. K. S. Weil, J. E. Deibler, J. S. Hardy, D. S. Kim, G.-G. Xia, L. A. Chick, and C. A. Coyle, "Rupture Testing as a Tool for Developing Planar Solid Oxide Fuel Cell Seals," *Journal of Materials Engineering and Performance*, Vol. 13, pp. 316-326, 2004.
17. J. Milhans, M. Khaleel, X. Sun, M. Tehrani, M. Al-Haik, and H. Garmestani, "Creep Properties of Solid Oxide Fuel Cell Glass-Ceramic Seal G18," *Journal of Power Sources*, Vol, 195, pp. 3631-3635, 2010.
18. Y.-S. Chou, J. W. Stevenson, and P. Singh, "Effect of Pre-Oxidation and Environmental Aging on the Seal Strength of a Novel High-Temperature Solid Oxide Fuel Cell (SOFC) Sealing Glass with Metallic Interconnect," *Journal of Power Sources*, Vol. 184, pp. 238-244, 2008.
19. E. V. Stephens, J. S. Vetrano, B. J. Koeppel, Y. Chou, X. Sun, and M. A. Khaleel, "Experimental Characterization of Glass-Ceramic Seal Properties and Their Constitutive Implementation in Solid Oxide Fuel Cell Stack Models," *Journal of Power Sources*, Vol. 193, pp. 625-631, 2009.
20. C.-K. Liu, T.-Y. Yung, and K.-F. Lin, "Effect of La Addition on the Thermal and Crystalline Properties of SiO_2-B_2O_3-Al_2O_3-BaO Glasses," *Proceedings of the Annual Conference of the Chinese Ceramic Society* (CD-ROM), 2007. (in Chinese)
21. C.-K. Liu, T.-Y. Yung, S.-H. Wu, and K.-F. Lin, "Study on a SiO_2-B_2O_3-Al_2O_3-BaO Glass System for SOFC Applications,"

Proceedings of the MRS_Taiwan Annual Meeting (CD-ROM), 2007. (in Chinese)

22. C.-K. Liu, T.-Y. Yung, and K.-F. Lin, "Isothermal Crystallization Properties of SiO_2-B_2O_3-Al_2O_3-BaO Glass," *Proceedings of the Annual Conference of the Chinese Ceramic Society* (CD-ROM), 2008. (in Chinese)
23. H.-T. Chang, "High-Temperature Mechanical Properties of a Glass Sealant for Solid Oxide Fuel Cell," Ph.D. Thesis, National Central University, Jhong-Li, Taiwan, 2010.
24. J. Fergus, R. Hui, X. Li, D. P. Wilkinson, and J. Zhang, *Solid Oxide Fuel Cells: Materials Properties and Performance*, CRC Press, New York, USA, 2008.
25. Z. Yang, J. W. Stevenson, and K. D. Meinhardt, "Chemical Interactions of Barium–Calcium–Aluminosilicate-Based Sealing Glasses with Oxidation Resistant Alloys," *Solid State Ionics*, Vol. 160, pp. 213-225, 2003.
26. Z. Yang, K. D. Meinhardt, and J. W. Stevenson, "Chemical Compatibility of Barium-Calcium-Aluminosilicate-Based Sealing Glasses with the Ferritic Stainless Steel Interconnect in SOFCs," *Journal of The Electrochemical Society*, Vol. 150, pp. 1085-1101, 2003.
27. Z. Yang, G. Xia, K. D. Meinhardt, K. S. Weil, and J. W. Stevenson, "Chemical Stability of Glass Seal Interfaces in Intermediate Temperature Solid Oxide Fuel Cells," *Journal of Materials Engineering and Performance*, Vol. 13, pp. 327-334, 2004.
28. V. A. C. Haanappel, V. Shemet, S. M. Gross, T. Koppitz, N. H. Menzler, M. Zahid, and W. J. Quadakkers, "Behaviour of Various Glass-Ceramic Sealants with Ferritic Steels under Simulated SOFC Stack Conditions," *Journal of Power Sources*, Vol. 150, pp. 86-100, 2005.
29. N. H. Menzler, D. Sebold, M. Zahid, S. M. Gross, and T. Koppitz, "Interaction of Metallic SOFC Interconnect Materials with Glass-Ceramic Sealant in Various Atmospheres," *Journal of Power Sources*, Vol. 152, pp. 156-167, 2005.
30. V. A. C. Haanappel, V. Shemet, I. C. Vinke, S. M. Gross, T. Koppitz, N. H. Menzler, M. Zahid, and W. J. Quadakkers, "Evaluation of the Suitability of Various Glass Sealant-Alloy Combinations under SOFC Stack Conditions," *Journal of Materials Science*, Vol. 40, pp. 1583-1592, 2005.
31. F. Smeacetto, M. Salvo, M. Ferraris, J. Chob, and A. R. Boccaccini, "Glass-Ceramic Seal to Join Crofer 22 APU Alloy to YSZ Ceramic in

Planar SOFCs," *Journal of the European Ceramic Society*, Vol. 28, pp. 61-68, 2008.

32. F. Smeacetto, M. Salvo, M. Ferraris, V. Casalegno, P. Asinari, and A. Chrysanthou, "Characterization and Performance of Glass-Ceramic Sealant to Join Metallic Interconnects to YSZ and Anode-Supported-Electrolyte in Planar SOFCs," *Journal of the European Ceramic Society*, Vol. 28, pp. 2521-2527, 2008.

33. T. Jin and K. Lu, "Compatibility between AISI441 Alloy Interconnect and Representative Seal Glasses in Solid Oxide Fuel/Electrolyzer Cells," *Journal of Power Sources*, Vol. 195, pp. 4853-4864, 2010.

34. Y.-S. Chou, E. C. Thomsen, R. T. Williams, J.-P. Choi, N. L. Canfield, J. F. Bonnett, J. W. Stevenson, A. Shyam, and E. Lara-Curzio, "Compliant Alkali Silicate Sealing Glass for Solid Oxide Fuel Cell Applications: Thermal Cycle Stability and Chemical Compatibility," *Journal of Power Sources*, Vol. 196, pp. 2709-2716, 2011.

35. G. Kaur, O. P. Pandey, and K. Singh, "Chemical Interaction Study between Lanthanum Based Different Alkaline Earth Glass Sealants with Crofer 22 APU for Solid Oxide Fuel Cell Applications," *International Journal of Hydrogen Energy*, Vol. 37, pp. 3883-3889, 2012.

36. Y.-S. Chou, E. C. Thomsen, J.-P. Choi, and J. W. Stevenson, "Compliant Alkali Silicate Sealing Glass for Solid Oxide Fuel Cell Applications: The Effect of Protective YSZ Coating on Electrical Stability in Dual Environment," *Journal of Power Sources*, Vol. 202, pp. 149-156, 2012.

37. S. Celikn, "Influential Parameters and Performance of a Glass-Ceramic Sealant for Solid Oxide Fuel Cells," *Ceramics International*, Vol. 41, pp. 2744-2751, 2015.

38. B. Timurkutluka, Y. Ciflik, and H. Korkmaz, "Strength Evaluation of Glass-Ceramic Composites Containing Yttria Stabilized Zirconia after Thermal Cycling," *Ceramics International*, Vol. 41, pp. 6985-6990, 2015.

39. V. Kumar, G. Kaur, K. Lu, and G. Pickrell, "Interfacial Compatibility of Alumino-Borosilicate Glass Sealants with AISI 441 and YSZ for Different Atmospheres," *International Journal of Hydrogen Energy*, Vol. 40, pp. 1195-1202, 2015.

40. C.-K. Lin, T.-T. Chen, Y.-P. Chyou, and L.-K. Chiang, "Thermal Stress Analysis of a Planar SOFC Stack," *Journal of Power Sources*, Vol. 164, pp. 238-251, 2007.

41. A.-S. Chen, "Thermal Stress Analysis of a Planar SOFC Stack with Mica

Sealants," M.S. Thesis, National Central University, Jhong-Li, Taiwan, 2007.

42. C.-K. Lin, L.-H. Huang, L.-K. Chiang, and Y.-P. Chyou, "Thermal Stress Analysis of Planar Solid Oxide Fuel Cell Stacks: Effects of Sealing Design," *Journal of Power Sources*, Vol. 192, pp. 515-524, 2009.

43. L. Blum, S. M. Groß, J. Malzbender, U. Pabst, M. Peksen, R. Peters, and I. C. Vinke, "Investigation of Solid Oxide Fuel Cell Sealing Behavior under Stack Relevant Conditions at Forschungszentrum Jülich," *Journal of Power Sources*, Vol.196, pp. 7175-7181, 2011.

44. J.-Y. Chen, "Analysis of Mechanical Properties for the Joint of Metallic Interconnect and Glass Ceramic in Solid Oxide Fuel Cell," M.S. Thesis, National Central University, Jhong-Li, Taiwan, 2010.

45. Y.-A. Liu, "Environmental Effects on the Mechanical Properties of Joints in Solid Oxide Fuel Cell," M.S. Thesis, National Central University, Jhong-Li, Taiwan, 2014.

46. J.-H. Yeh, "Analysis of High-Temperature Mechanical Durability for the Joint of Glass Ceramic Sealant and Metallic Interconnect for Solid Oxide Fuel Cell," M.S. Thesis, National Central University, Jhong-Li, Taiwan, 2011.

47. D. W. Richerson, *Modern Ceramic Engineering*, 2nd Ed., Marcel Dekker, New York, USA, 1992.

48. N. E. Dowling, *Mechanical Behavior of Materials: Engineering Methods for Deformation, Fracture, and Fatigue*, 3rd Ed., Prentice Hall, New Jersey, USA, 2007.

49. J. Laurencin, G. Delette, F. Usseglio-Viretta, and S. D. Iorio, "Creep Behaviour of Porous SOFC Electrodes: Measurement and Application to Ni-8YSZ Cermets," *Journal of the European Ceramic Society*, Vol. 31, pp. 1741-1752, 2011.

50. C. Y. S. Chang, W. C. J. Wei, and C. H. Hsueh, "Viscosity of Ba-B-Si-Al-O Glass Measured by Indentation Creep Test at Operating Temperature of IT-SOFC," *Journal of Non-Crystalline Solids*, Vol. 357, pp. 1414-1419, 2011.

51. J. Milhans, D. S. Li, M. Khaleel, X. Sun, M. S. Al-Haik, A. Harris, and H. Garmestani, "Mechanical Properties of Solid Oxide Fuel Cell Glass-Ceramic Seal at High Temperatures," *Journal of Power Sources*, Vol. 196, pp. 5599-5603, 2011.

52. C.-K. Lin, K.-L. Lin, J.-H. Yeh, W.-H. Shiu, C.-K. Liu, and R.-Y. Lee,

"Aging Effects on High-Temperature Creep Properties of a Solid Oxide Fuel Cell Glass-Ceramic Sealant," *Journal of Power Sources*, Vol. 241, pp. 12-19, 2012.

53. J. Malzbender, Y. Zhao, and T. Beck, "Fracture and Creep of Glass-Ceramic Solid Oxide Fuel Cell Sealant Materials," *Journal of Power Sources*, Vol. 246, pp. 574-580, 2014.

54. J. Froitzheim, G. H. Meier, L. Niewolak, P. J. Ennis, H. Hattendorf, L. Singheiser, and W. J. Quadakkers, "Development of High Strength Ferritic Steel for Interconnect Application in SOFCs," *Journal of Power Sources*, Vol. 178, pp. 163-173, 2008.

55. B. Kuhn, C. A. Jimenez, L. Niewolak, T. Hüttel, T. Beck, H. Hattendorf, L. Singheiser, and W. J. Quadakkers, "Effect of Laves Phase Strengthening on the Mechanical Properties of High Cr Ferritic Steels for Solid Oxide Fuel Cell Interconnect Application," *Materials Science and Engineering A*, Vol. 528, pp. 5888-5899, 2011.

56. Y.-T. Chiu, C.-K. Lin, and J.-C. Wu, "High-Temperature Tensile and Creep Properties of a Ferritic Stainless Steel for Interconnect in Solid Oxide Fuel Cell," *Journal of Power Sources*, Vol. 196, pp. 2005-2012, 2011.

57. Y.-T. Chiu and C.-K. Lin, "Effects of Nb and W Additions on High-Temperature Creep Properties of Ferritic Stainless Steels for Solid Oxide Fuel Cell Interconnect," *Journal of Power Sources*, Vol. 198, pp. 149-157, 2012.

58. D. N. Boccaccini, H. L. Frandsen, B. R. Sudireddy, P. Blennow, Å. H. Persson, K. Kwok, and P. V. Hendriksen, "Creep Behaviour of Porous Metal Supports for Solid Oxide Fuel Cells," *International Journal of Hydrogen Energy*, Vol. 39, pp. 21569-21580, 2014.

59. B. Rutkowski, J. Malzbender, T. Beck, R. W. Steinbrech, and L. Singheiser, "Creep Behaviour of Tubular $Ba_{0.5}Sr_{0.5}Co_{0.8}Fe_{0.2}O_{3-\delta}$ Gas Separation Membranes," *Journal of the European Ceramic Society*, Vol. 31, pp. 493-499, 2011.

60. K.-L. Lin, "Analysis of Creep Properties of Glass Ceramic Sealant and Its Joint with Metallic Interconnect for Solid Oxide Fuel Cells," M.S. Thesis, National Central University, Jhong-Li, Taiwan, 2012.

61. Y.-T. Chiu, "Creep and Thermo-Mechanical Fatigue Properties of Ferritic Stainless Steels for Use in Solid Oxide Fuel Cell Interconnect," Ph.D. Thesis, National Central University , Jhong-Li, Taiwan, 2012.

62. C.-K. Liu, T-.Y. Yung, K.-F. Lin, R.-Y. Lee, and T.-S. Lee, Glass-Ceramic Sealant for Planar Solid Oxide Fuel Cells, United States Patent No. 7,897,530 B2, 2011.

63. M. Tomozawa, H. Li, and K. M. Davis, "Water Diffusion, Oxygen Vacancy Annihilation and Structural Relaxation in Silica Glasses," *Journal of Non-Crystalline Solids*, Vol. 179, pp. 162-169, 1994.

64. S. Fujita, A. Sakamoto, and M. Tomozawa, "Behavior of Water in Glass During Crystallization," *Journal of Non-Crystalline Solids*, Vol. 320, pp. 56-63, 2003.

65. T. Jin, M. O. Naylor, J. E. Shelby, and S. T. Misture, "Galliosilicate Glasses for Viscous Sealants in Solid Oxide Fuel Cell Stacks: Part III, Behavior in Air and Humidified Hydrogen," *International Journal of Hydrogen Energy*, Vol. 38, pp. 16308-16319, 2013.

66. W. Liu, X. Sun, and M. A. Khaleel, "Predicting Young's Modulus of Glass/Ceramic Sealant for Solid Oxide Fuel Cell Considering the Combined Effects of Aging, Micro-Voids and Self-Healing," *Journal of Power Sources*, Vol. 185, pp. 1193-1200, 2008.

67. G. Wei, J. Qu, Z. Yu, Y. Li, Q. Guo, and T. Qi, "Mineralizer Effects on the Synthesis of Amorphous Chromium Hydroxide and Chromium Oxide Green Pigment Using Hydrothermal Reduction Method," *Dyes and Pigments*, Vol. 113, pp. 487-495,2015.

TABLES

Table. 1 Chemical composition of Crofer 22 H alloy (in wt.%)

Fe	C	Cr	Mn	Si	Ti	Nb
Bal.	0.007	22.93	0.43	0.21	0.07	0.51
Cu	S	P	Al	W	La	
0.02	<0.002	0.014	0.02	1.94	0.08	

Table. 2 Average of mechanical properties for Crofer 22 H alloy [61]

Temperature (℃)	Yield strength (MPa)	Ultimate tensile strength (MPa)	Young's modulus (GPa)	Elongation (in 12 mm) (%)
25	406	567	205	27
600	286	359	181	29
650	241	295	161	30
700	204	219	142	39
750	140	147	88	54
800	120	123	86	55

Table. 3 Average biaxial flexural strength (σ_f) for variously aged GC-9 glass at different temperatures [46]

Average flexural strength	Aged condition	Temperature				
		25 ℃	650 ℃	700 ℃	750 ℃	800 ℃
σ_f (MPa)	Non-aged	38	50	47	33	18
	100 h-aged	38	49	53	54	32
	1000 h-aged	45	59	49	57	36

Table. 4 Creep fracture path of non-aged joint specimen

Type of Loading	Creep rupture time	Cracking path*
Shear	0-1	A → B → C → A
Shear	1-10	B → A → C
Shear	10-100	B → A → C
Shear	100-1000	D → A
Shear	> 1000	A + C
Tensile	0-1	A+C
Tensile	1-10	A+C
Tensile	10-100	C
Tensile	100-1000	A
Tensile	> 1000	A

*A: in glass-ceramic sealant layer; B: at the interface between $BaCrO_4$ layer and Cr_2O_3 layer; C: at the interface between glass-ceramic sealant layer and Cr_2O_3 layer; D: in Cr_2O_3 layer.

Table. 5 Creep fracture path of 1000 h-aged joint specimen

Type of Loading	Creep rupture time	Cracking path
Shear	0-1	A
Shear	1-10	A
Shear	10-100	A
Tensile	0-1	A
Tensile	1-10	A
Tensile	10-100	A

FIGURES

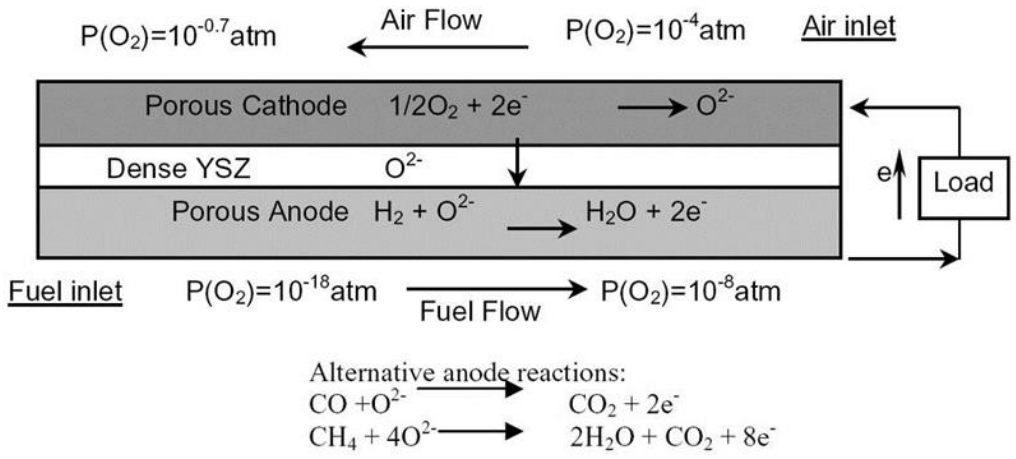

Fig. 1 Operating principle of a single SOFC unit using hydrogen as fuel. [4]

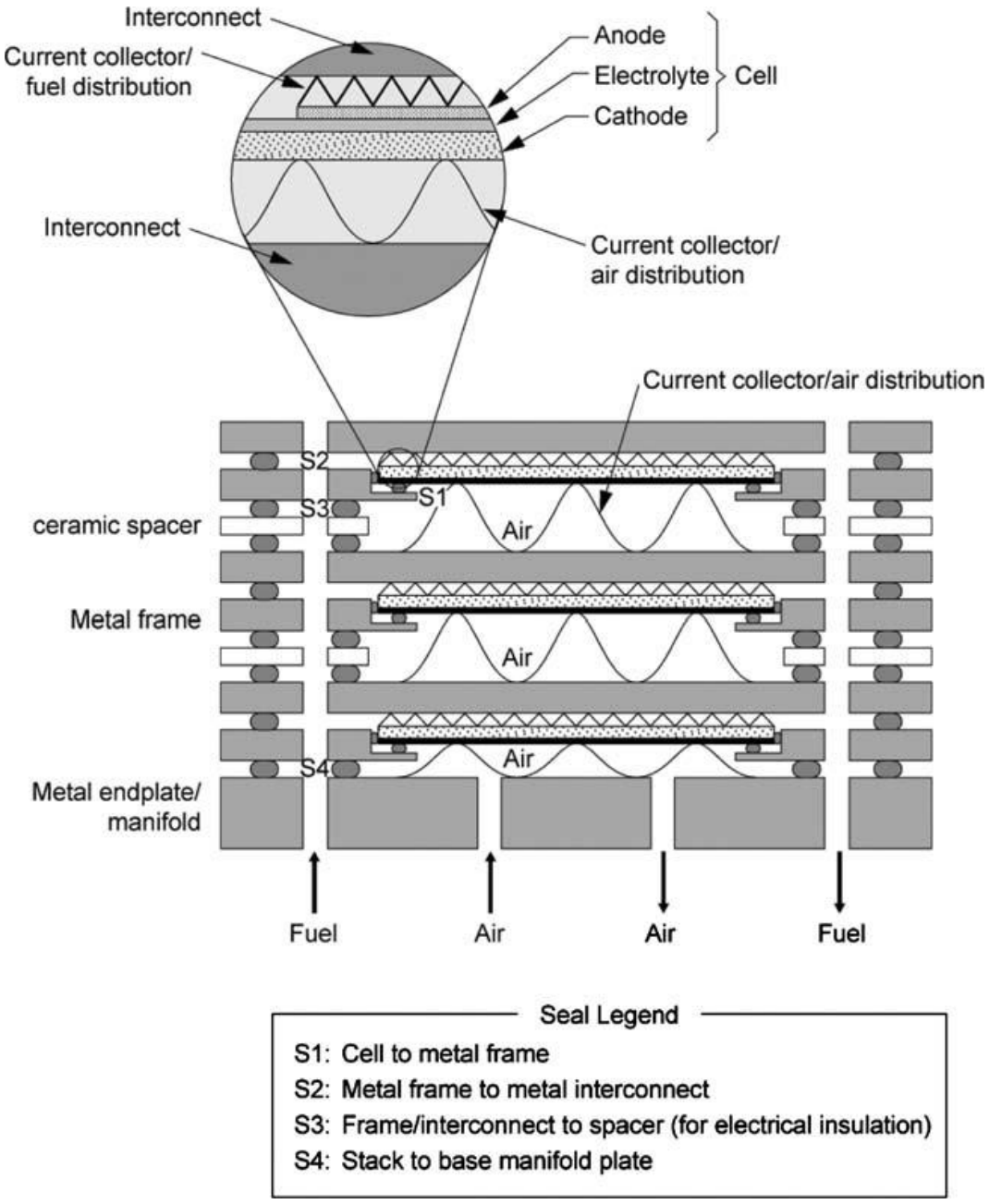

Fig. 2 Structural scheme of a planar SOFC stack. [4]

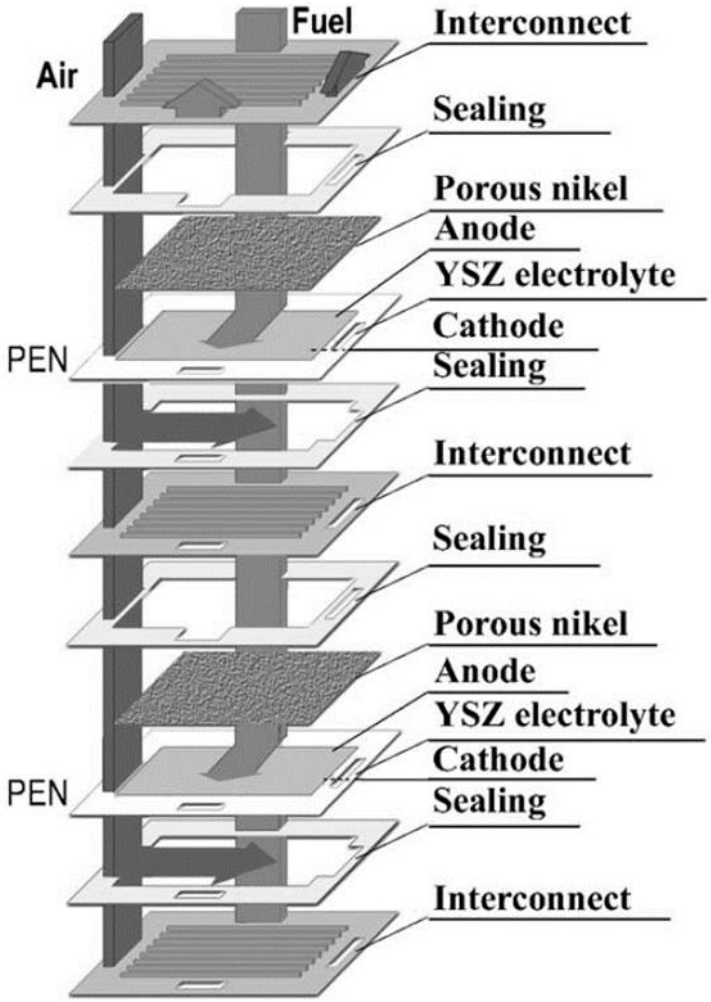

Fig. 3 Scheme of seals used in a planar SOFC stack with metallic interconnects and metallic internal gas manifold channels. [8]

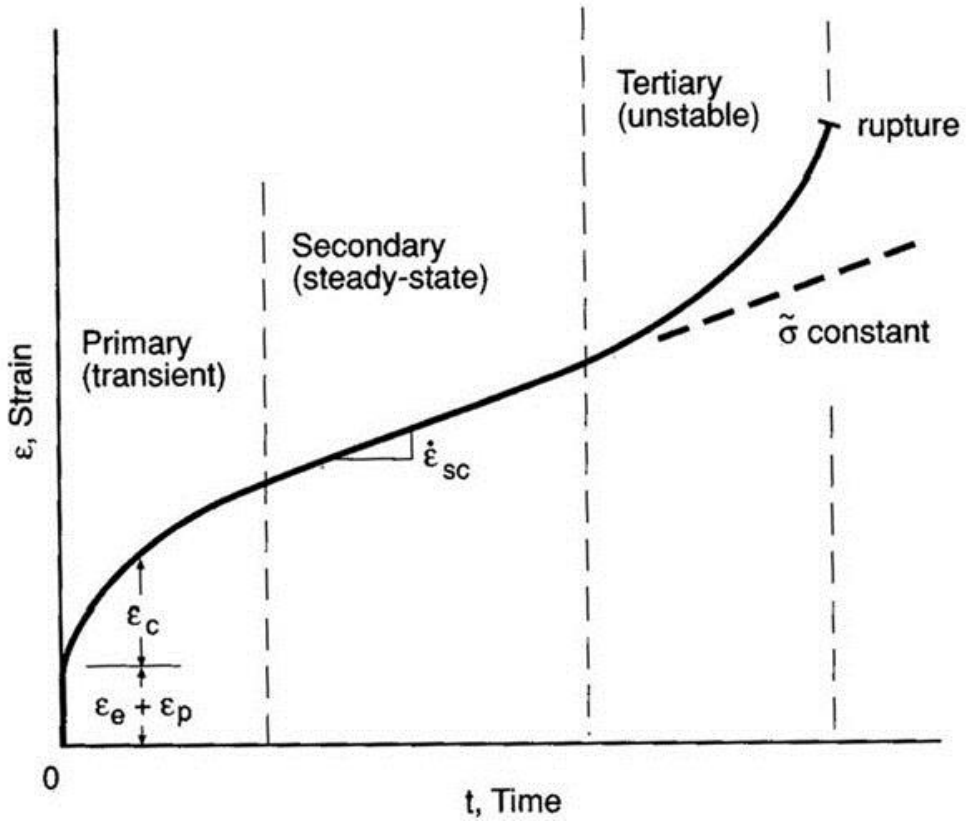

Fig. 4 A typical strain-time relationship during creep under constant load. [48]

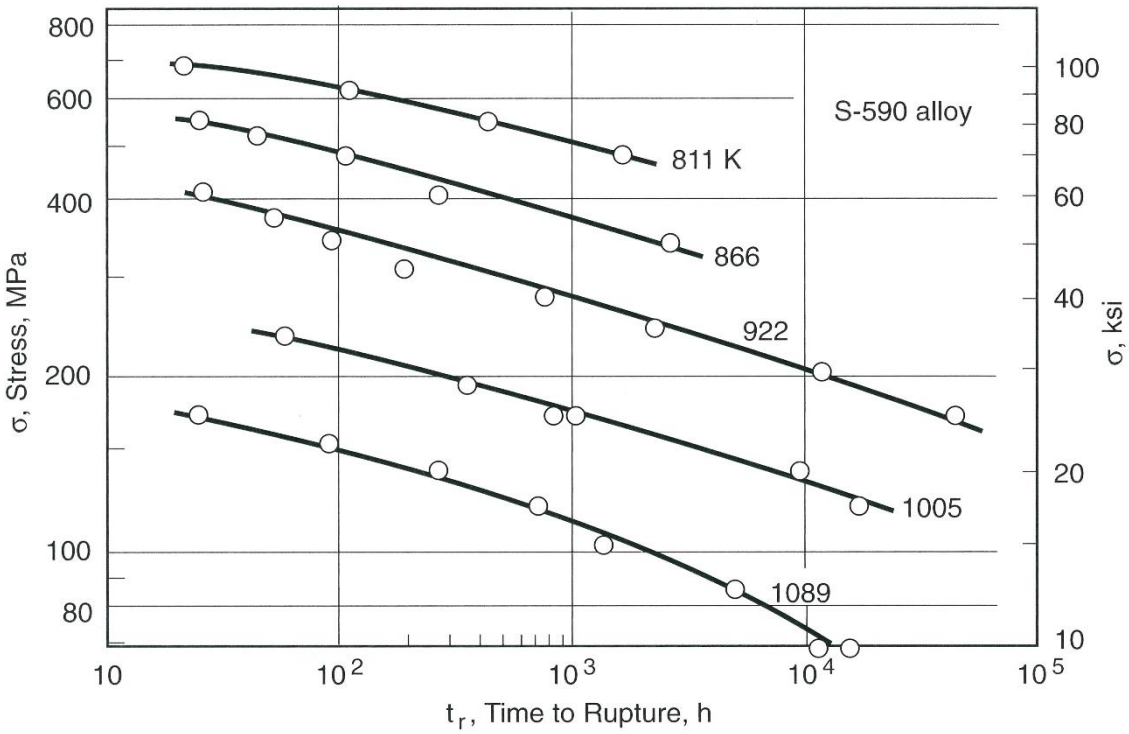

Fig. 5 Stress versus rupture life curves for S-590, an iron-based and heat-resisting alloy. [48]

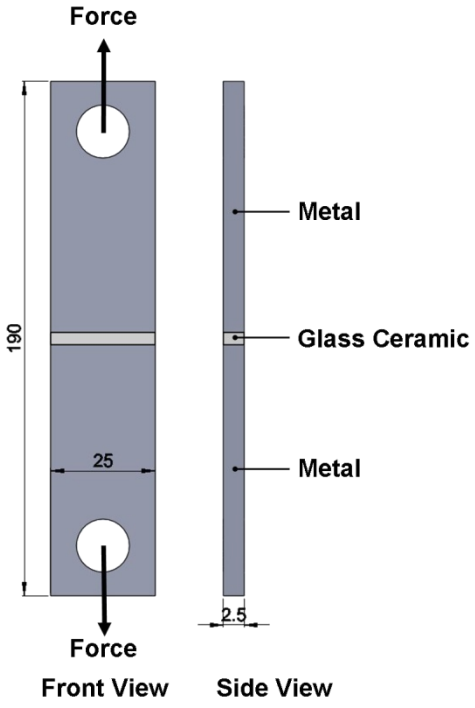

(a)

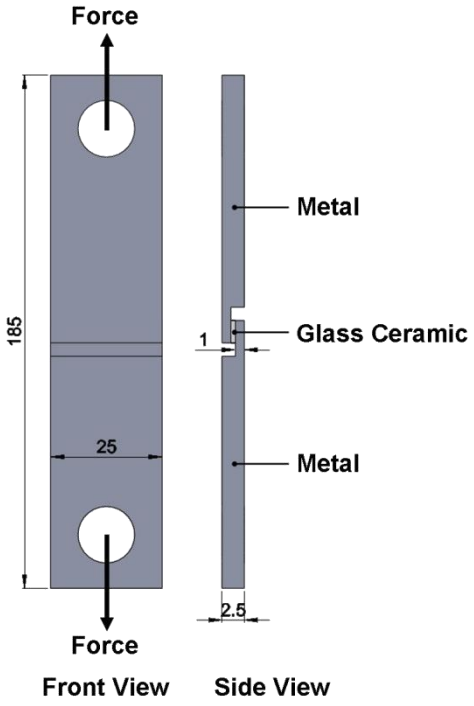

(b)

Fig. 6 Scheme of two types of joint specimens: (a) tensile specimen; (b) shear specimen. (Dimensions: mm)

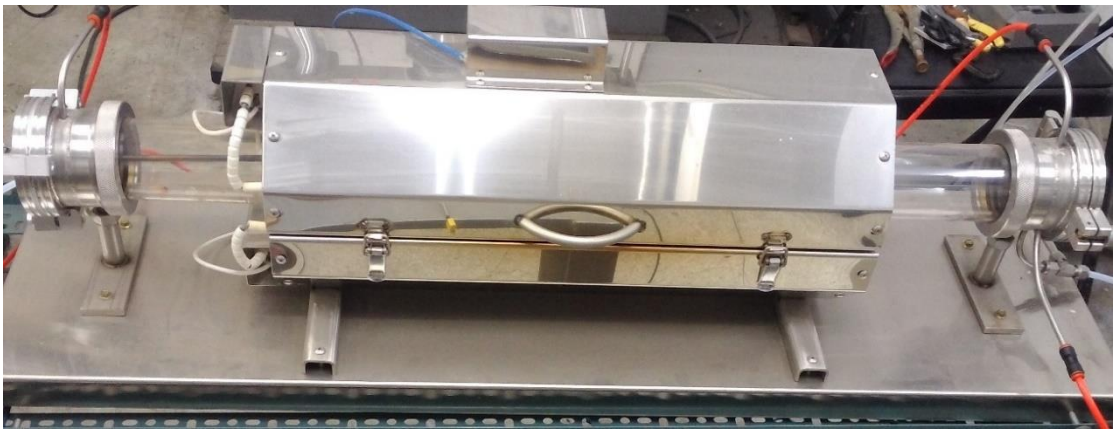

Fig. 7 Photograph of the environmental furnace for aging treatment.

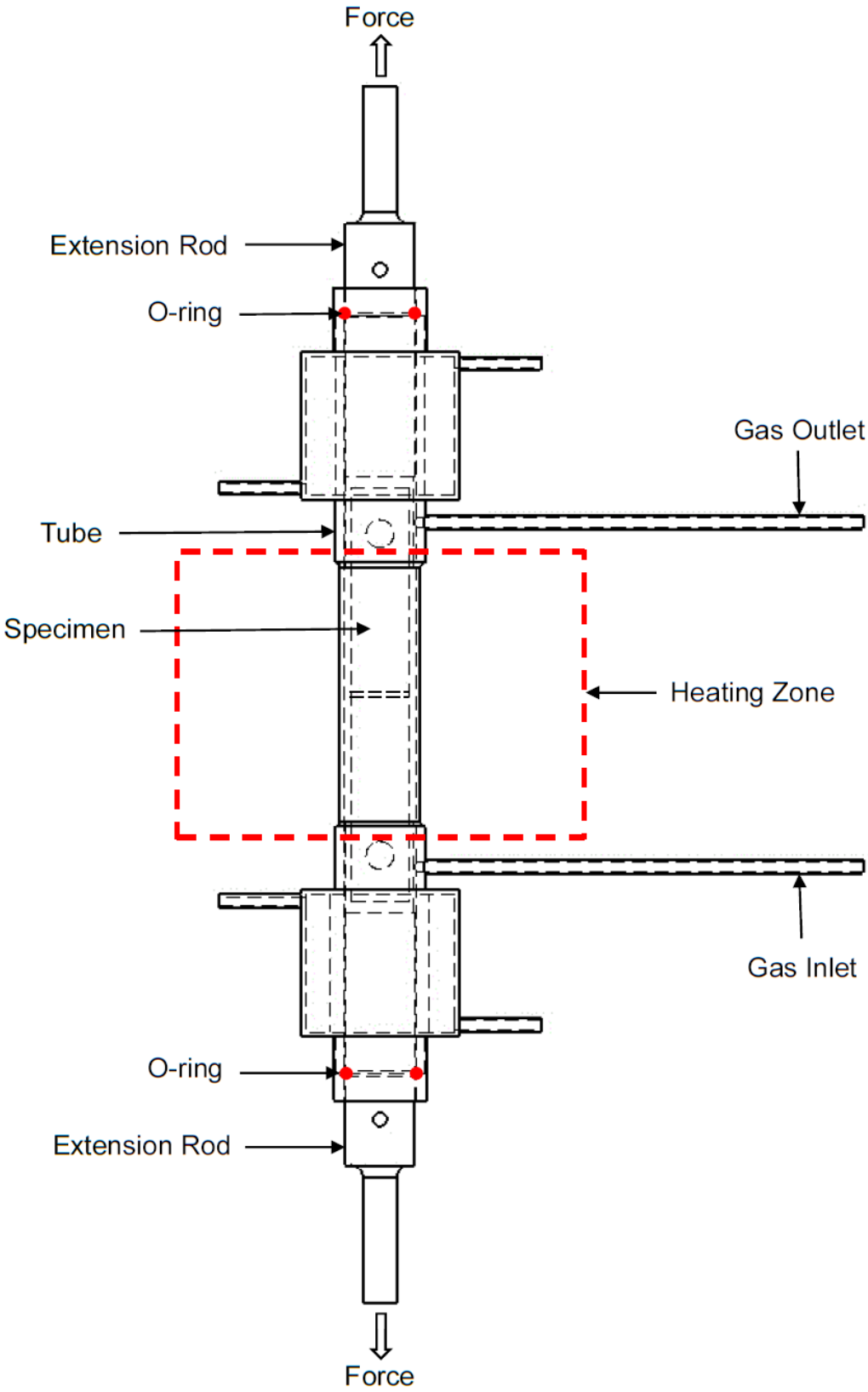

Fig. 8 Schematic of specimen enclosed by a gas-tight tube in mechanical test.

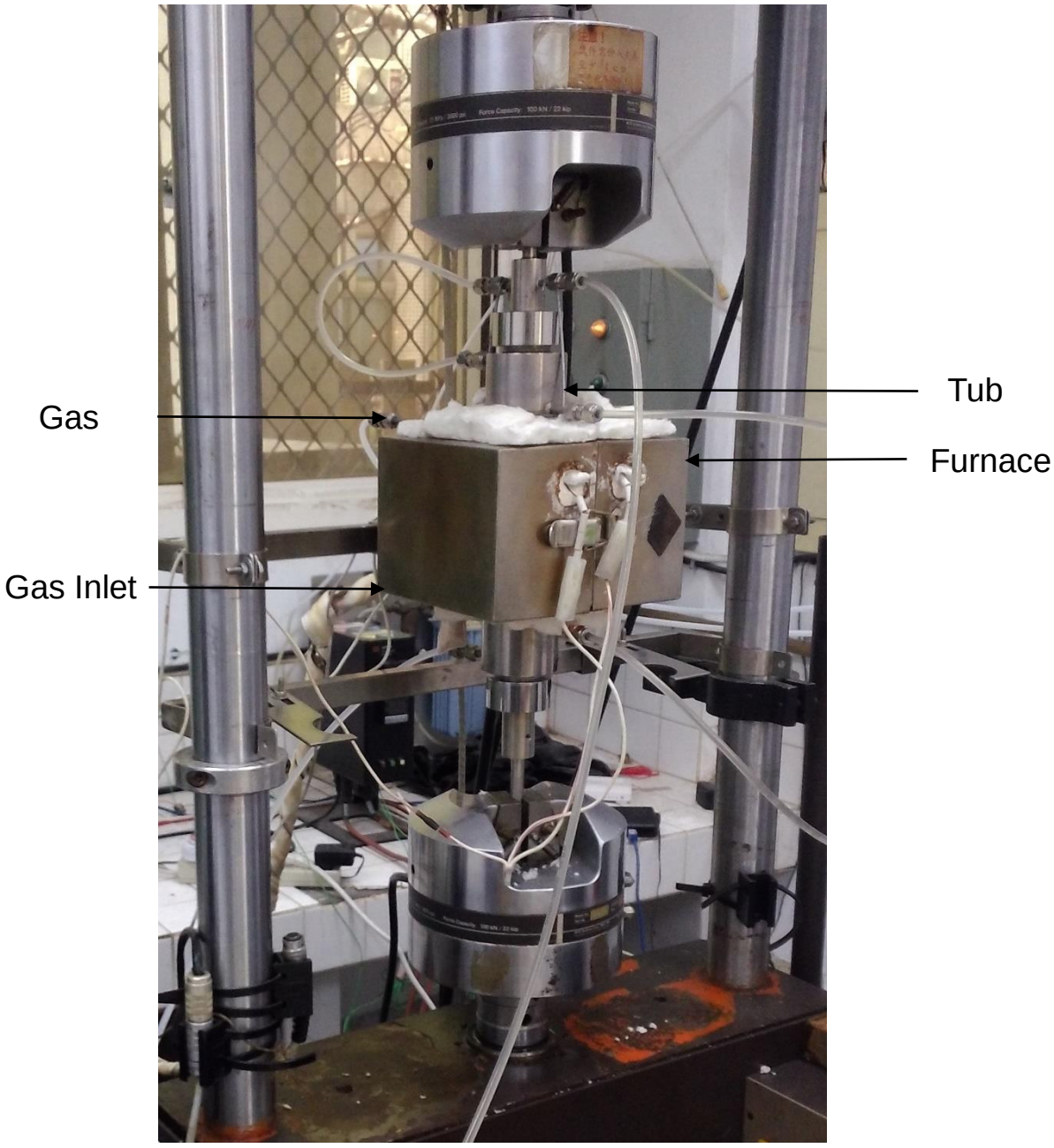

Fig. 9 Photograph of experimental setup for short-term creep test.

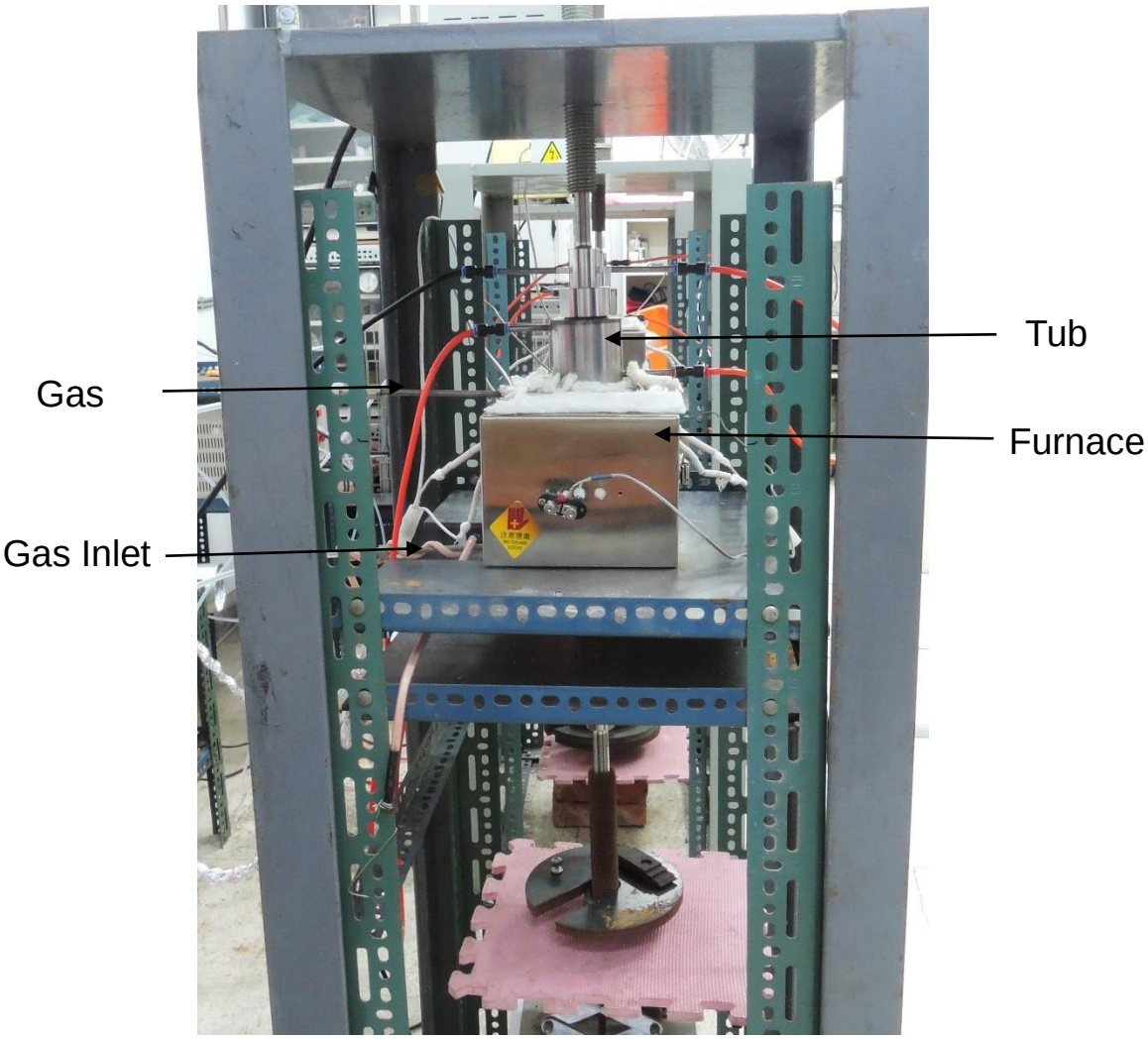

Fig. 10 Photograph of experimental setup for long-term creep test.

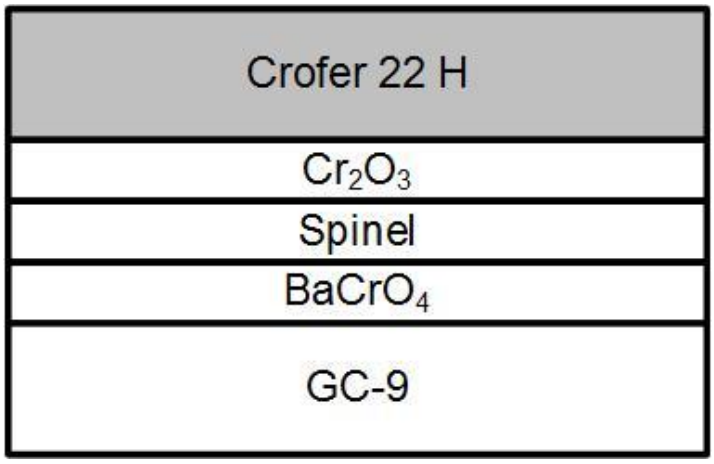

Fig. 11 Schematic of oxide layers between Crofer 22 H and GC-9 glass-ceramic.

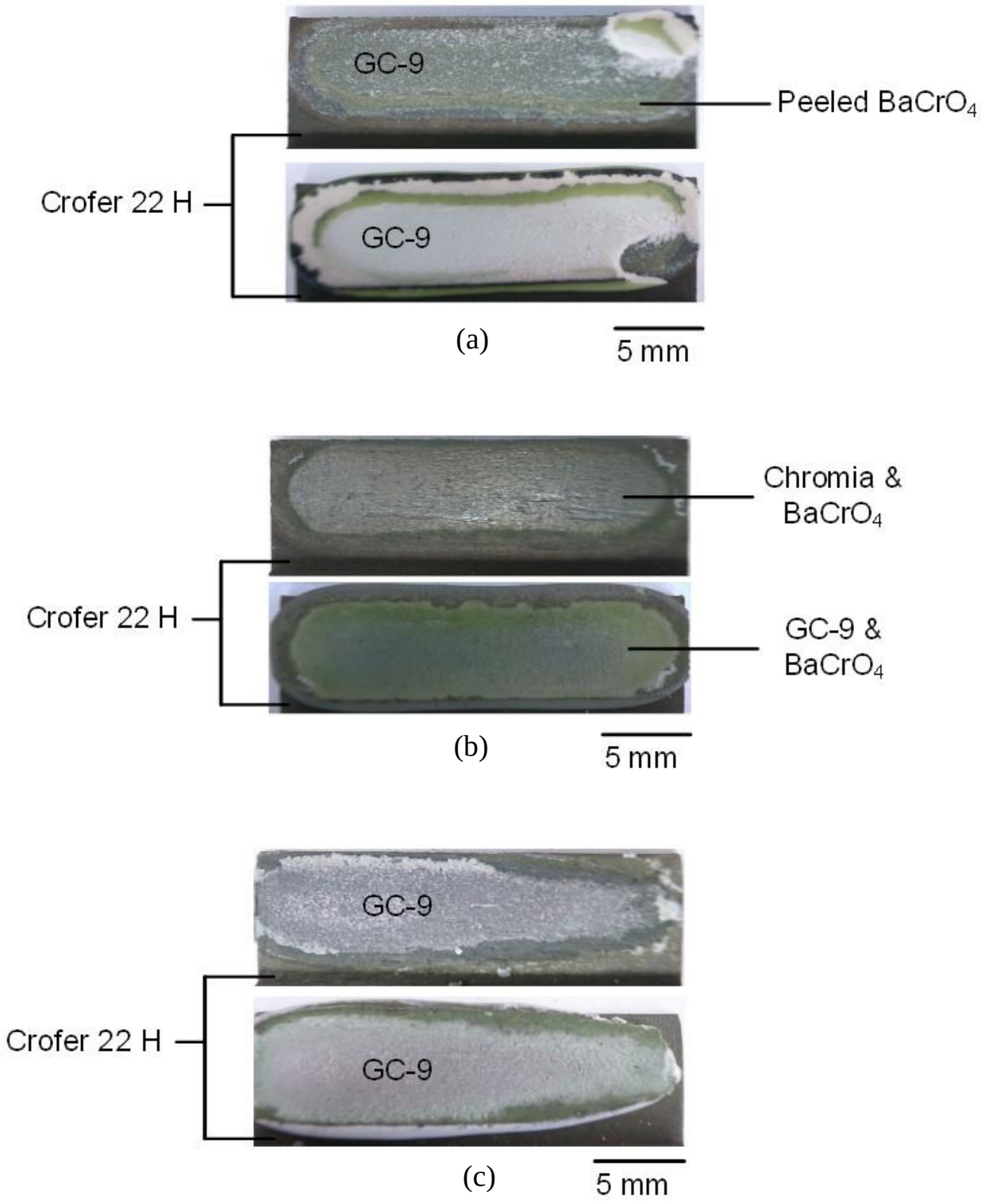

Fig. 12 Failure patterns of non-aged shear specimens tested in H_2-7 vol% H_2O at 800 ℃: (a) non-aged; (b) 100 h-aged; (b) 1000 h-aged. [45]

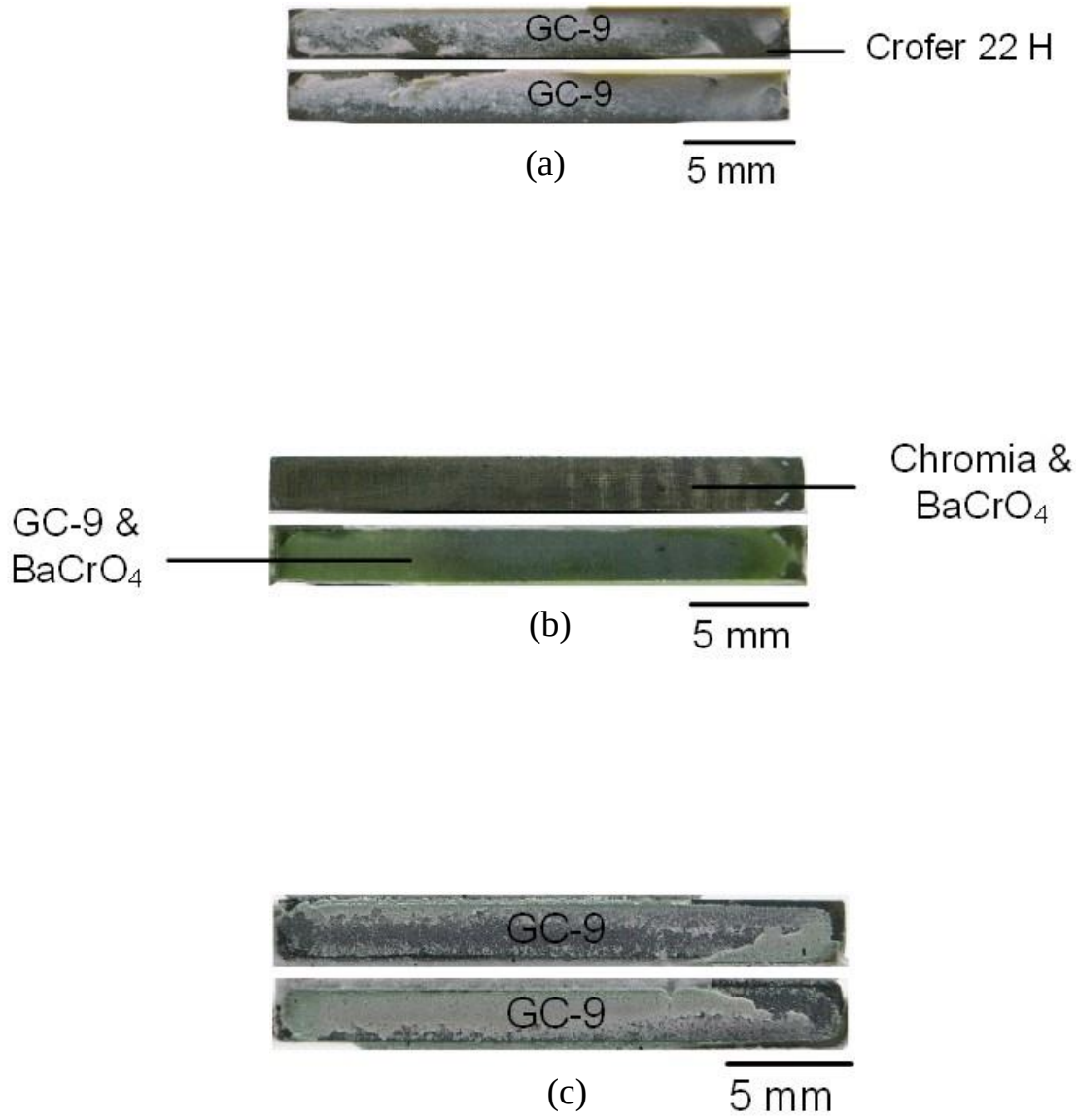

Fig. 13 Failure patterns of non-aged tensile specimens tested in H_2-7 vol% H_2O at 800 ℃: (a) non-aged; (b) 100 h-aged; (b) 1000 h-aged. [45]

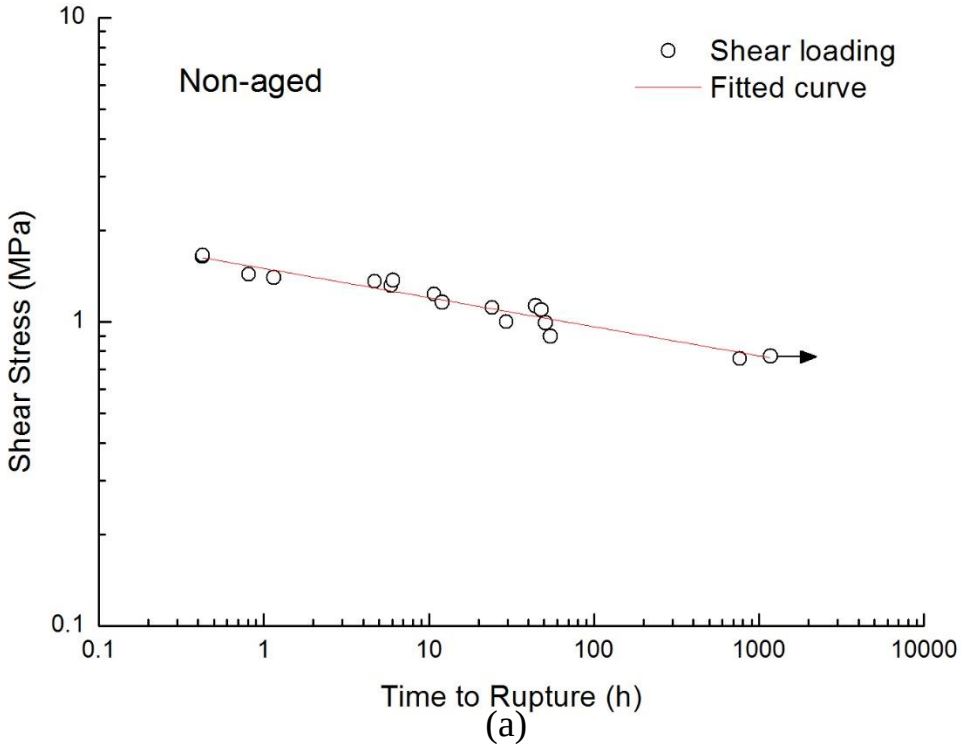

(a)

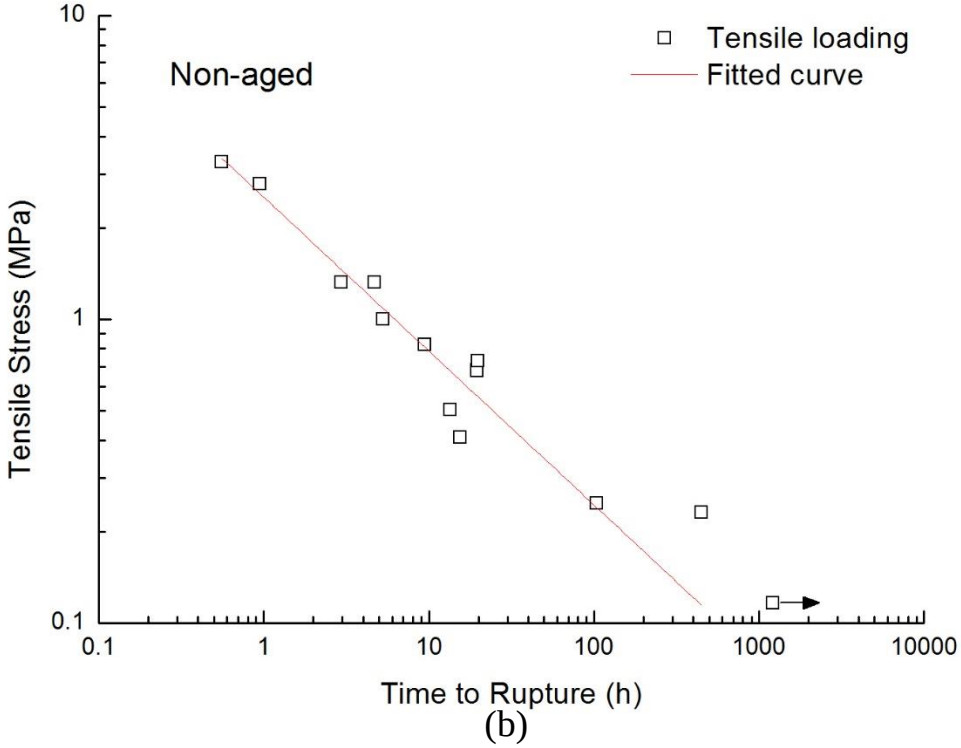

(b)

Fig. 14 Applied stress versus rupture time for non-aged joint specimens subjected to constant (a) shear and (b) tensile loading. (Arrow indicates the specimen was not ruptured when the test was terminated.)

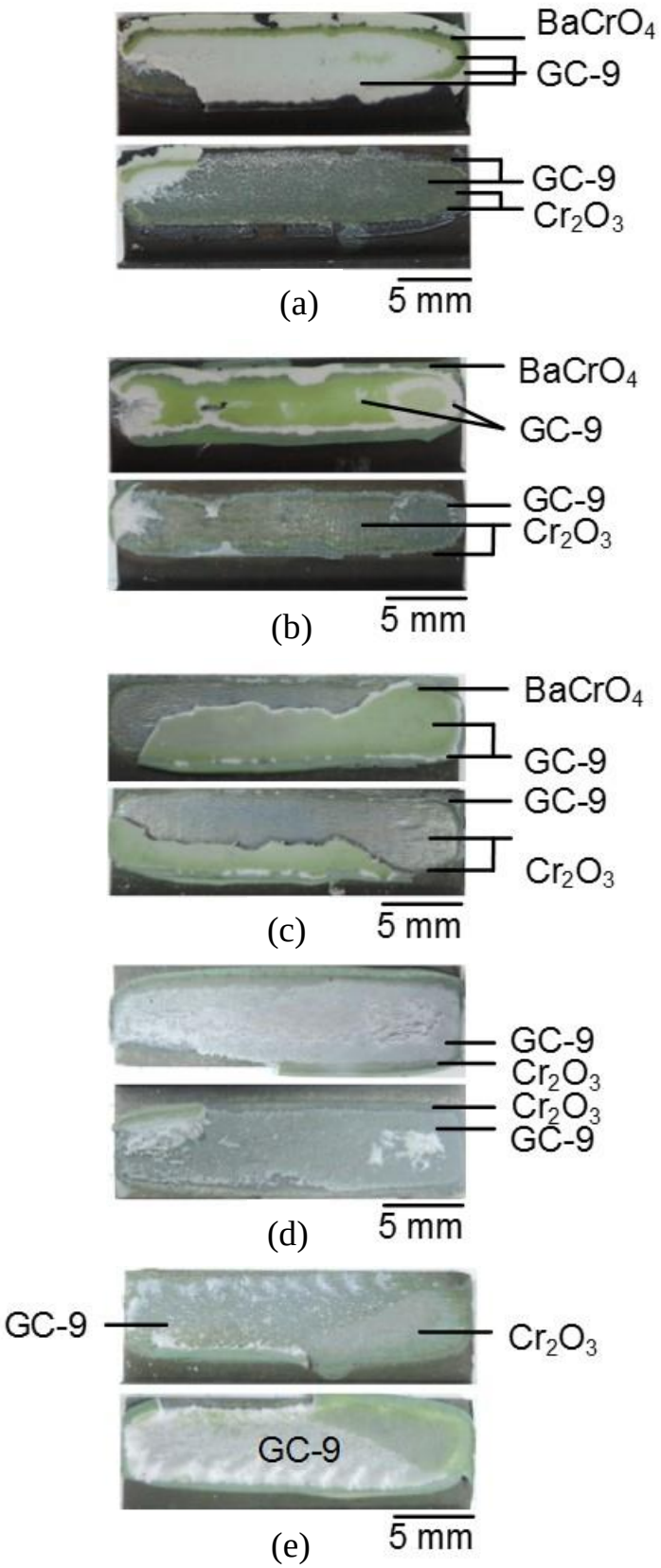

Fig. 15 Failure patterns in the non-aged shear specimens tested at 800 ℃ with various creep rupture times: (a) 0-1 h; (b) 1-10 h; (c) 10-100 h; (d) 100-1000 h; (e) over 1000 h.

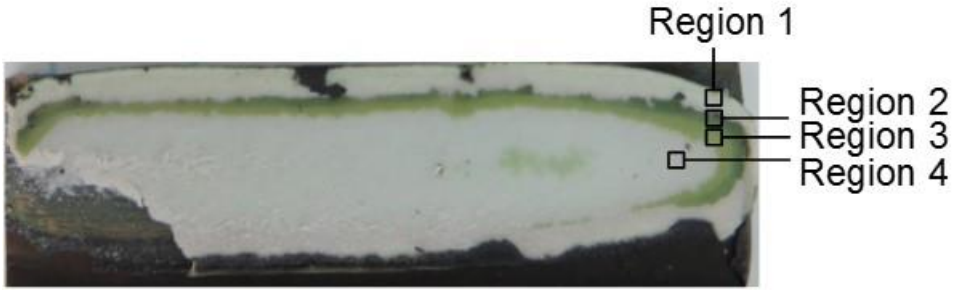

(a)

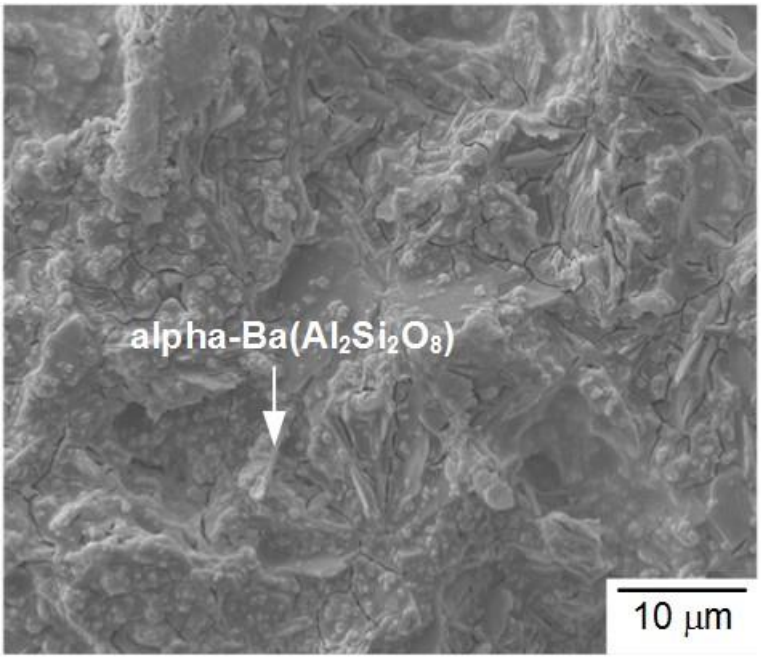

(b)

Fig. 16 Fracture surface of the non-aged shear specimen shown in the upper part of Fig. 15(a): (a) optical micrograph showing the observed regions of SEM; (b) SEM micrograph of Region 1 (glass-ceramic sealant); (c) SEM micrograph of Region 2 ($BaCrO_4$ chromate); (d) SEM micrograph of Region 3 (glass-ceramic sealant); (e) SEM micrograph of Region 4 (glass-ceramic sealant).

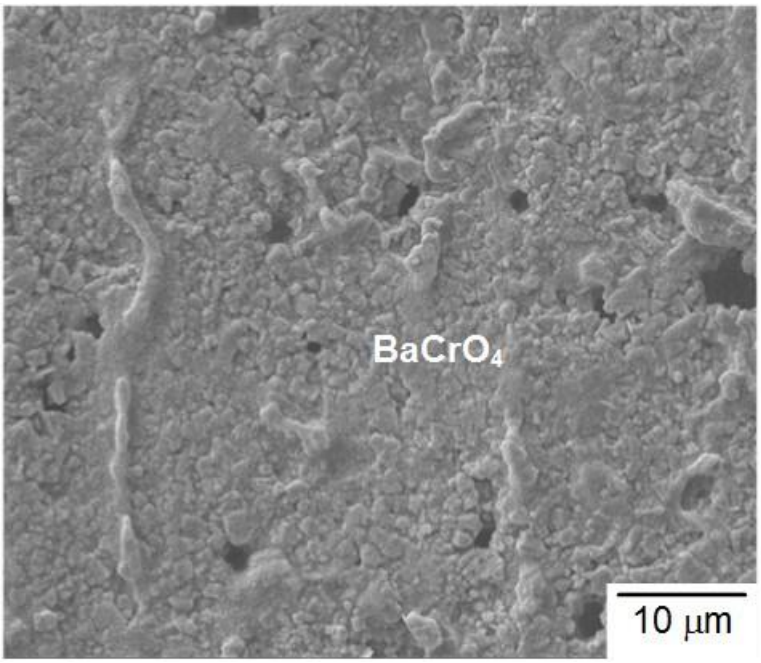

(c)

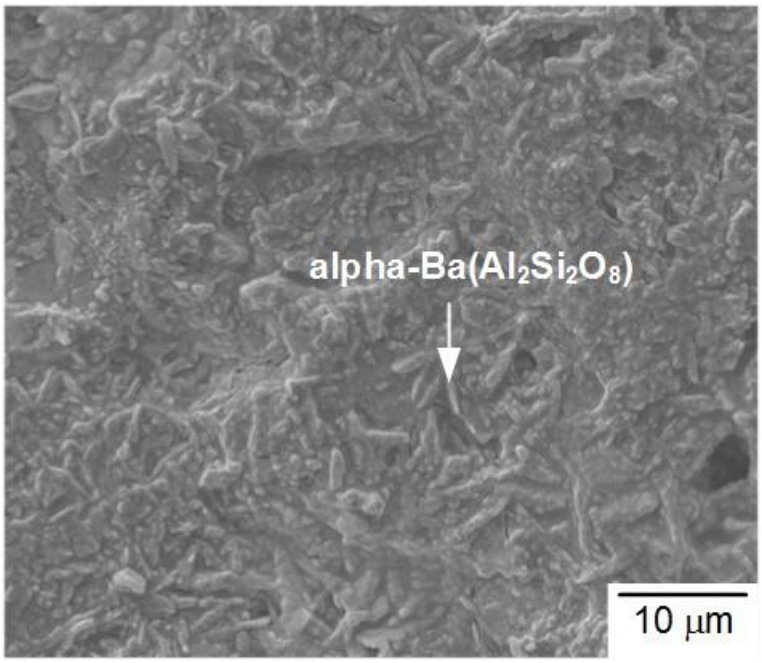

(d)

Fig. 16 (continued)

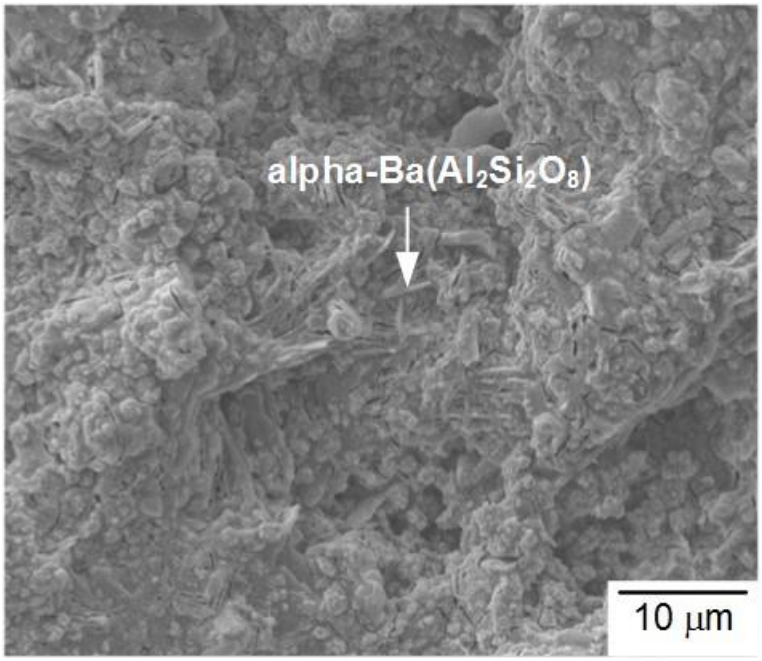

(e)

Fig. 16 (continued)

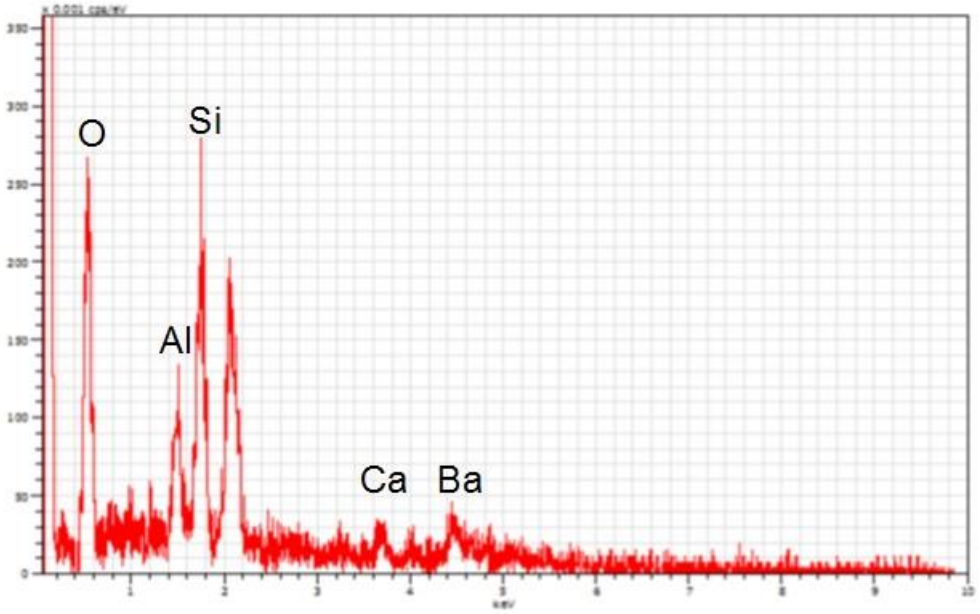

(a)

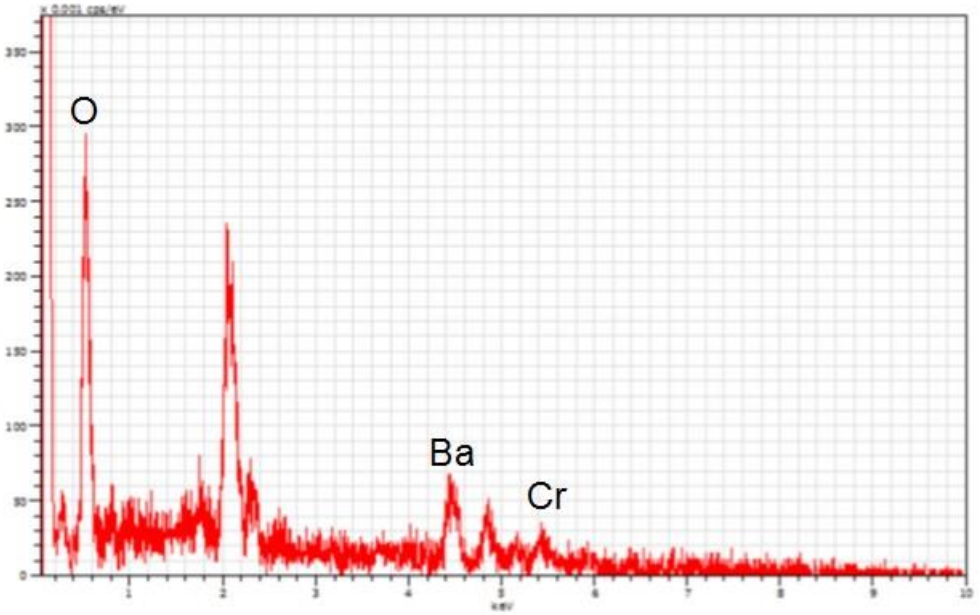

(b)

Fig. 17 EDS analysis results of the fracture surface of a non-aged shear joint specimen: (a) glass-ceramic layer (in Fig. 16(b)); (b) $BaCrO_4$ chromate layer (in Fig. 16 (c)); (c) glass-ceramic layer (in Fig. 16 (d)).

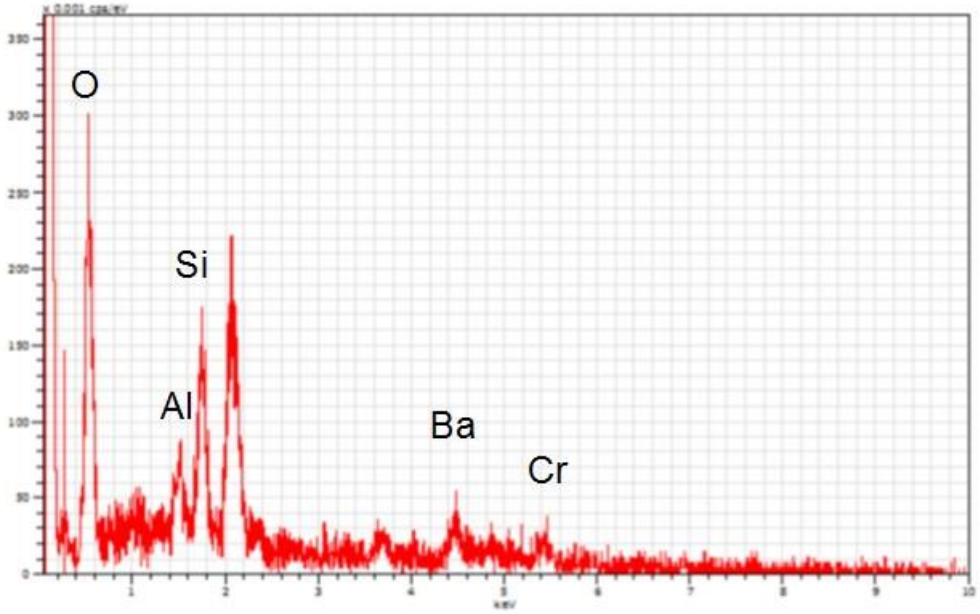

(c)

Fig. 17 (continued)

(a)

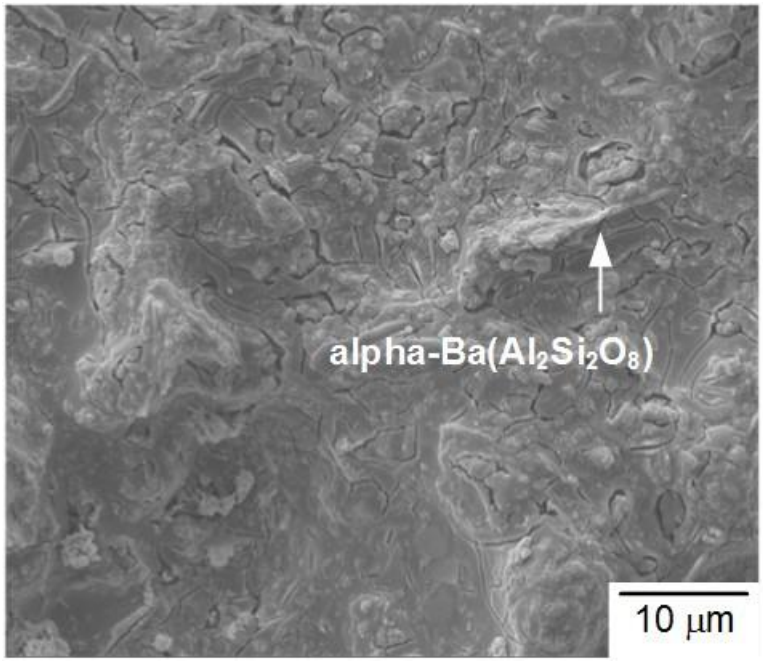

(b)

Fig. 18 Fracture surface of the non-aged shear specimen shown in the lower part of Fig. 15(a): (a) optical micrograph showing the observed regions of SEM; (b) SEM micrograph of Region 1 (glass-ceramic sealant); (c) SEM micrograph of Region 2 (Cr_2O_3 chromia); (d) SEM micrograph of Region 3 (Cr_2O_3 chromia); (e) SEM micrograph of Region 4 (glass-ceramic sealant).

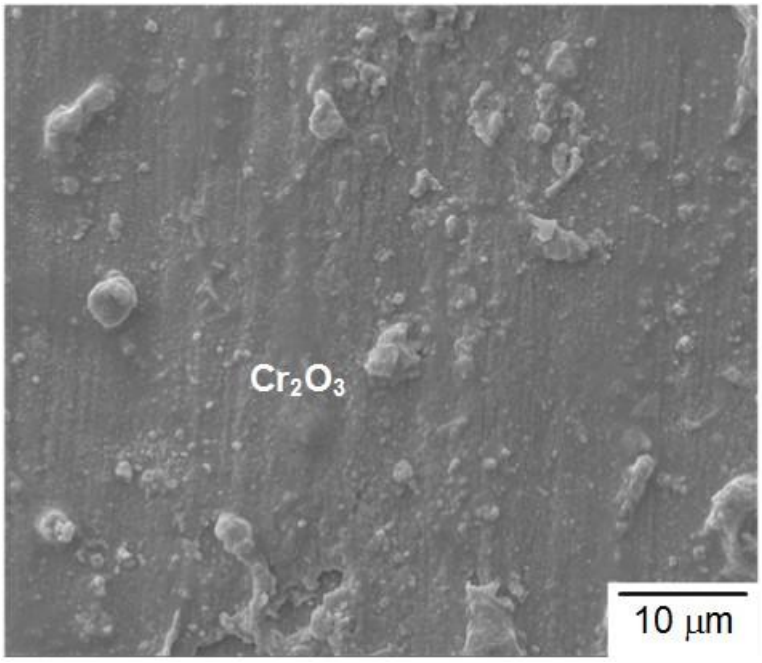

(c)

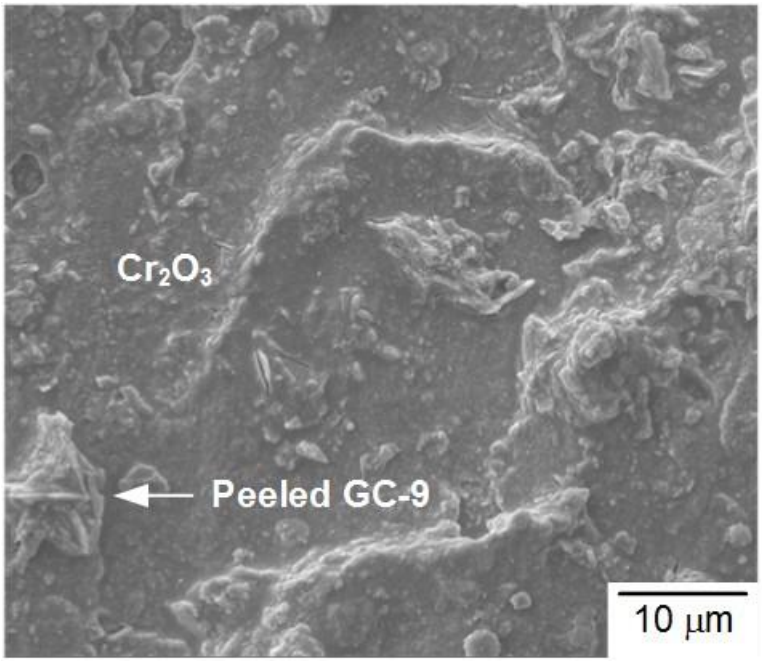

(d)

Fig. 18 (continued)

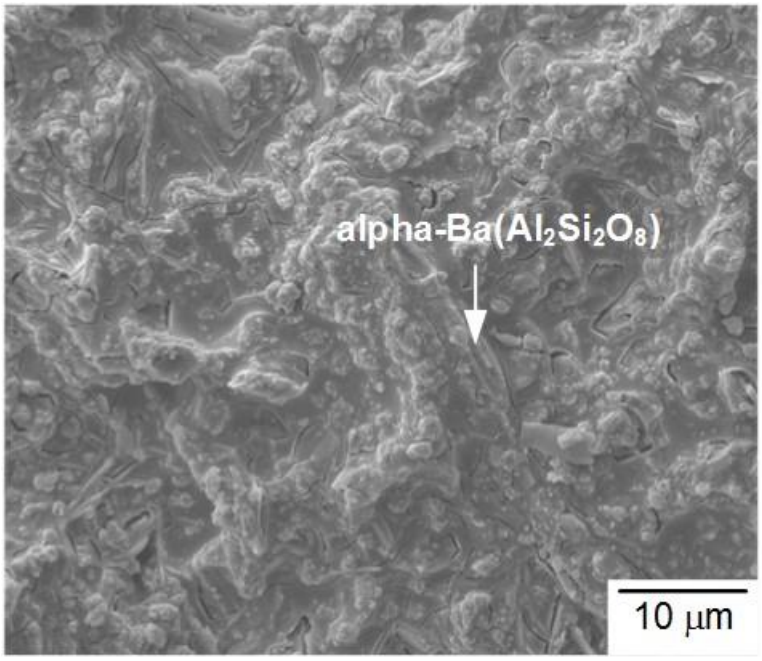

(e)

Fig. 18 (continued)

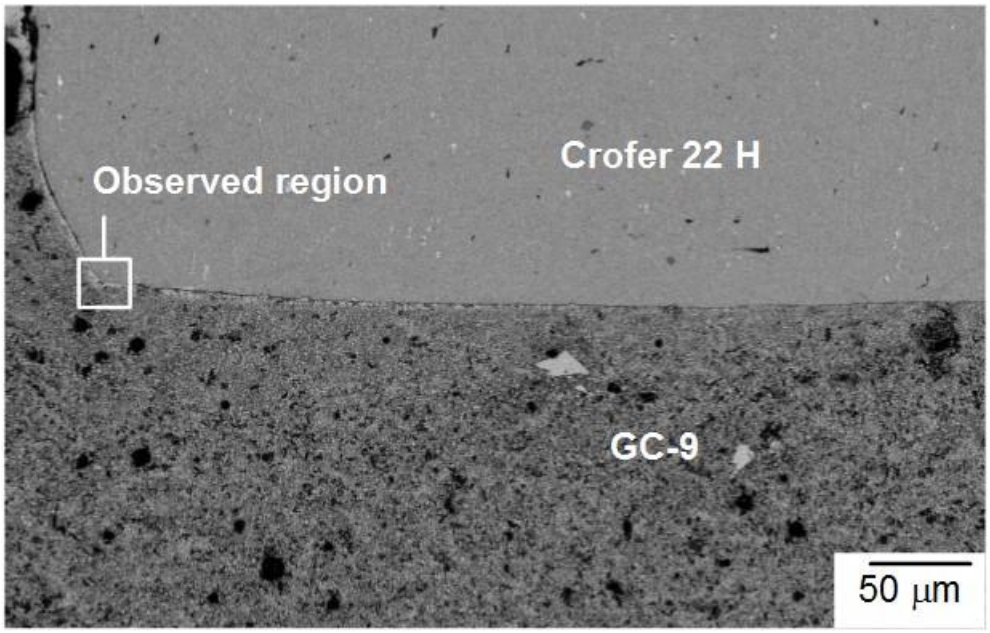

(a)

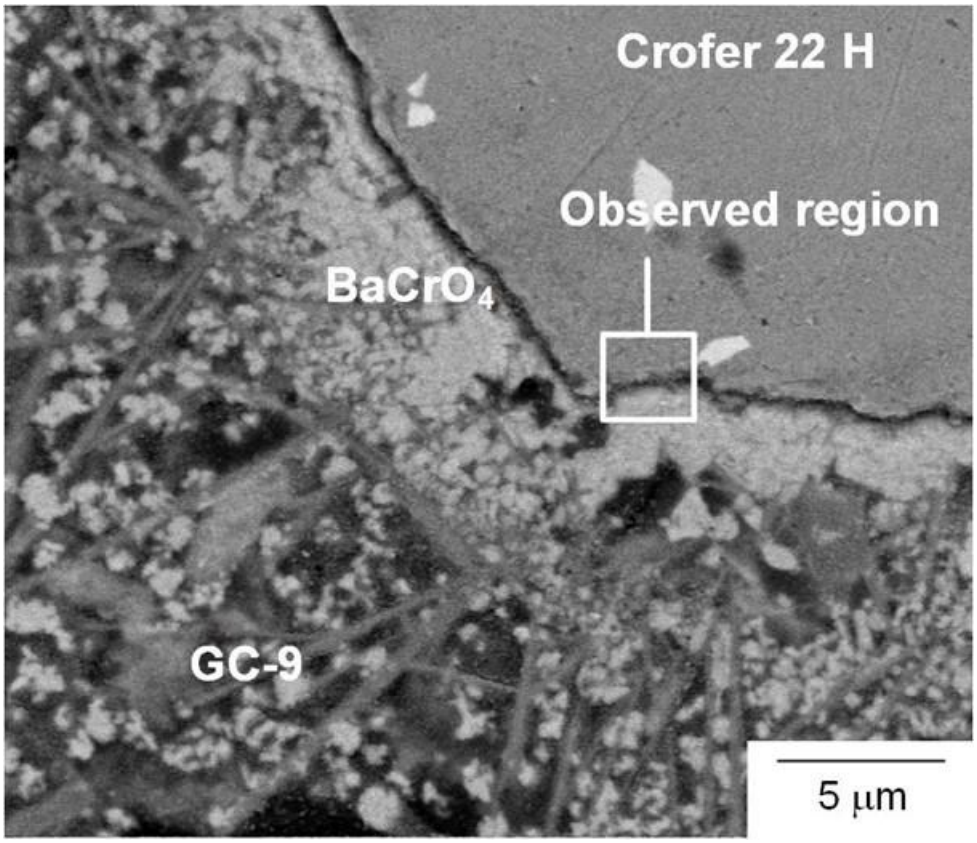

(b)

Fig. 19 Cross-sectional SEM micrographs (BSE mode) of an interface between the GC-9 and Crofer 22 H in a non-aged specimen: (a) low magnification view; (b) high magnification of the outlined region in (a); (c) higher magnification of the outlined region in (b).[45]

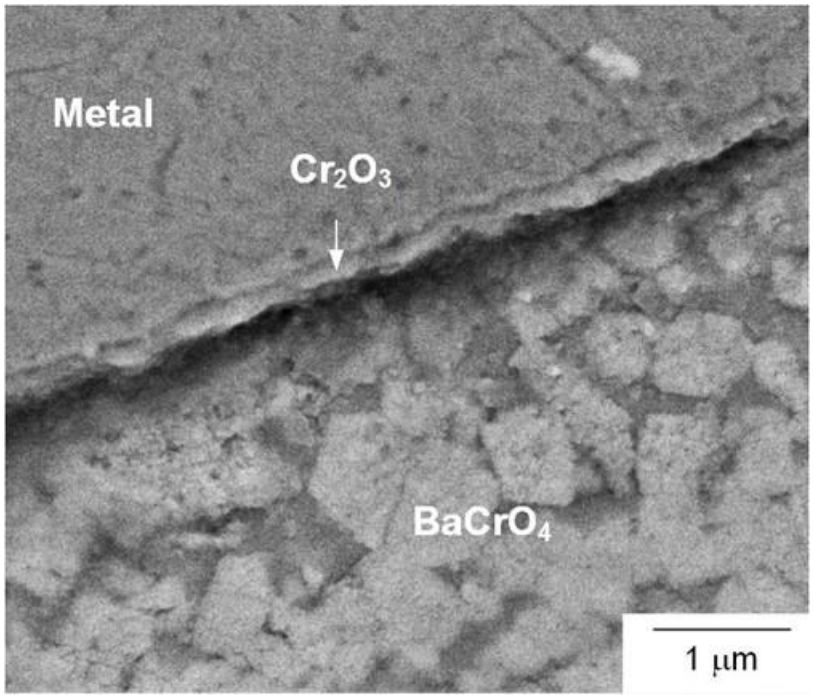

(c)

Fig. 19 (continued)

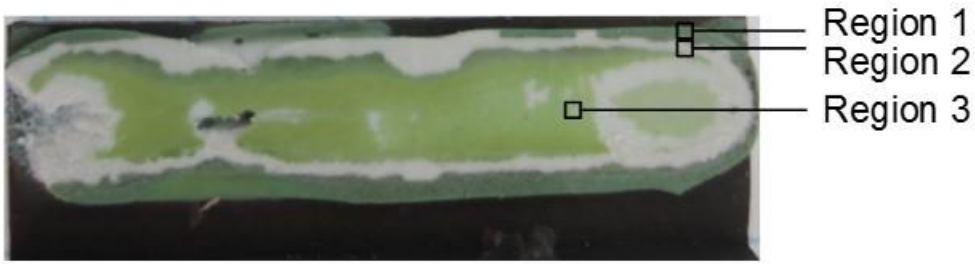

(a)

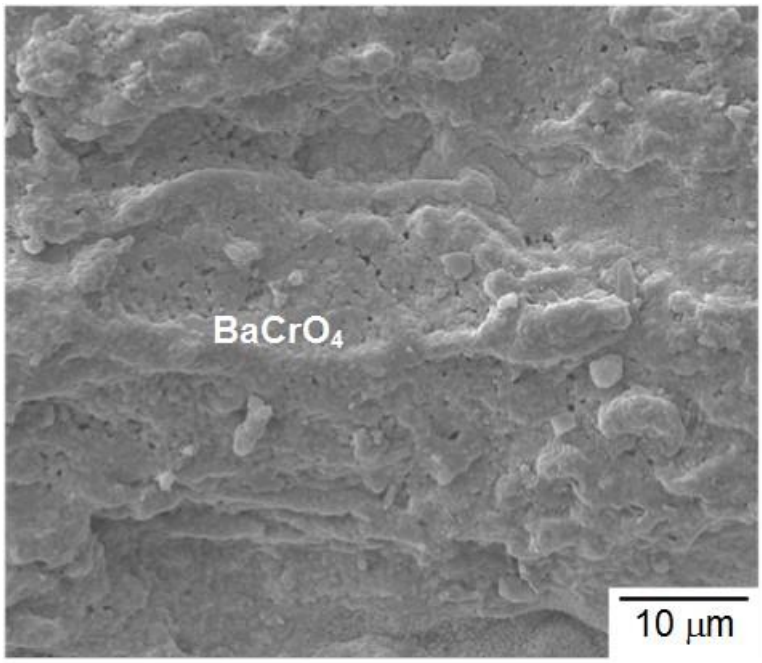

(b)

Fig. 20 Fracture surface of the non-aged shear specimen shown in the upper part of Fig. 15(b): (a) optical micrograph showing the observed regions of SEM; (b) SEM micrograph of Region 1 ($BaCrO_4$ chromate); (c) SEM micrograph of Region 2 (glass-ceramic sealant); (d) SEM micrograph of Region 3 (glass-ceramic sealant).

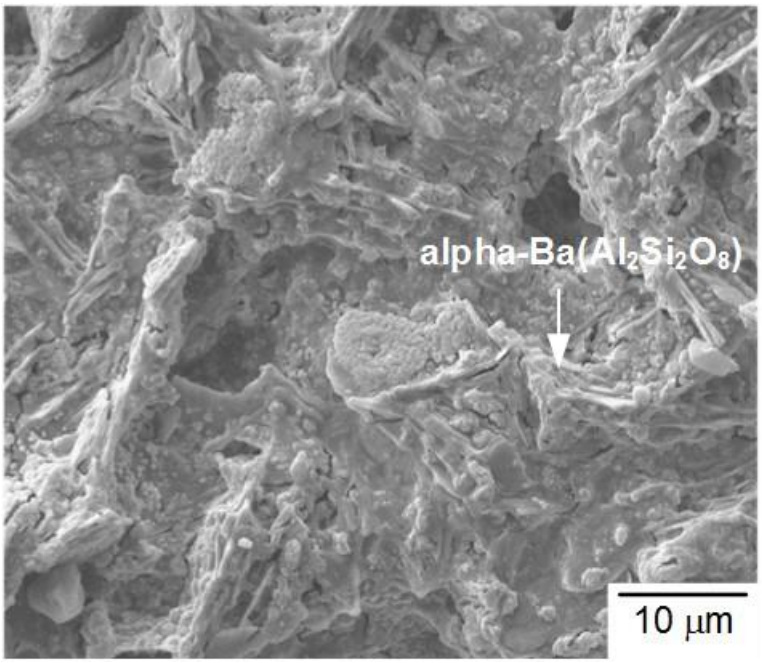

(c)

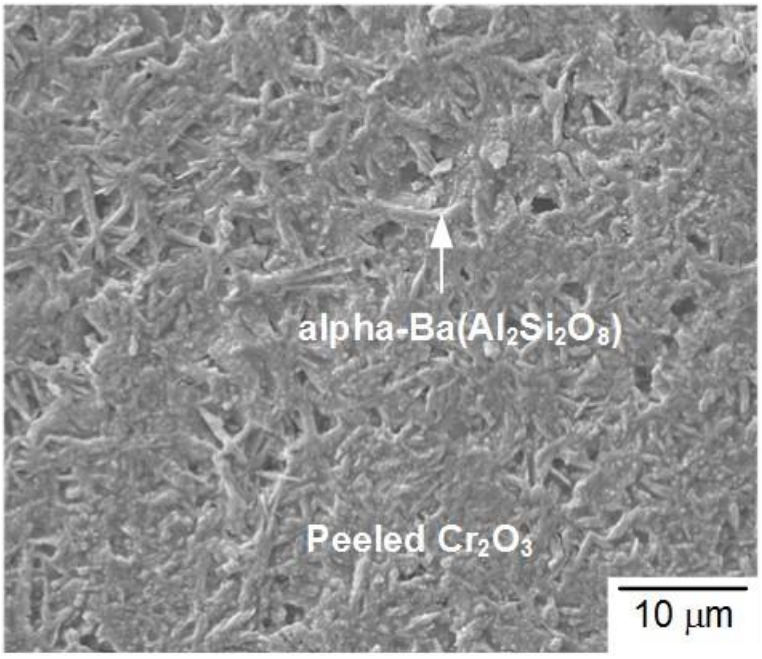

(d)

Fig. 20 (continued)

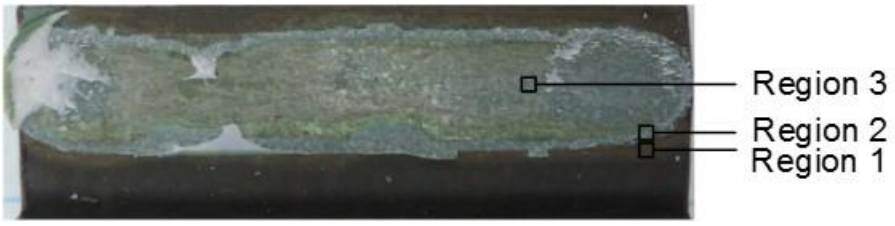

(a)

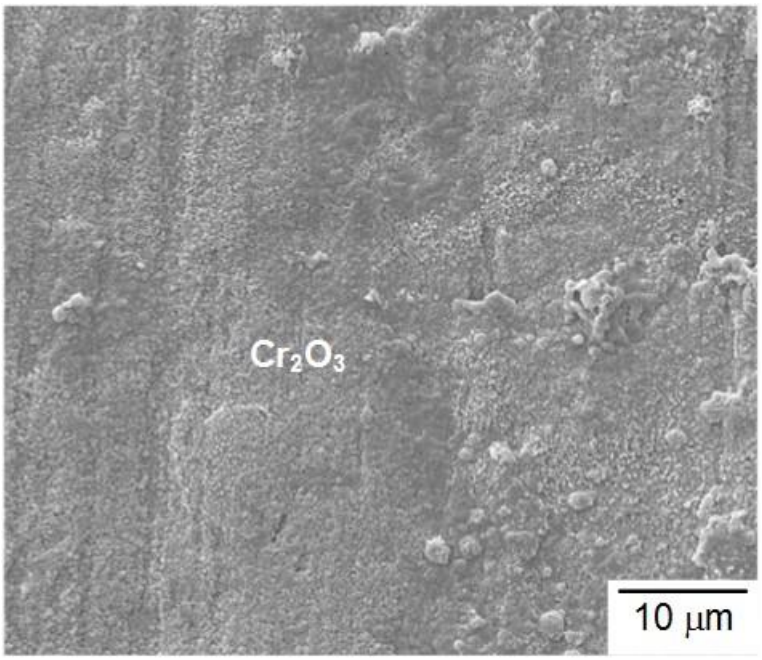

(b)

Fig. 21 Fracture surface of the non-aged shear specimen shown in the lower part of Fig. 15(b): (a) optical micrograph showing the observed regions of SEM; (b) SEM micrograph of Region 1 (Cr_2O_3 chromia); (c) SEM micrograph of Region 2 (glass-ceramic sealant); (d) SEM micrograph of Region 3 (Cr_2O_3 chromia).

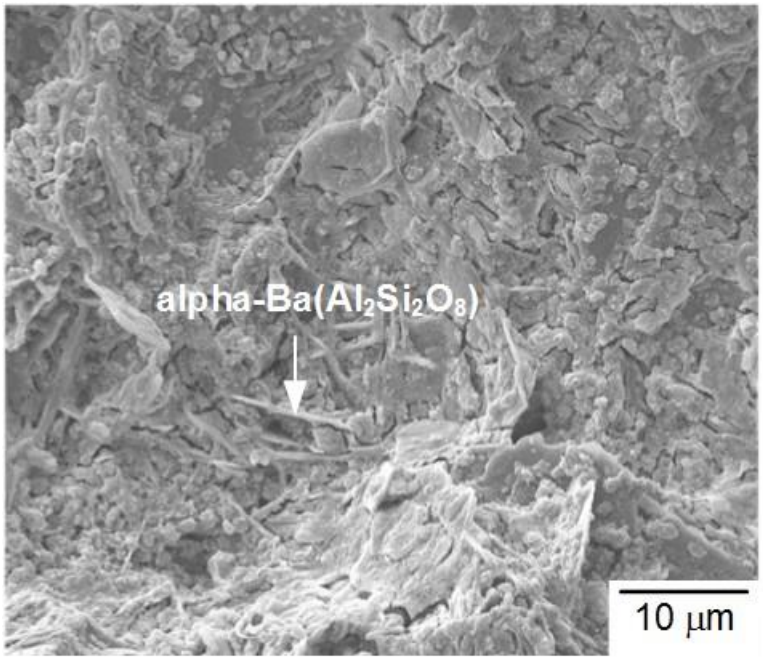

(c)

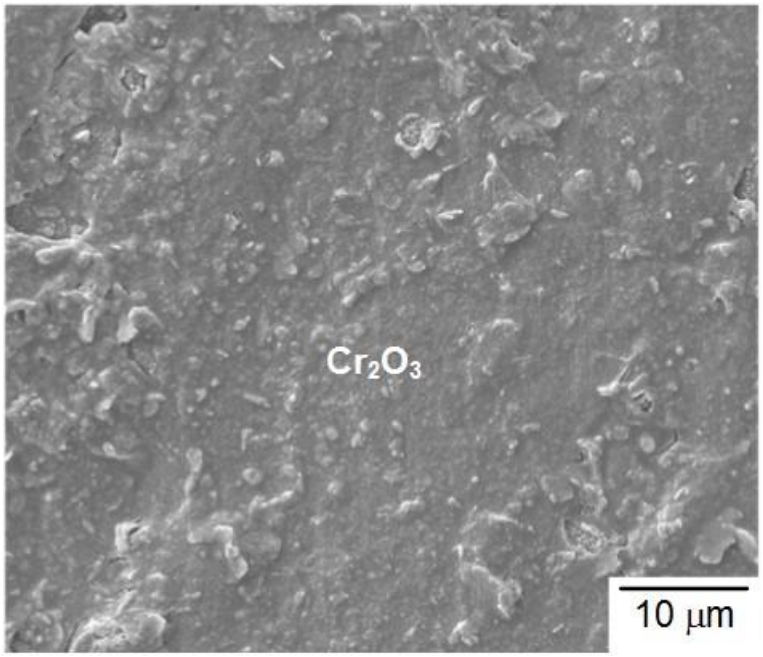

(d)

Fig. 21 (continued)

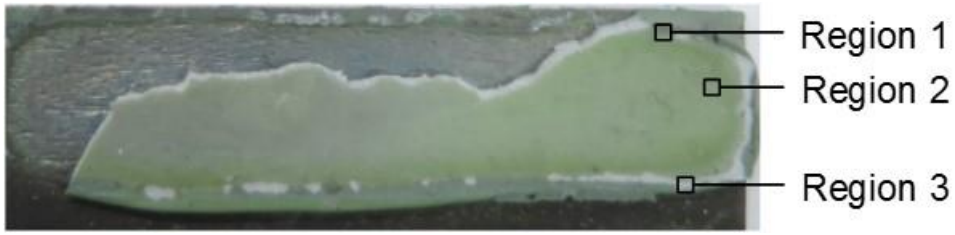

(a)

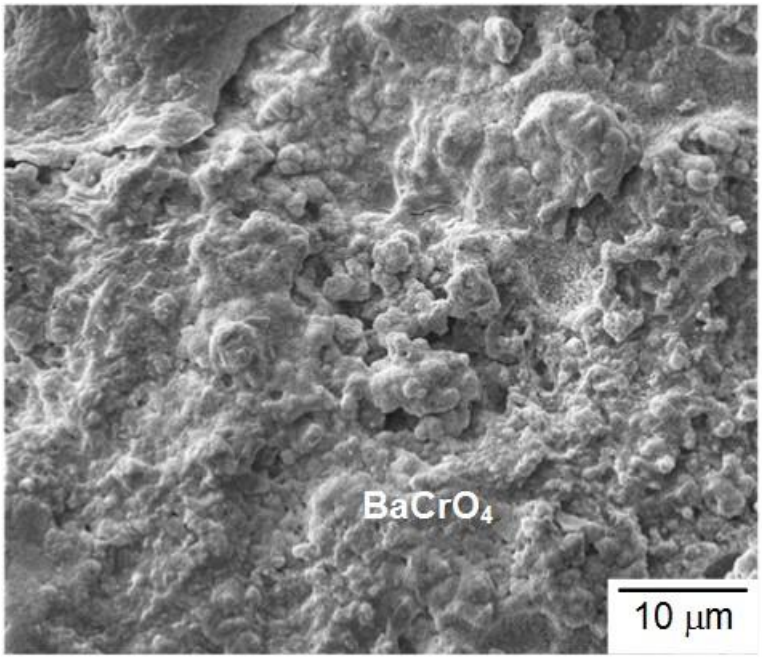

(b)

Fig. 22 Fracture surface of the non-aged shear specimen shown in the upper part of Fig. 15(c): (a) optical micrograph showing the observed regions of SEM; (b) SEM micrograph of Region 1 ($BaCrO_4$ chromate); (c) SEM micrograph of Region 2 (glass-ceramic sealant); (d) SEM micrograph of Region 3 (glass-ceramic sealant).

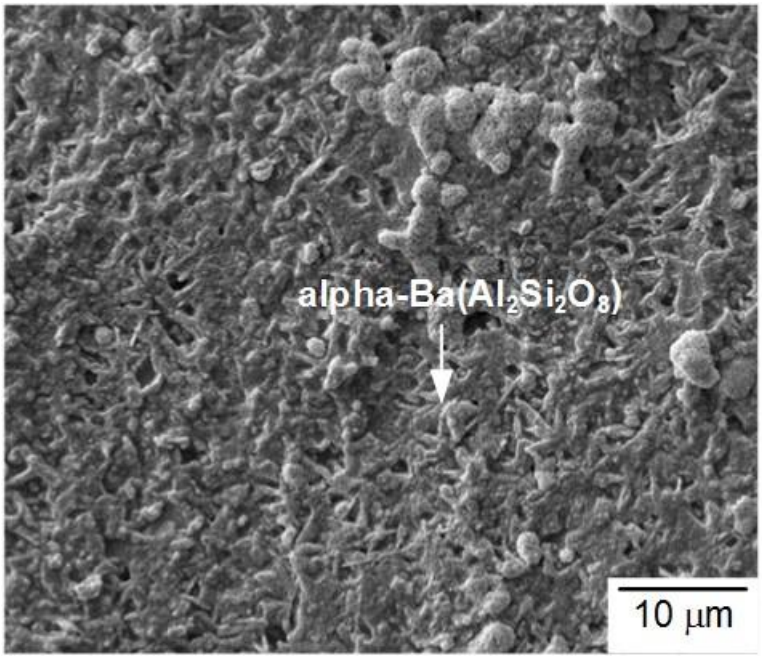

(c)

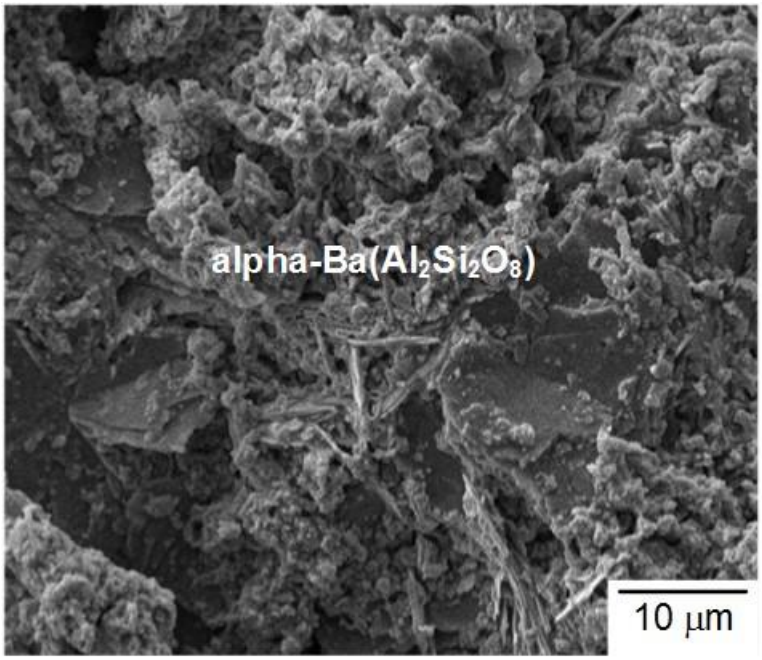

(d)

Fig. 22 (continued)

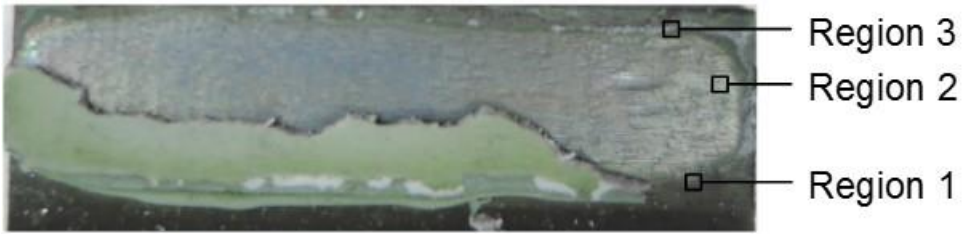

(a)

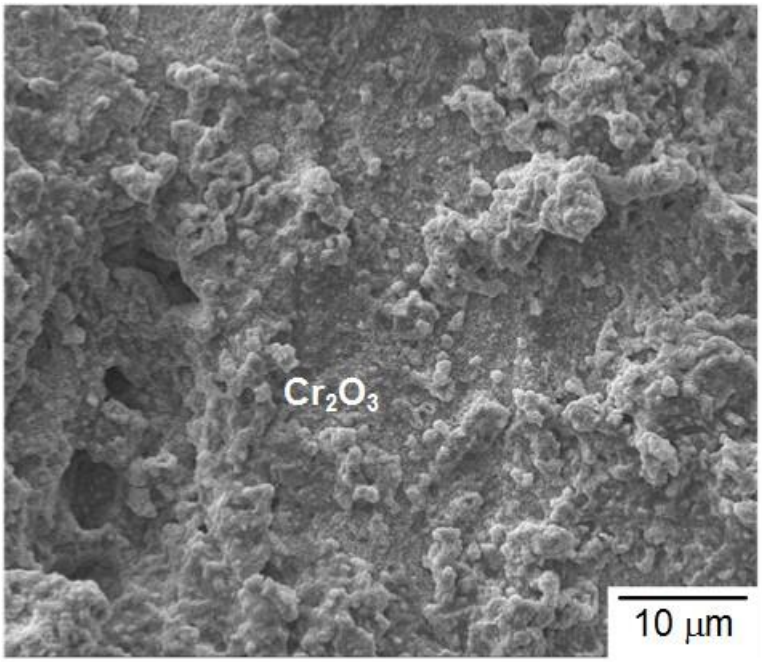

(b)

Fig. 23 Fracture surface of the non-aged shear specimen shown in the lower part of Fig. 15(c): (a) optical micrograph showing the observed regions of SEM; (b) SEM micrograph of Region 1 (Cr_2O_3 chromia); (c) SEM micrograph of Region 2 (Cr_2O_3 chromia); (d) SEM micrograph of Region 3 (glass-ceramic sealant).

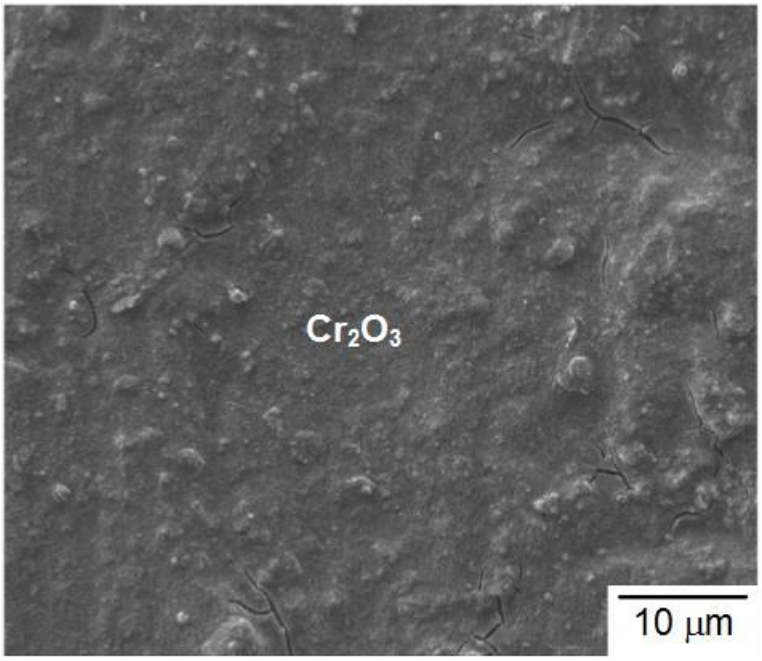

(c)

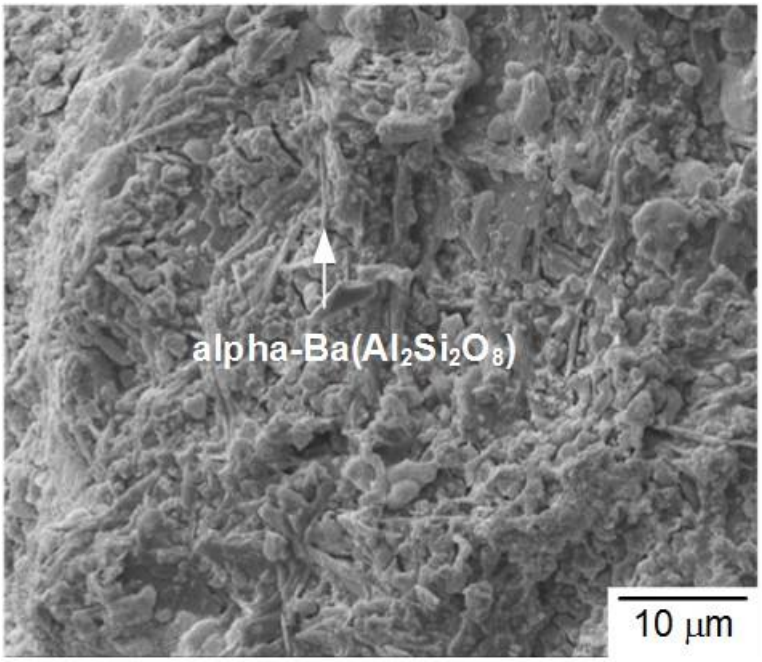

(d)

Fig. 23 (continued)

(a)

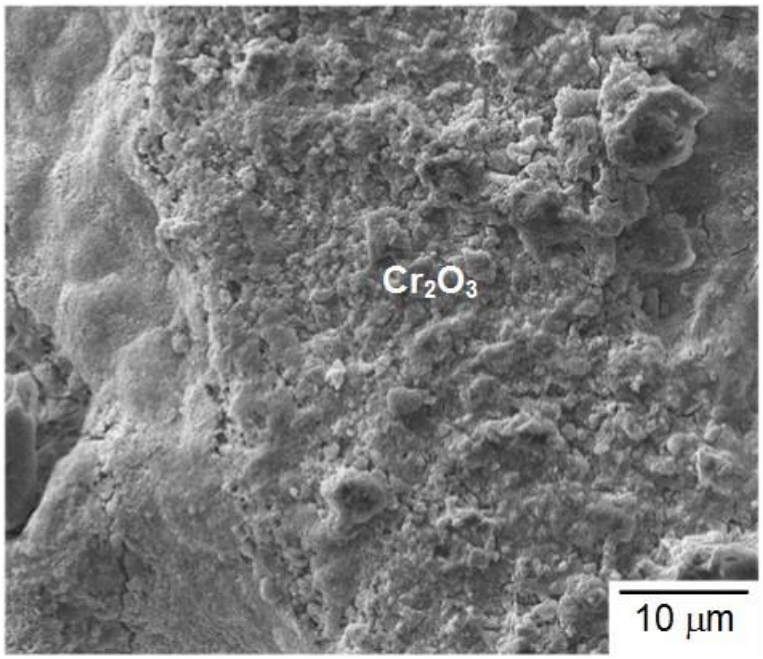

(b)

Fig. 24 Fracture surface of the non-aged shear specimen shown in the upper part of Fig. 15(d): (a) optical micrograph showing the observed regions of SEM; (b) SEM micrograph of Region 1 (Cr_2O_3 chromia); (c) SEM micrograph of Region 2 (glass-ceramic sealant).

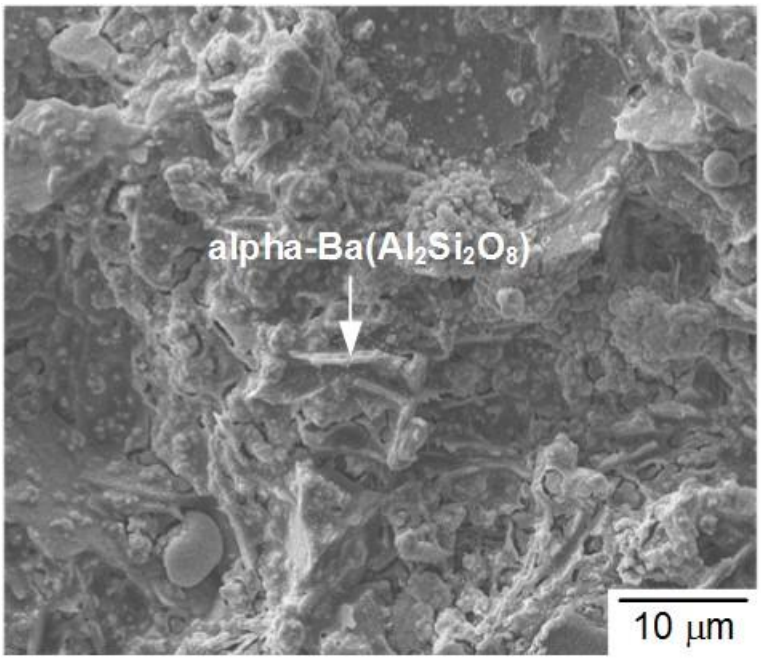

(c)

Fig. 24 (continued)

(a)

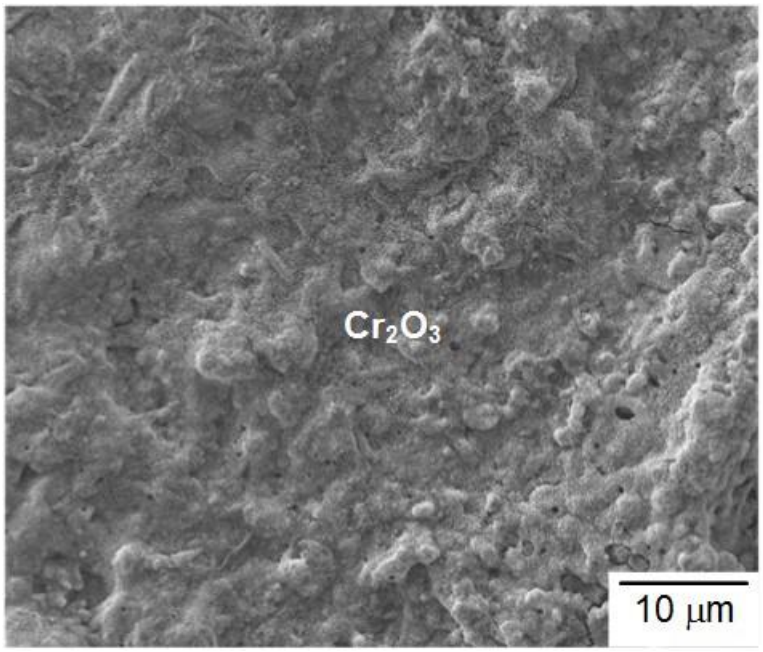

(b)

Fig. 25 Fracture surface of the non-aged shear specimen shown in the lower part of Fig. 15(d): (a) optical micrograph showing the observed regions of SEM; (b) SEM micrograph of Region 1 (Cr_2O_3 chromia); (c) SEM micrograph of Region 2 (glass-ceramic sealant).

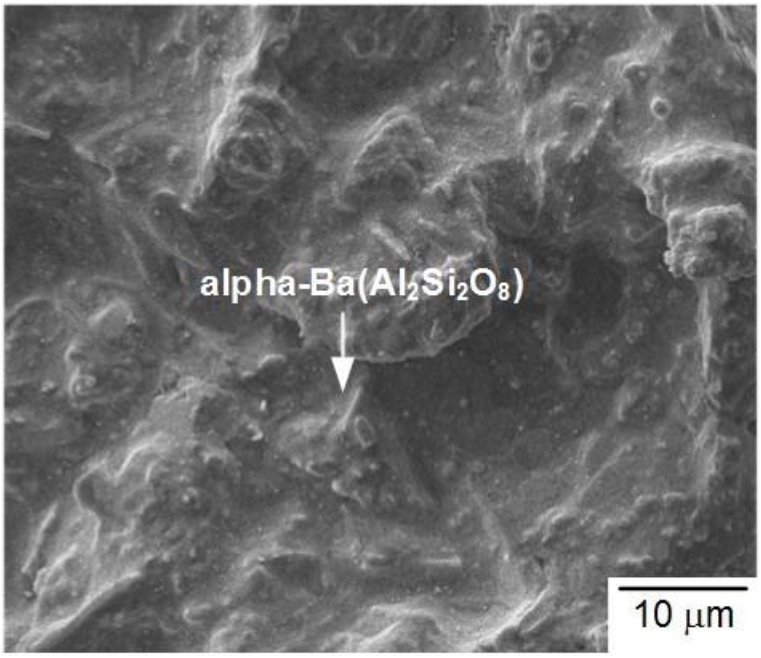

(c)

Fig. 25 (continued)

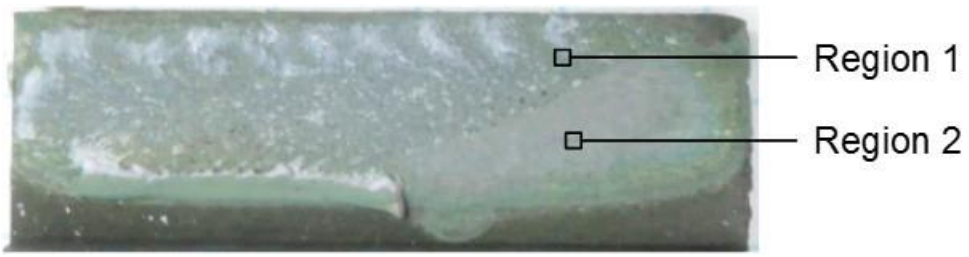

(a)

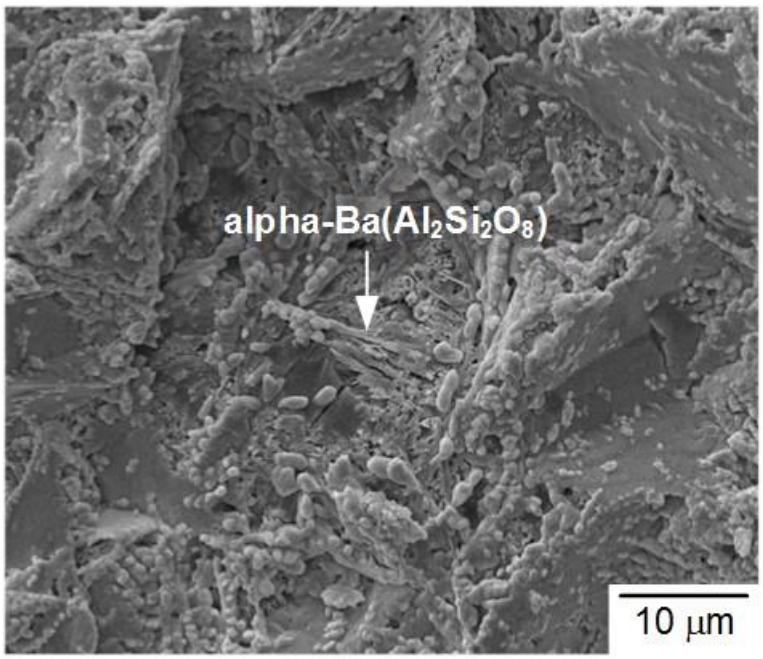

(b)

Fig. 26 Fracture surface of the non-aged shear specimen shown in the upper part of Fig. 15(e): (a) optical micrograph showing the observed regions of SEM; (b) SEM micrograph of Region 1 (glass-ceramic sealant); (c) SEM micrograph of Region 2 (glass-ceramic sealant).

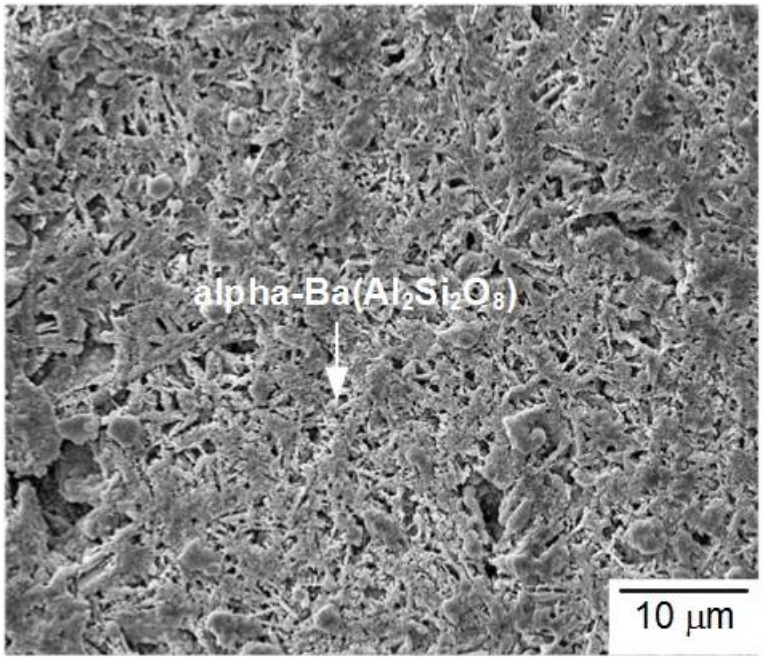

(c)

Fig. 26 (continued)

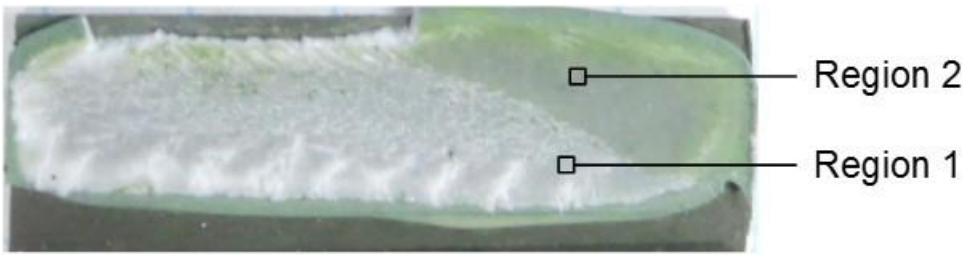

(a)

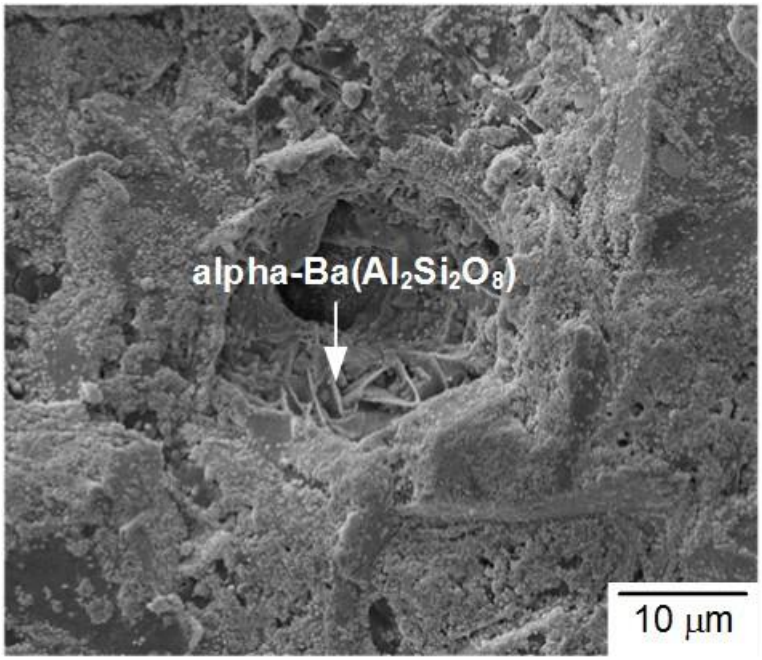

(b)

Fig. 27 Fracture surface of the non-aged shear specimen shown in the lower part of Fig. 15(e): (a) optical micrograph showing the observed regions of SEM; (b) SEM micrograph of Region 1 (glass-ceramic sealant); (c) SEM micrograph of Region 2 (Cr_2O_3 chromia).

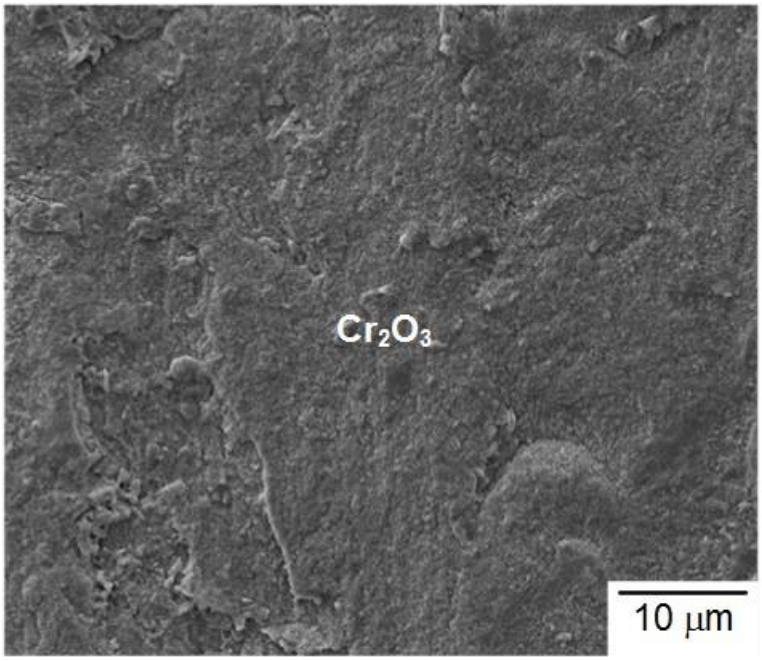

(c)

Fig. 27 (continued)

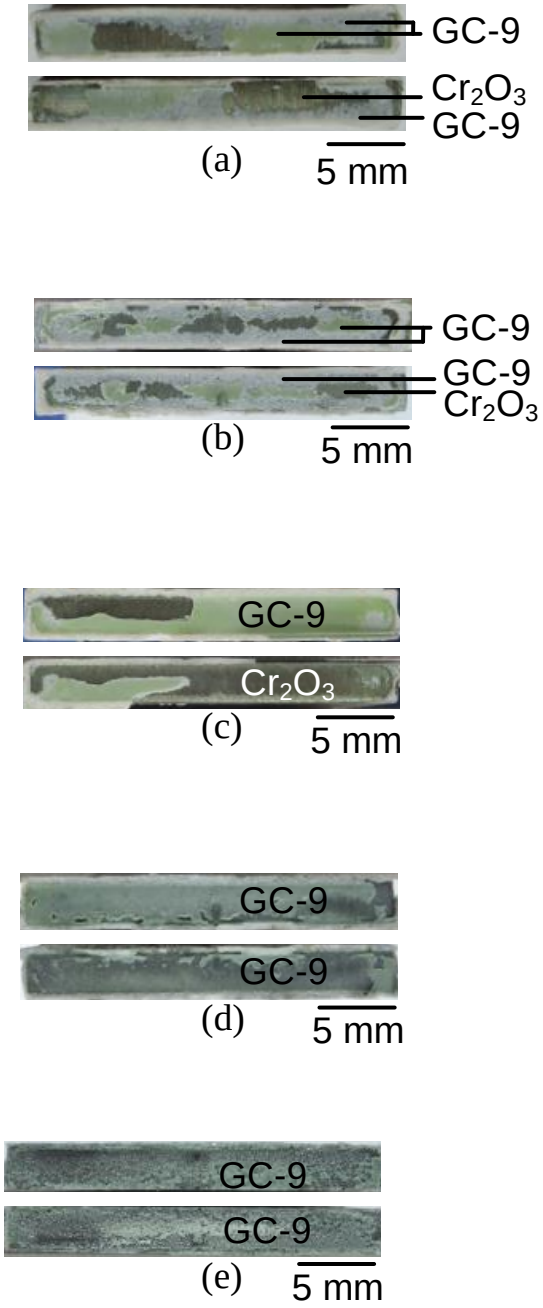

Fig. 28 Failure patterns in the non-aged tensile specimens tested at 800 ℃ with various creep rupture times: (a) 0-1 h; (b) 1-10 h; (c) 10-100 h; (d) 100-1000 h; (e) over 1000 h.

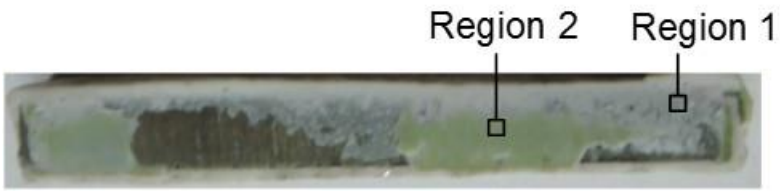

(a)

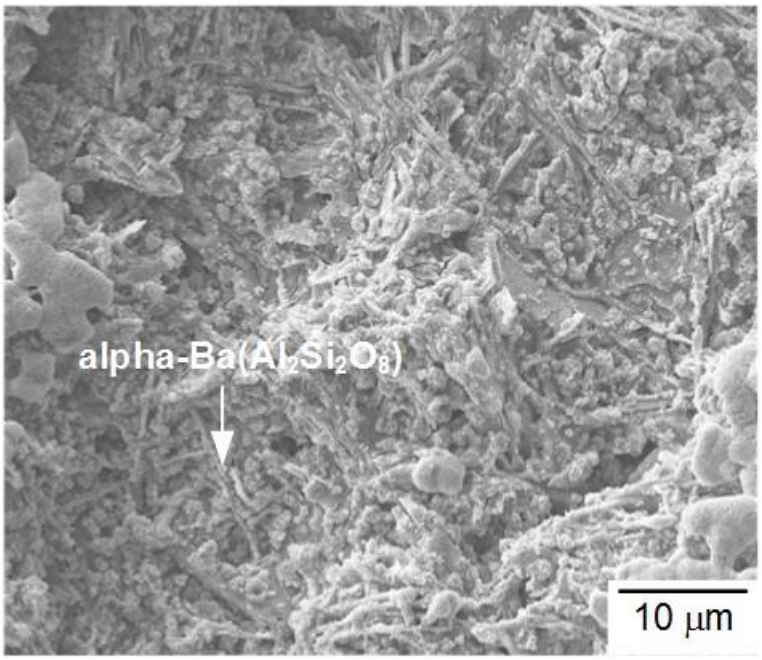

(b)

Fig. 29 Fracture surface of the non-aged tensile specimen shown in the upper part of Fig. 25(a): (a) optical micrograph showing the observed regions of SEM; (b) SEM micrograph of Region 1 (glass-ceramic sealant); (c) SEM micrograph of Region 2 (glass-ceramic sealant).

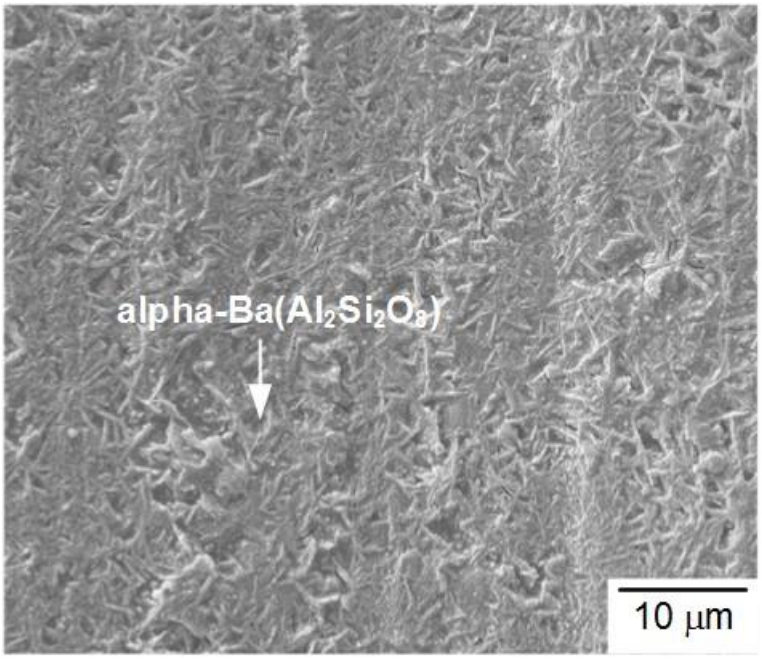

(c)

Fig. 29 (continued)

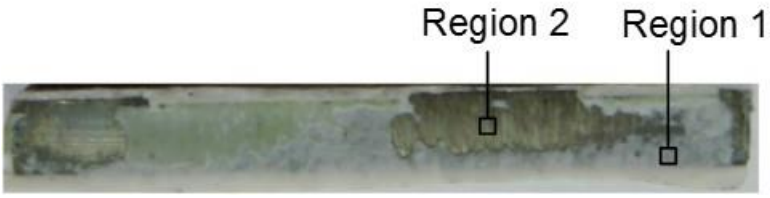

(a)

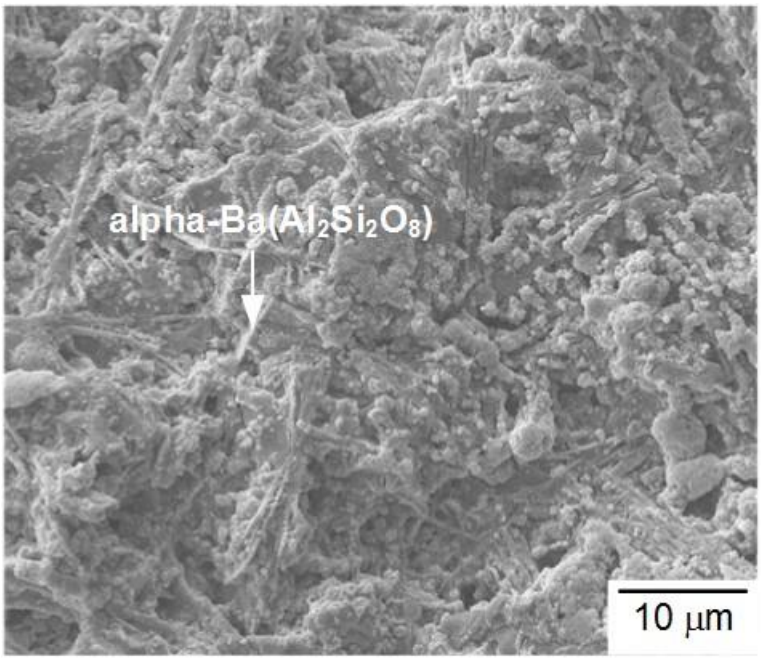

(b)

Fig. 30 Fracture surface of the non-aged tensile specimen shown in the lower part of Fig. 28(a): (a) optical micrograph showing the observed regions of SEM; (b) SEM micrograph of Region 1 (glass-ceramic sealant); (c) SEM micrograph of Region 2 (Cr_2O_3 chromia).

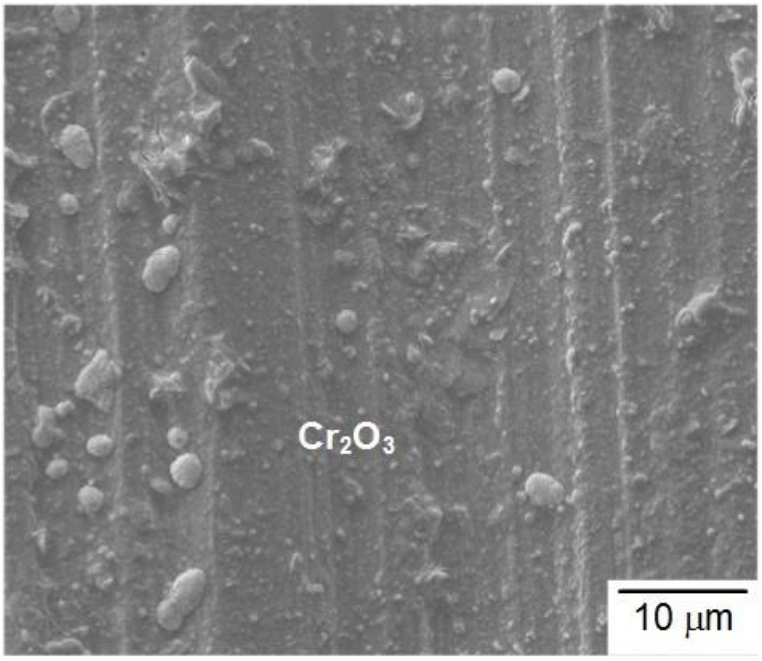

(c)

Fig. 30 (continued)

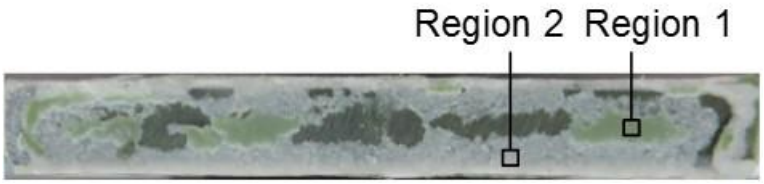

(a)

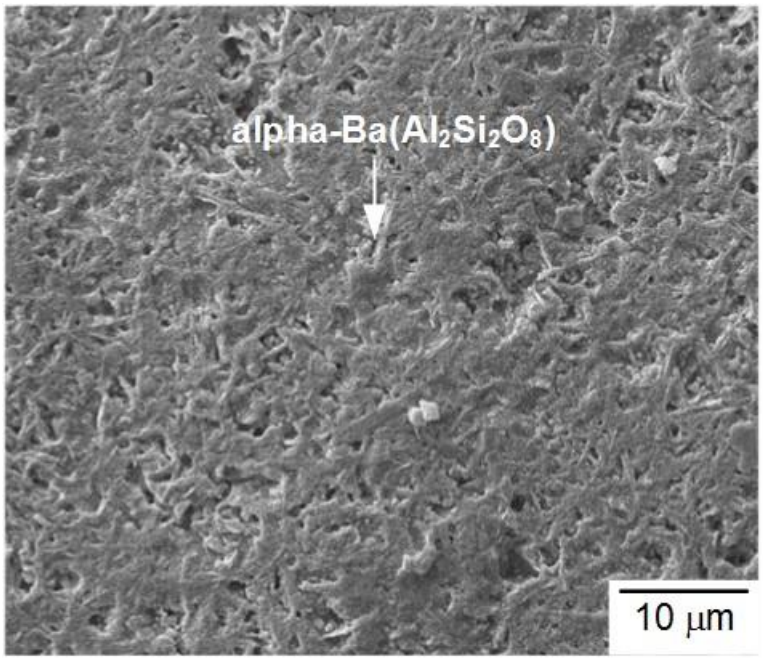

(b)

Fig. 31 Fracture surface of the non-aged tensile specimen shown in the upper part of Fig. 28(b): (a) optical micrograph showing the observed regions of SEM; (b) SEM micrograph of Region 1 (glass-ceramic sealant); (c) SEM micrograph of Region 2 (glass-ceramic sealant).

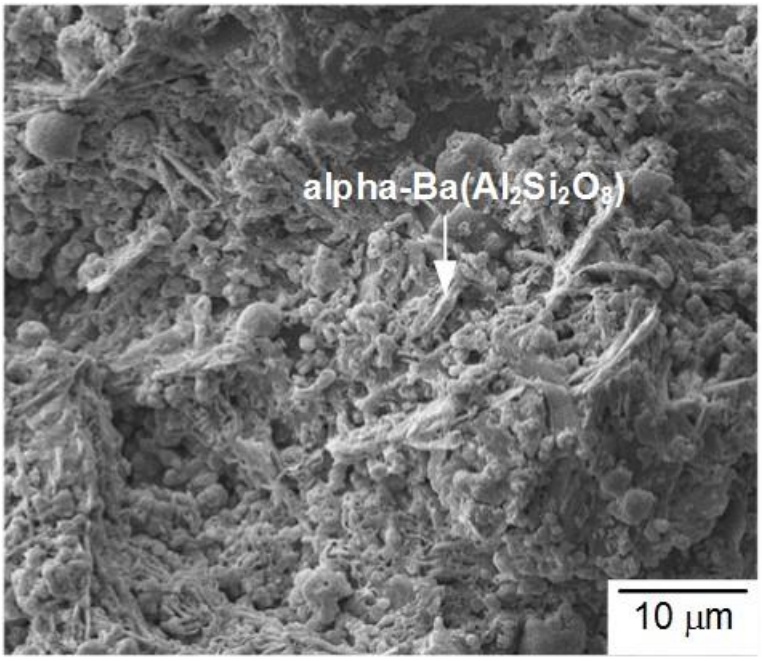

(c)

Fig. 31 (continued)

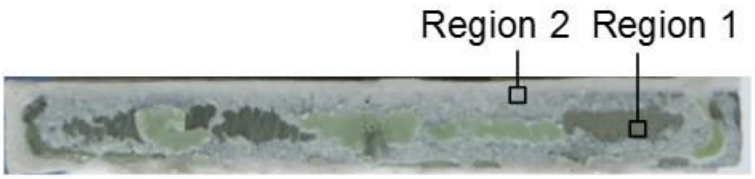

(a)

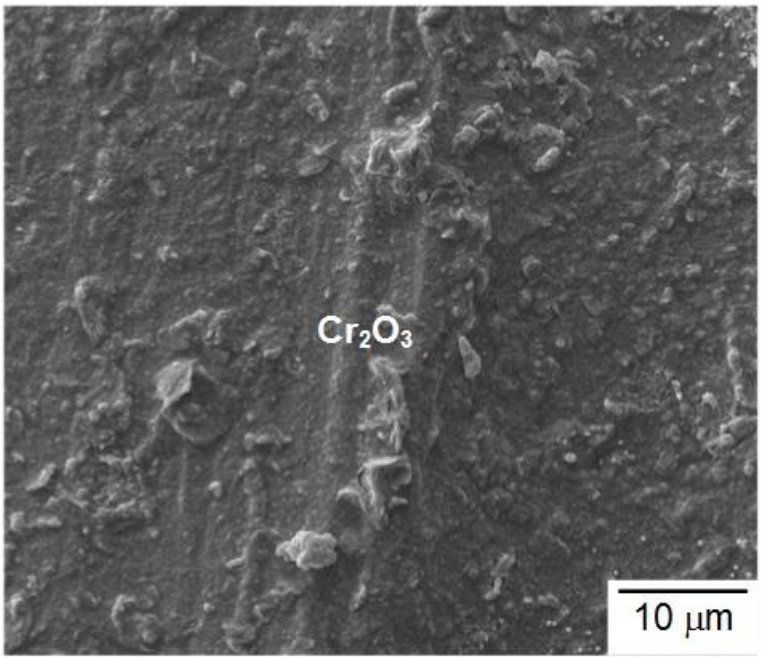

(b)

Fig. 32 Fracture surface of the non-aged tensile specimen shown in the lower part of Fig. 28(b): (a) optical micrograph showing the observed regions of SEM; (b) SEM micrograph of Region 1 (Cr_2O_3 chromia); (c) SEM micrograph of Region 2 (glass-ceramic sealant).

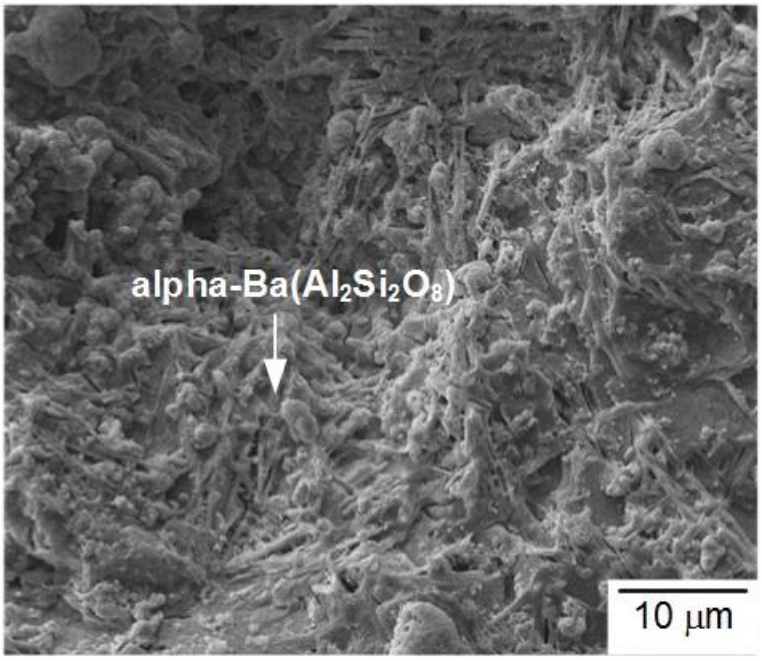

(c)

Fig. 32 (continued)

(a)

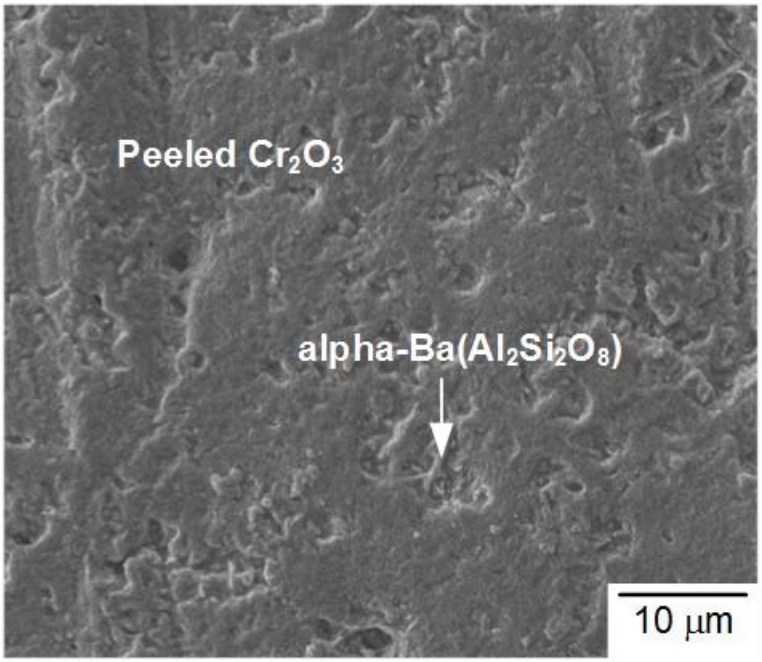

(b)

Fig. 33 Fracture surface of the non-aged tensile specimen shown in the upper part of Fig. 28(c): (a) optical micrograph showing the observed region of SEM; (b) SEM micrograph of Region 1 (glass-ceramic sealant).

(a)

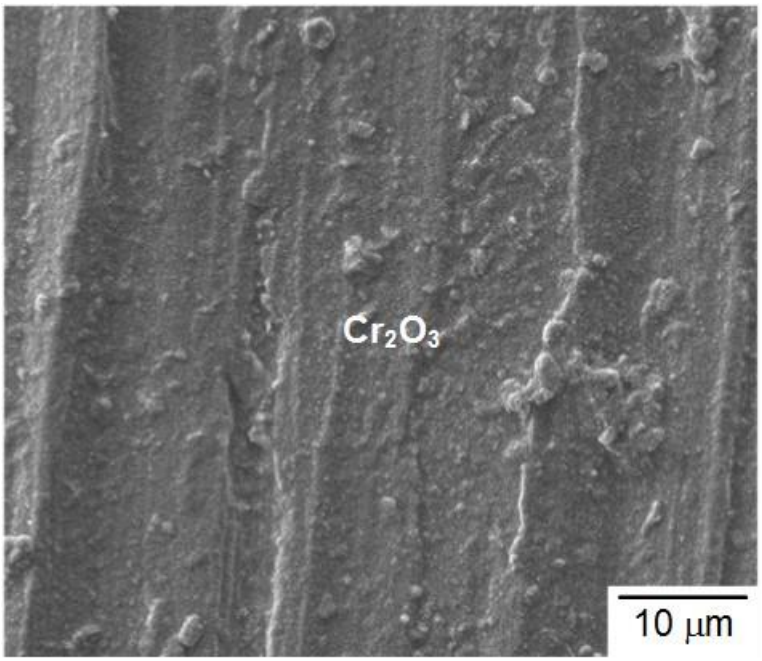

(b)

Fig. 34 Fracture surface of the non-aged tensile specimen shown in the lower part of Fig. 28(c): (a) optical micrograph showing the observed region of SEM; (b) SEM micrograph of Region 1 (Cr_2O_3 chromia).

(a)

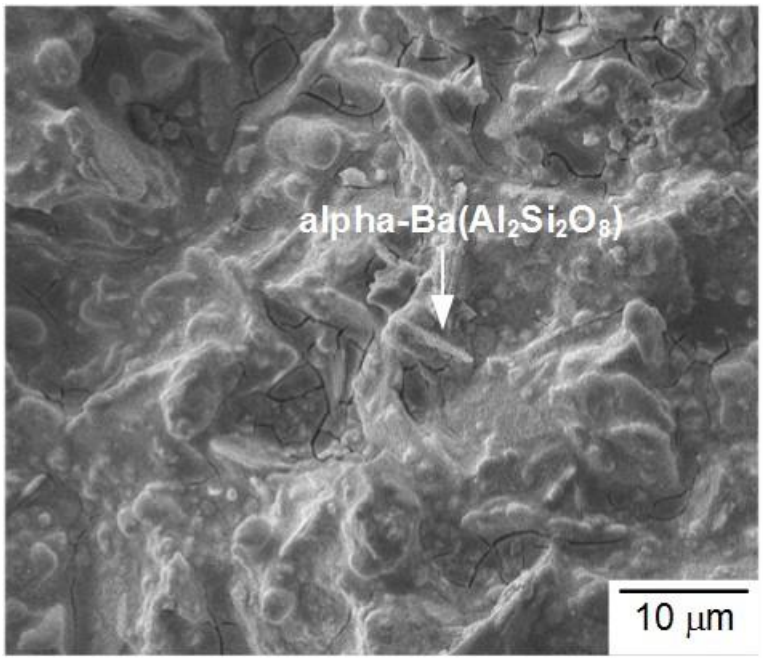

(b)

Fig. 35 Fracture surface of the non-aged tensile specimen shown in the upper part of Fig. 28(d): (a) optical micrograph showing the observed region of SEM; (b) SEM micrograph of Region 1 (glass-ceramic sealant).

(a)

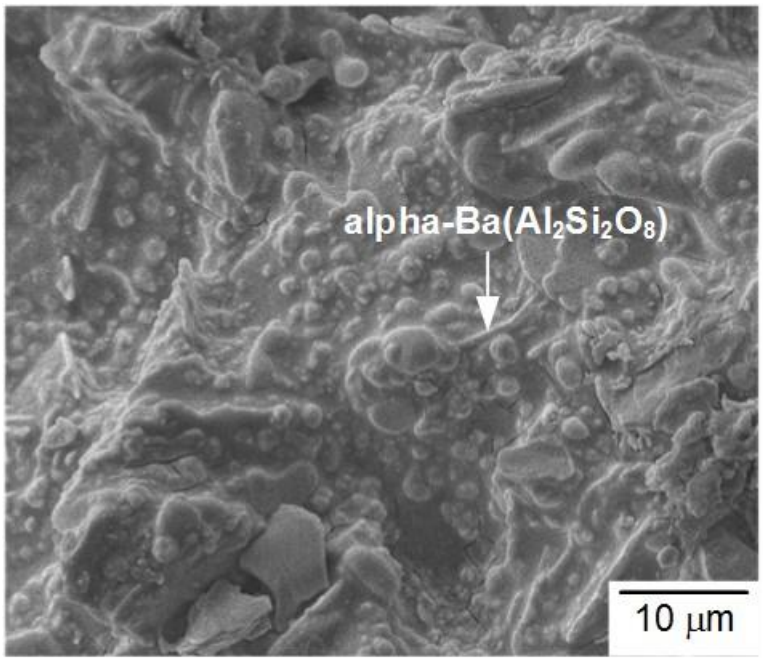

(b)

Fig. 36 Fracture surface of the non-aged tensile specimen shown in the lower part of Fig. 28(d): (a) optical micrograph showing the observed region of SEM; (b) SEM micrograph of Region 1 (glass-ceramic sealant).

(a)

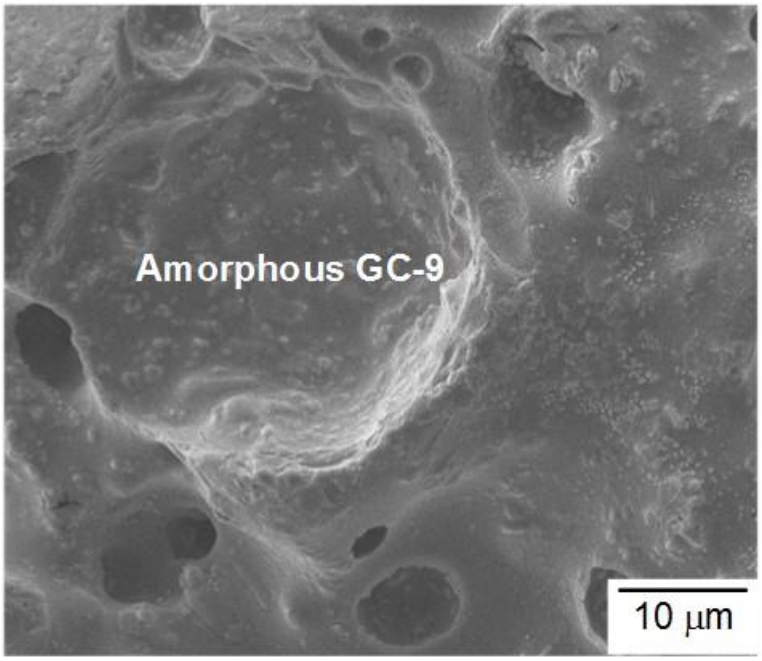

(b)

Fig. 37 Fracture surface of the non-aged tensile specimen shown in the upper part of Fig. 28(e): (a) optical micrograph showing the observed region of SEM; (b) SEM micrograph of Region 1 (glass-ceramic sealant).

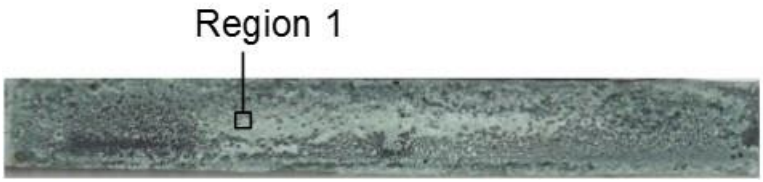

(a)

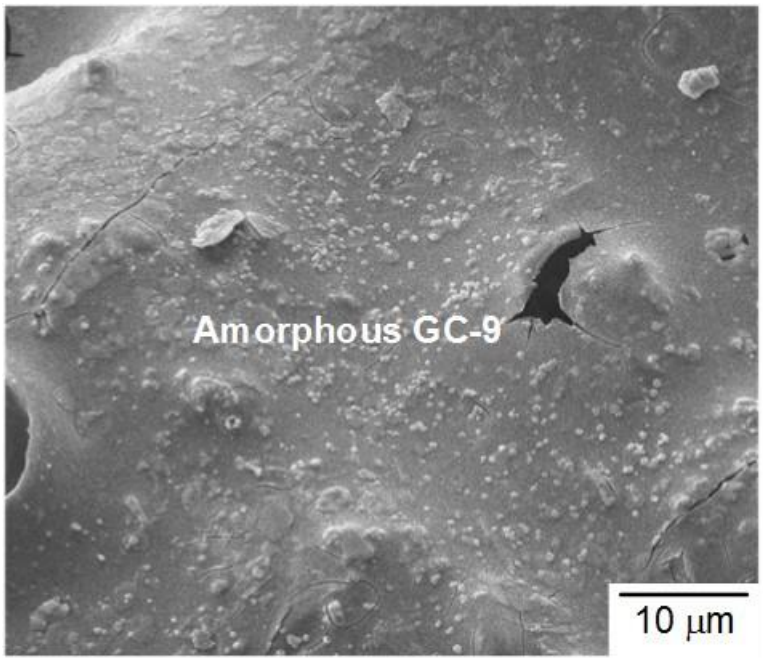

(b)

Fig. 38 Fracture surface of the non-aged tensile specimen shown in the lower part of Fig. 28(e): (a) optical micrograph showing the observed region of SEM; (b) SEM micrograph of Region 1 (glass-ceramic sealant).

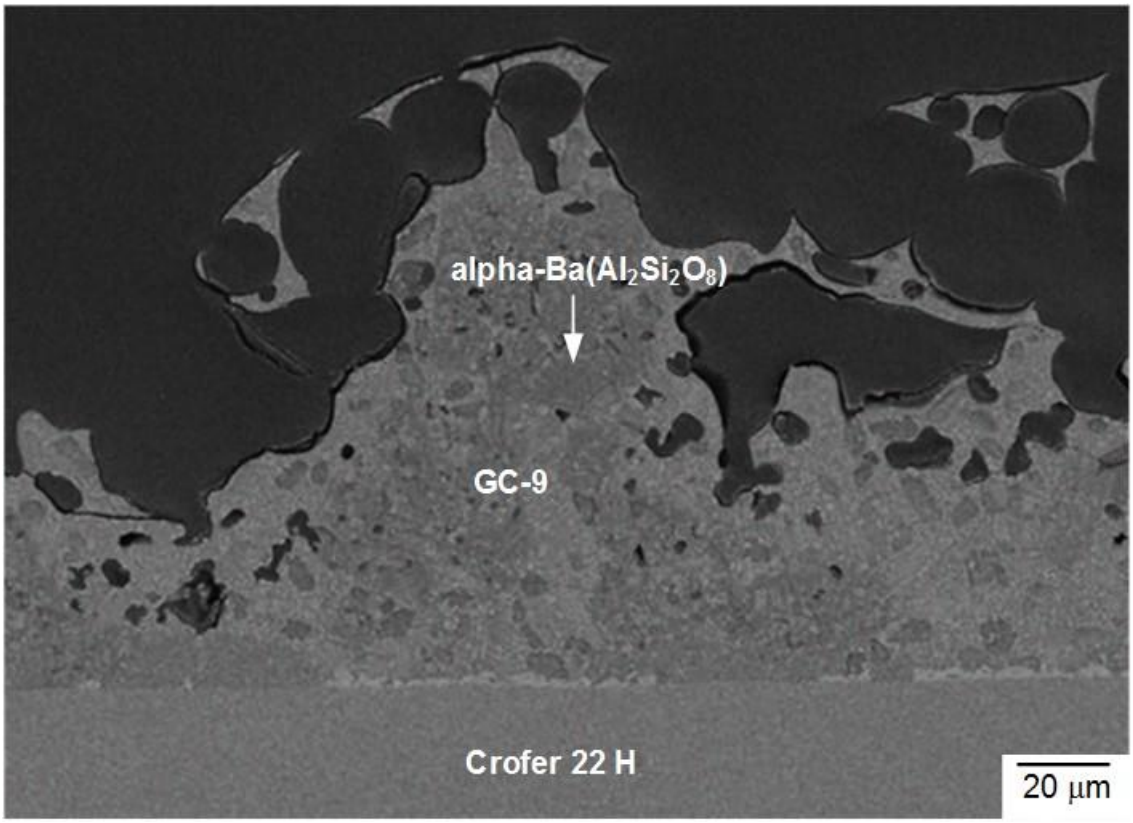

Fig. 39 SEM micrograph (BSE mode) of a cross section of an interface between the GC-9 and Crofer 22 H taken from Fig. 28(e)

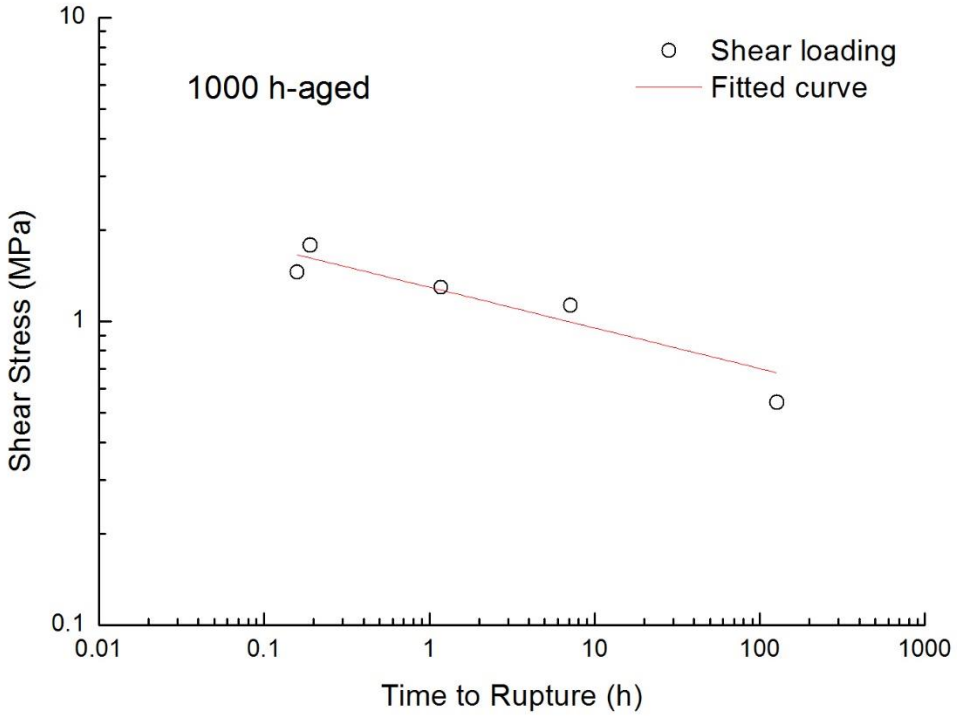

(a)

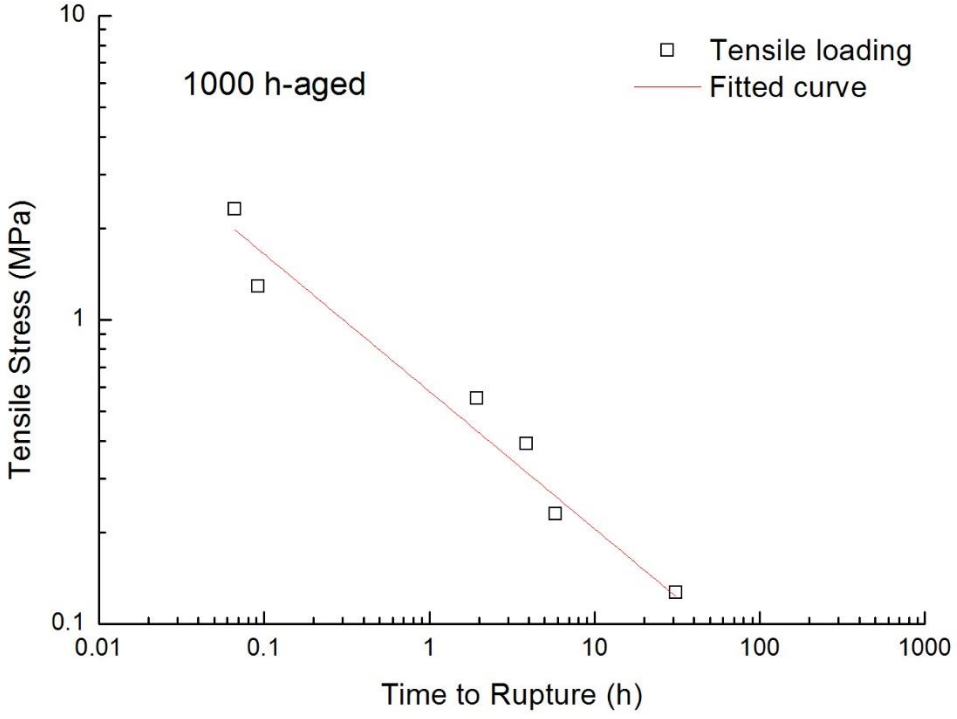

(b)

Fig. 40 Applied stress versus rupture time for 1000 h-aged joint specimens subjected to constant (a) shear and (b) tensile loading.

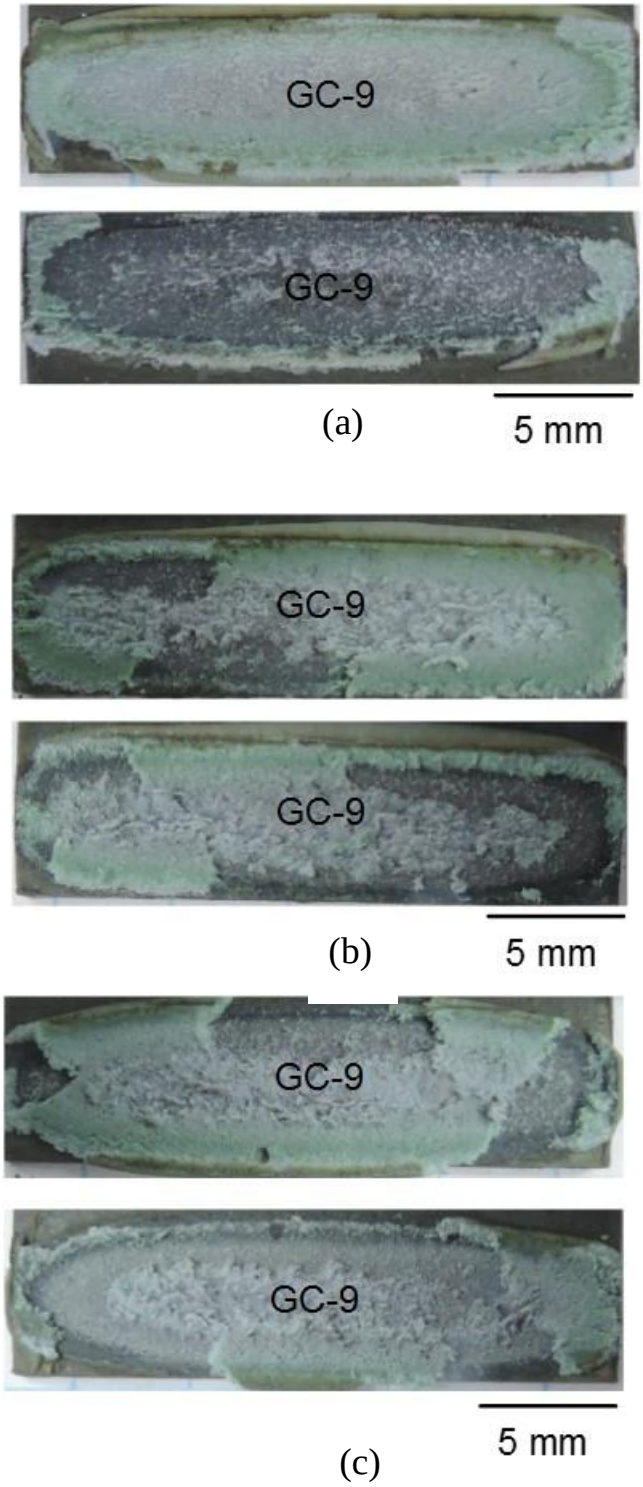

Fig. 41 Failure patterns in the 1000 h-aged shear specimens tested at 800 ℃ with various creep rupture times: (a) 0-1 h; (b) 1-10 h; (c) 10-100 h.

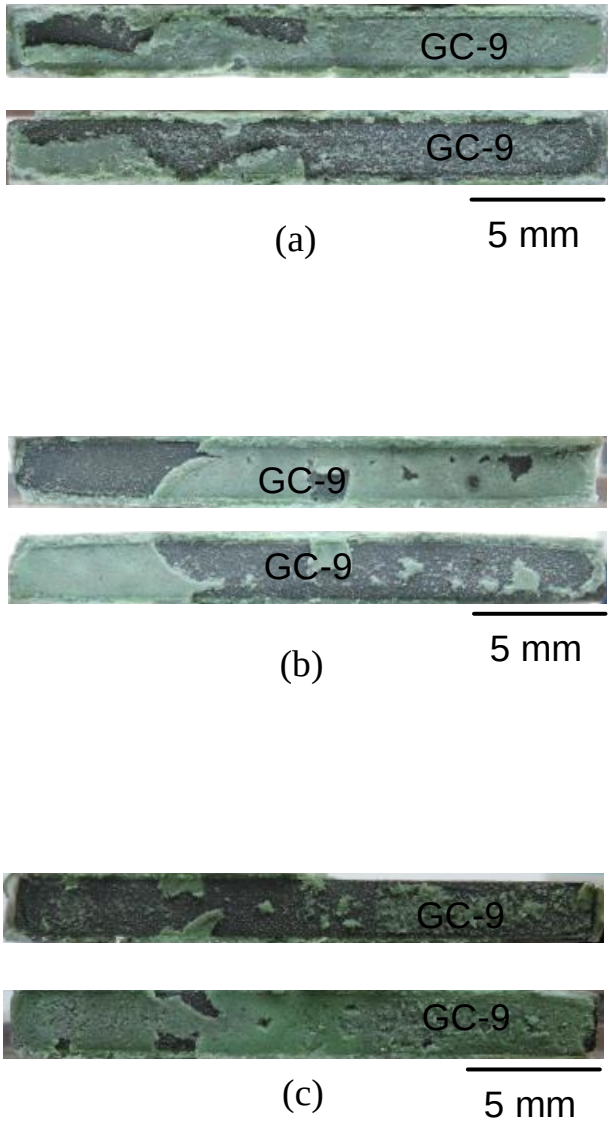

Fig. 42 Failure patterns in the 1000 h-aged tensile specimens tested at 800 ℃ with various creep rupture times: (a) 0-1 h; (b) 1-10 h; (c) 10-100 h.

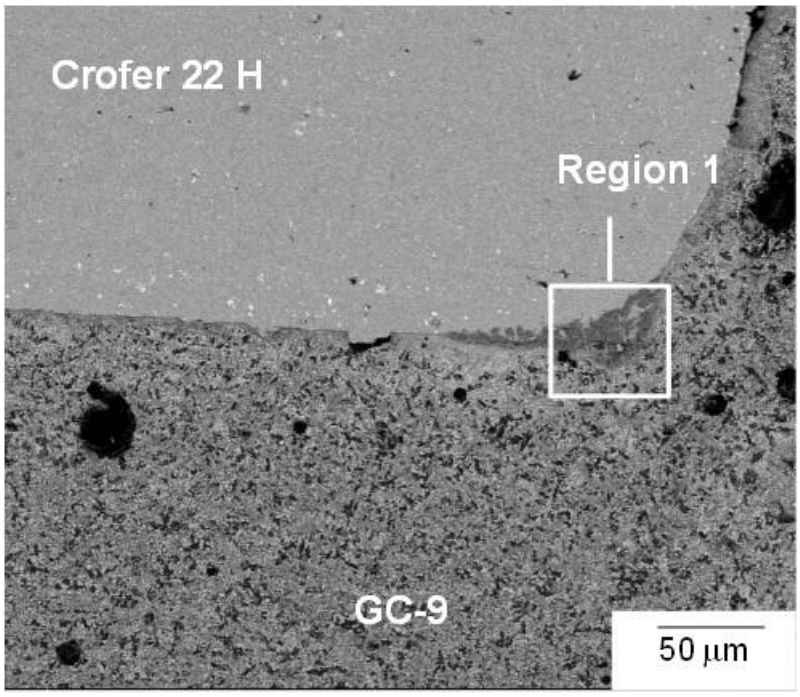

(a)

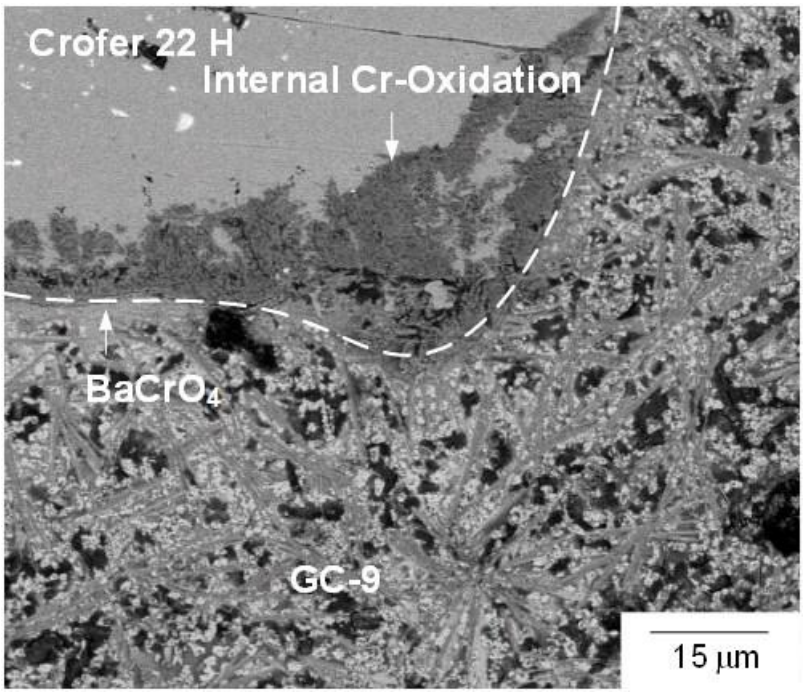

(b)

Fig. 43 SEM micrographs (BSE mode) of a cross section of an interface between the GC-9 and Crofer 22 H in a 100 h-aged specimen: (a) low magnification view; (b) high magnification of the region 1 in (a). [45]

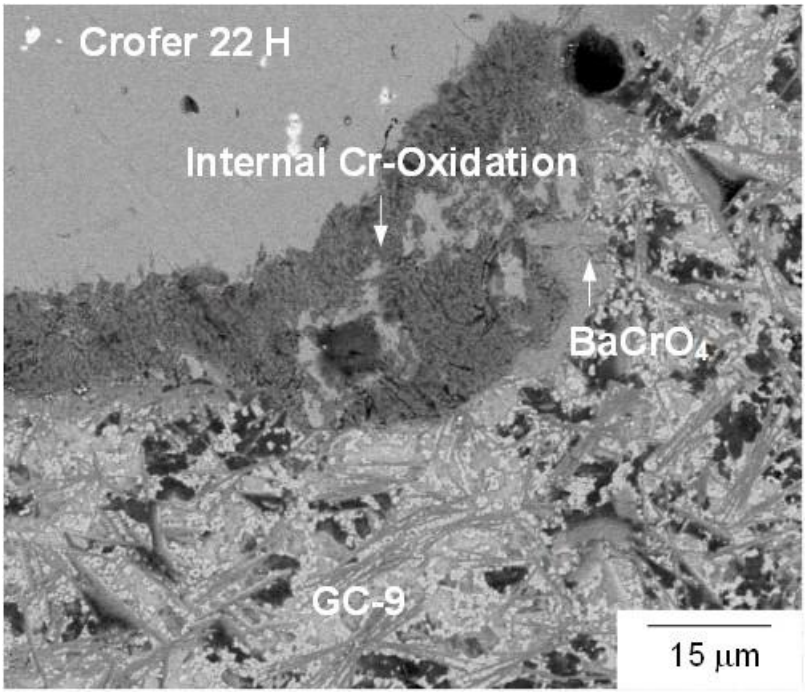

Fig. 44 SEM micrographs (BSE mode) of a cross section of an interface between the GC-9 and Crofer 22 H in a 1000 h-aged specimen at edge of the joint. [45]

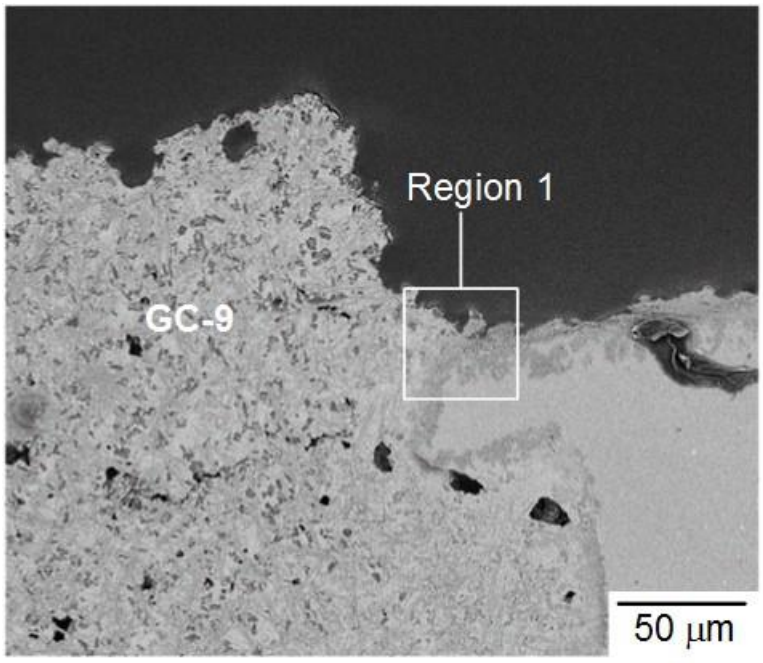

(a)

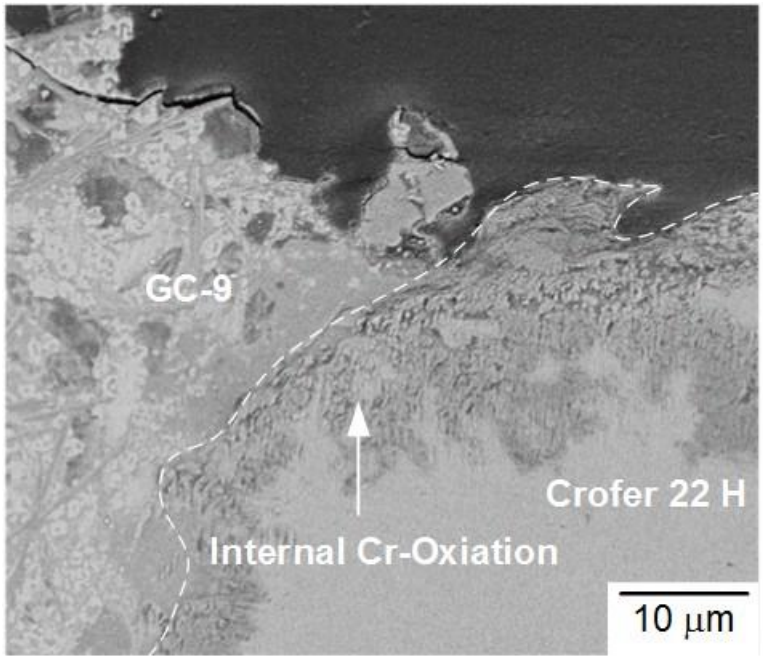

(b)

Fig. 45 SEM micrographs (BSE mode) of a cross section of an interface between the GC-9 and Crofer 22 H taken from Fig. 28(d): (a) low magnification view; (b) high magnification of the Region 1 in (a).

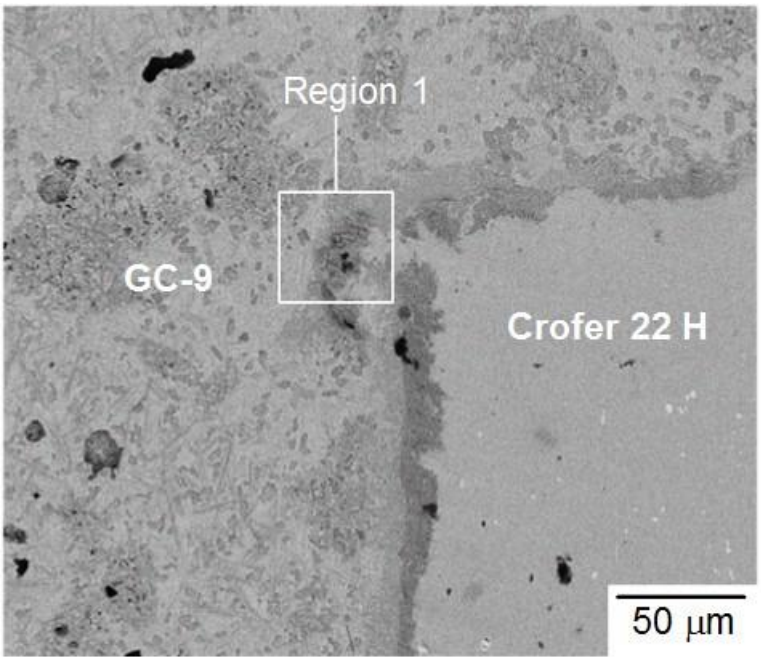

(a)

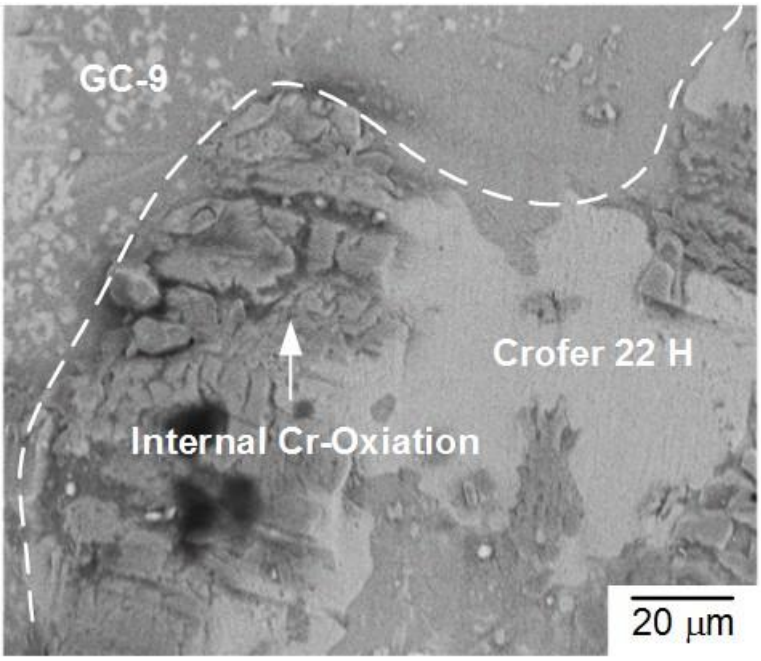

(b)

Fig. 46 SEM micrographs (BSE mode) of a cross section of an interface between the GC-9 and Crofer 22 H taken from Fig. 28(e): (a) low magnification view; (b) high magnification of the Region 1 in (a).

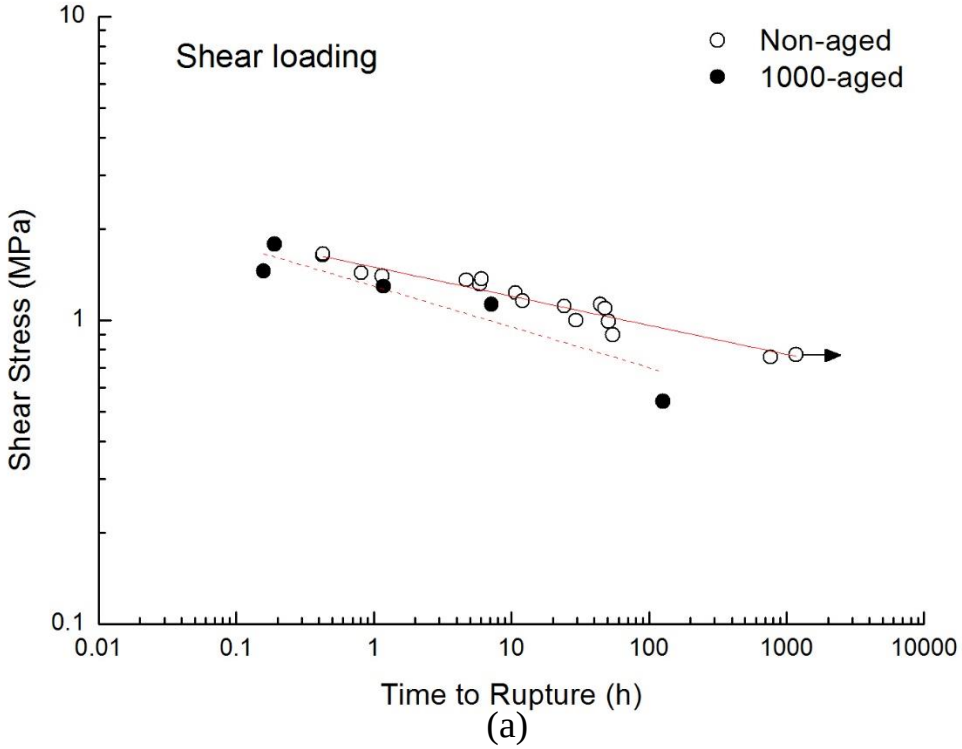

(a)

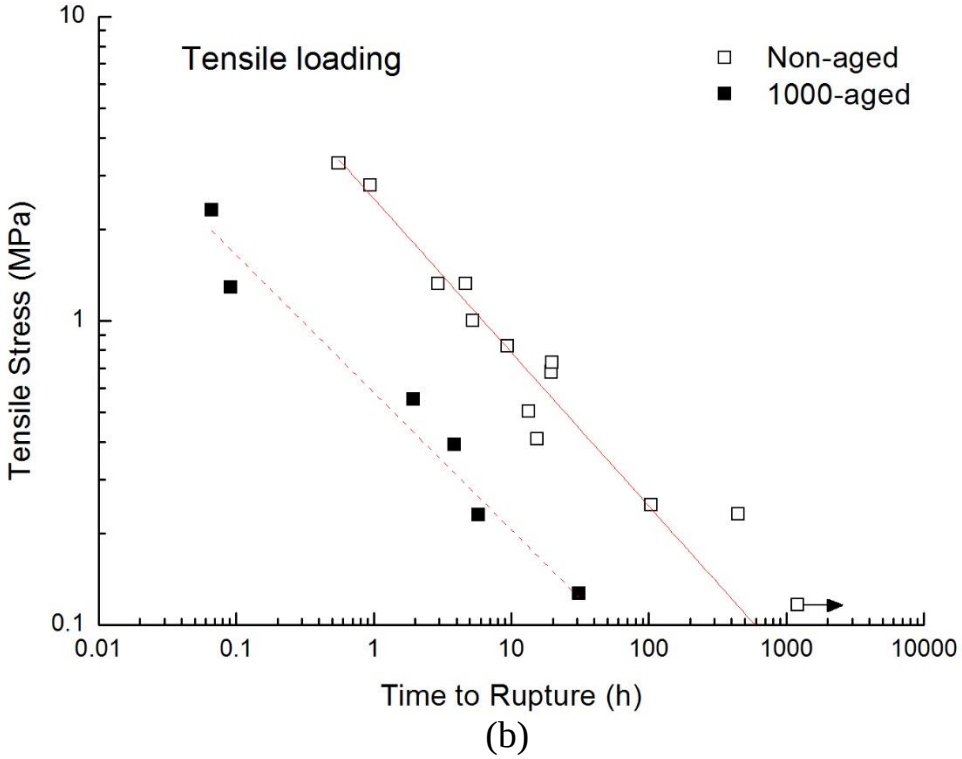

(b)

Fig. 47 Applied stress versus rupture time for non-aged and 1000 h-aged joint specimens under constant (a) shear and (b) tensile loading. (Arrow indicates the specimen was not ruptured when the test was terminated.)

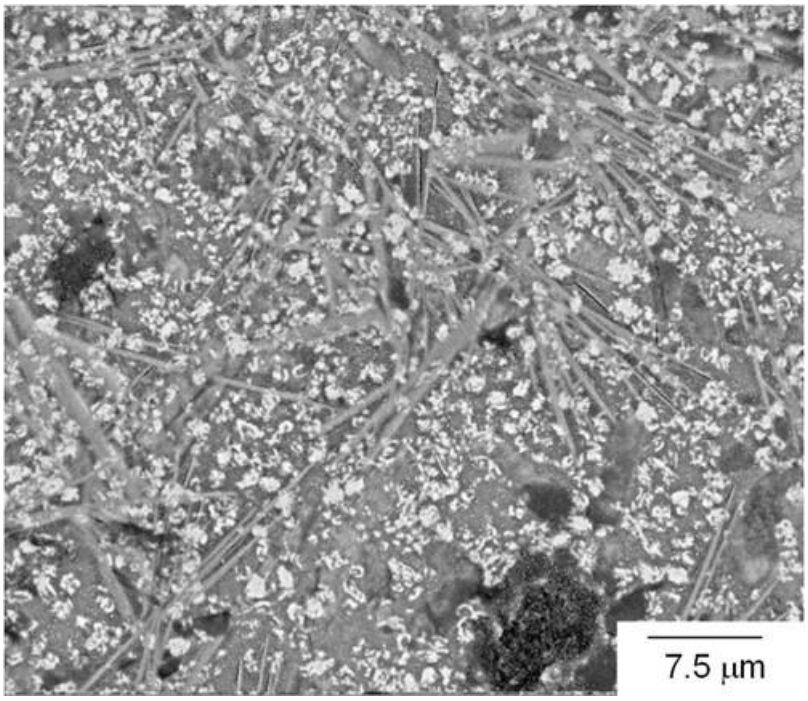

(a)

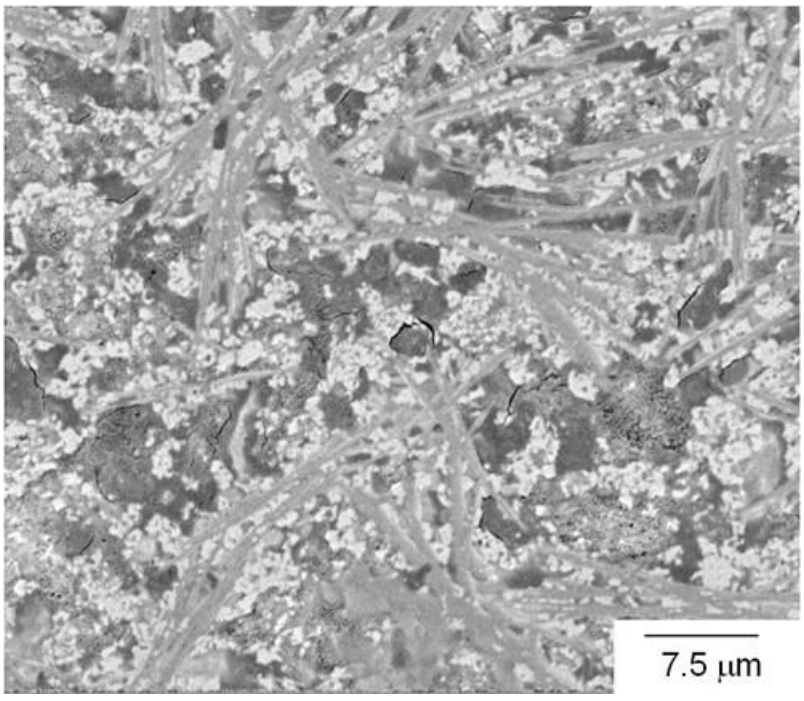

(b)

Fig. 48 SEM micrographs (in BSE mode) of variously aged GC-9 glass-ceramics: (a) non-aged; (b) 100 h-aged; (c) 1000 h-aged. [45]

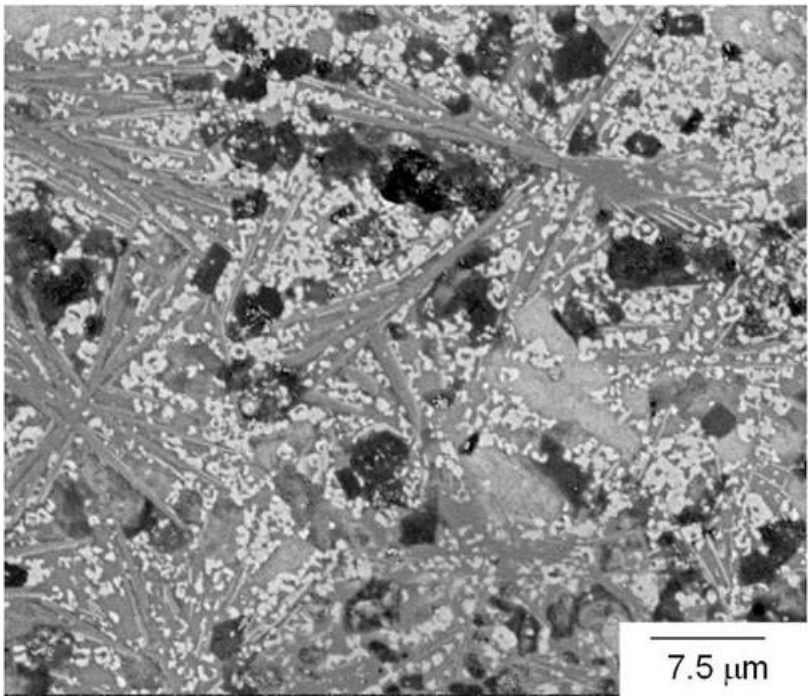

(c)

Fig. 48 (continued)

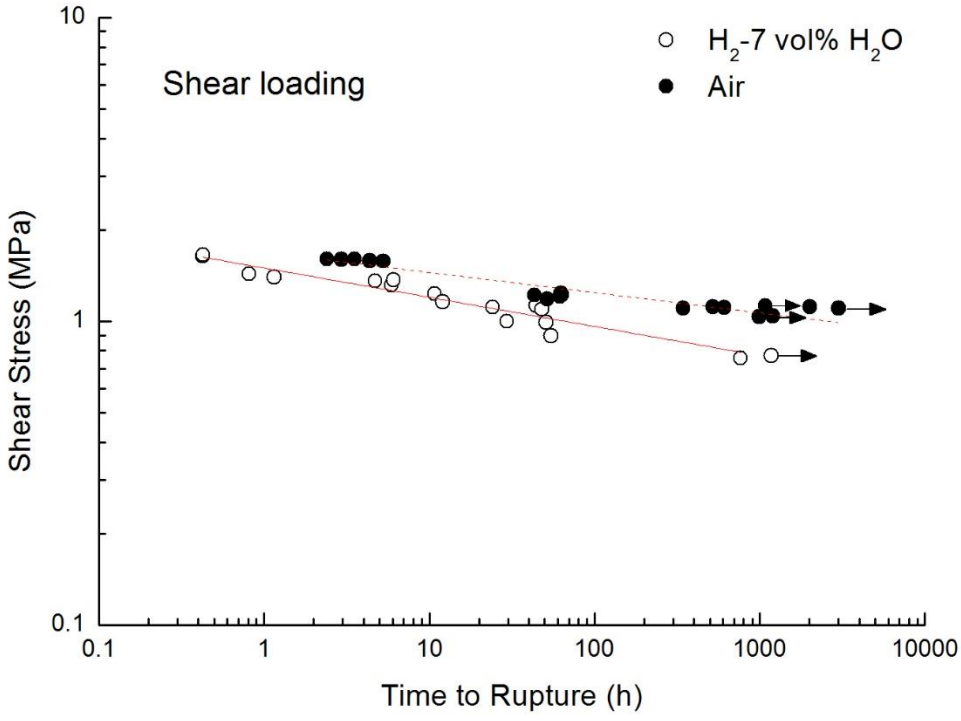

(a)

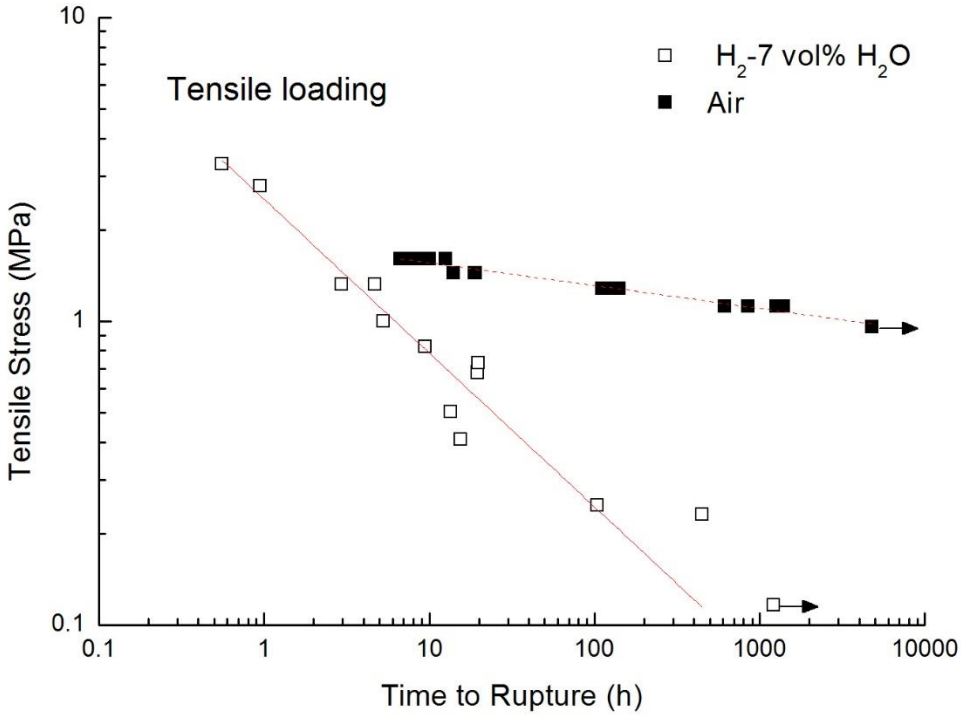

(b)

Fig. 49 Applied stress versus rupture time for the non-aged joint specimens in H_2-7 vol% H_2O and air under constant (a) shear and (b) tensile loading. (Arrow indicates the specimen was not ruptured when the test was terminated. The data of air are taken from Ref. [60].)

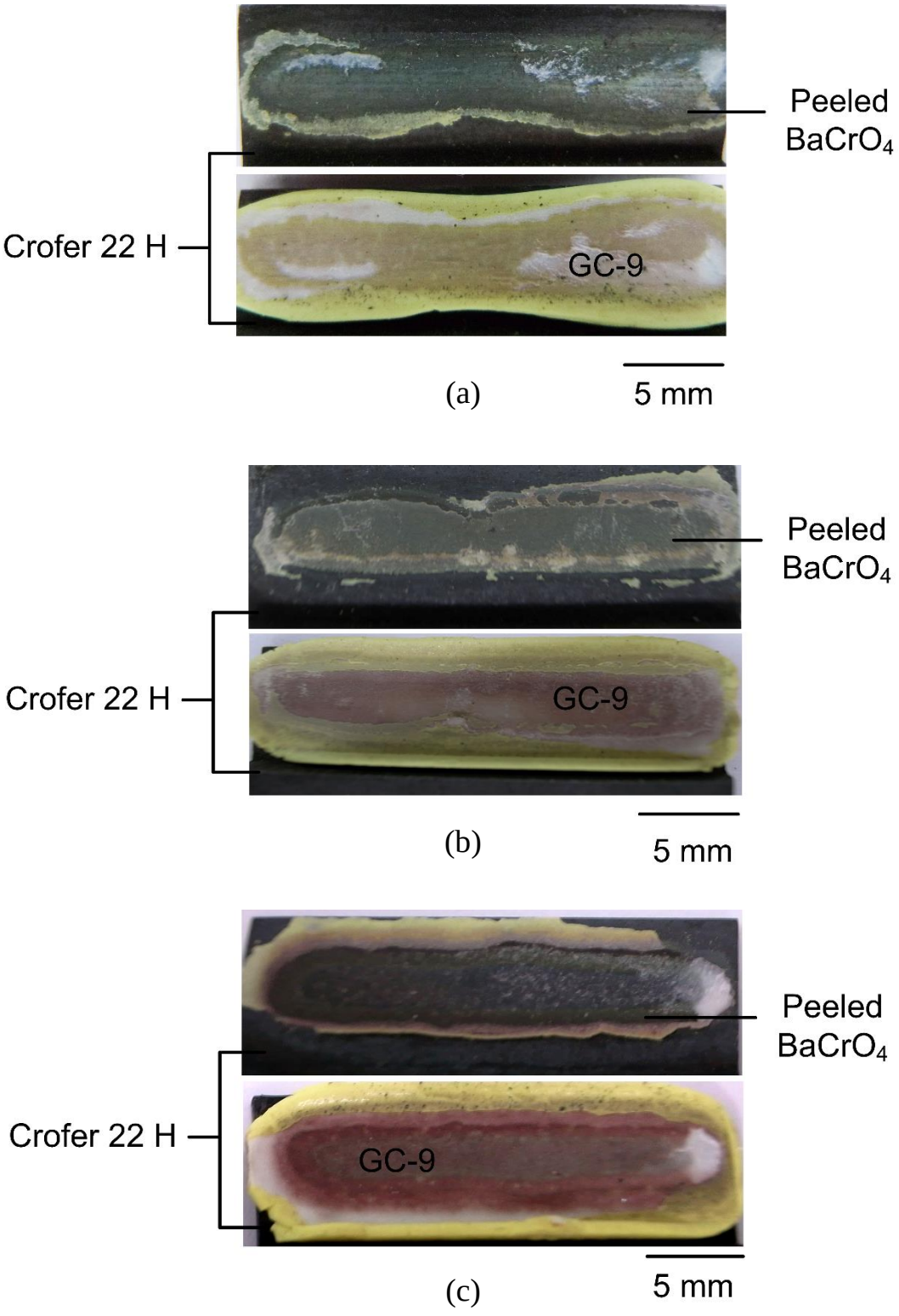

Fig. 50 Failure patterns in the non-aged shear specimens tested in air at 800 ℃ with various creep rupture times: (a) 0-100 h; (b) 100-1000 h; (c) over 1000 h. [60]

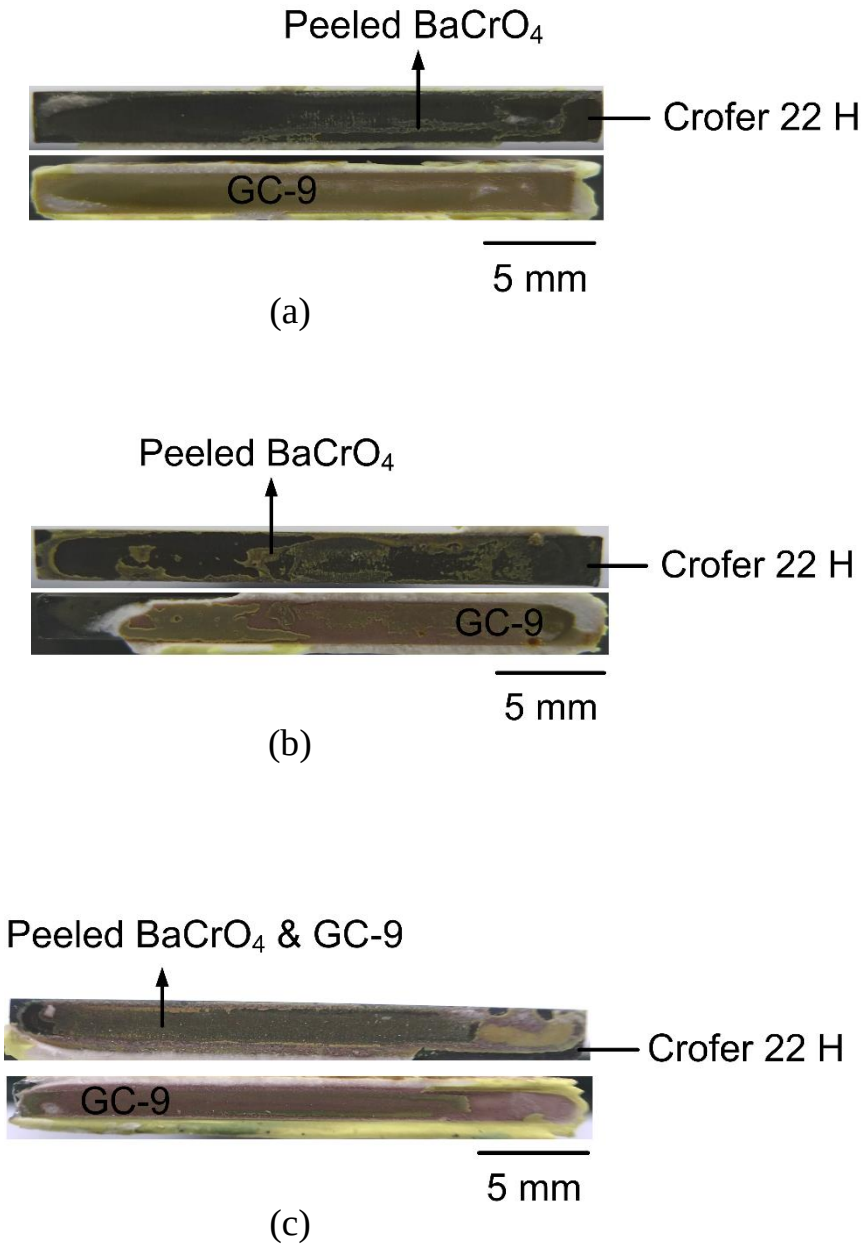

Fig. 51 Failure patterns in the non-aged tensile specimens tested in air at 800 ℃ with various creep rupture times: (a) 0-100 h; (b) 100-1000 h; (c) over 1000 h. [60]